

DEVELOPMENT OF A DESIGN METHOD FOR SUBSONIC INTAKES WITH  
IMPROVED AERODYNAMIC PERFORMANCE AND REDUCED RADAR  
SIGNATURE

A THESIS SUBMITTED TO  
THE GRADUATE SCHOOL OF NATURAL AND APPLIED SCIENCES  
OF  
MIDDLE EAST TECHNICAL UNIVERSITY

BY

TEZCAN ÜNLÜ

IN PARTIAL FULFILLMENT OF THE REQUIREMENTS  
FOR  
THE DEGREE OF MASTER OF SCIENCE  
IN  
AEROSPACE ENGINEERING

SEPTEMBER 2021



Approval of the thesis:

**DEVELOPMENT OF A DESIGN METHOD FOR SUBSONIC INTAKES  
WITH IMPROVED AERODYNAMIC PERFORMANCE AND REDUCED  
RADAR SIGNATURE**

submitted by **TEZCAN ÜNLÜ** in partial fulfillment of the requirements for the degree of **Master of Science in Aerospace Engineering, Middle East Technical University** by,

Prof. Dr. Halil Kalıpçılar  
Dean, Graduate School of **Natural and Applied Sciences**

\_\_\_\_\_

Prof. Dr. İsmail Hakkı Tuncer  
Head of the Department, **Aerospace Engineering**

\_\_\_\_\_

Prof. Dr. Sinan Eyi  
Supervisor, **Aerospace Engineering, METU**

\_\_\_\_\_

**Examining Committee Members:**

Prof. Dr. Yusuf Özyörük  
Aerospace Engineering Dept, METU

\_\_\_\_\_

Prof. Dr. Sinan Eyi  
Aerospace Engineering Dept, METU

\_\_\_\_\_

Prof. Dr. Dilek Funda Kurtuluş  
Aerospace Engineering Dept, METU

\_\_\_\_\_

Assist. Prof. Dr. Sıtkı Uslu  
Mechanical Engineering Dept., TOBB ETU

\_\_\_\_\_

Assist. Prof. Dr. Hediye Atik  
Aerospace Engineering Dept., Atılım University

\_\_\_\_\_

Date: 02.09.2021

**I hereby declare that all information in this document has been obtained and presented in accordance with academic rules and ethical conduct. I also declare that, as required by these rules and conduct, I have fully cited and referenced all material and results that are not original to this work.**

Name Last name : Tezcan Ünlü

Signature :

## **ABSTRACT**

### **DEVELOPMENT OF A DESIGN METHOD FOR SUBSONIC INTAKES WITH IMPROVED AERODYNAMIC PERFORMANCE AND REDUCED RADAR SIGNATURE**

Ünlü, Tezcan  
Master of Science, Aerospace Engineering  
Supervisor: Prof. Dr. Sinan Eyi

September 2021, 136 pages

In this thesis, a design method for a subsonic intake with high aerodynamic performance and reduced radar signature is developed. Intakes are key components of aircrafts' propulsion systems that create open ended cavities resulting in increased radar signature. To achieve reduced radar signature characteristics, a parameterized double curved intake is proposed. Due to the nature of this multi-objective and multi-disciplinary engineering problem, surrogate based analysis and optimization approach is taken to reduce the computationally expensive and time consuming analyses. The thesis consists of three main sections. In the first section, validation studies for the intake performance evaluation methods are conducted. Mesh independence and turbulence model selection studies are carried out for the computational fluid dynamics analyses and radar cross section evaluation studies are carried out for the electromagnetic analyses. In the second section, a design problem is constructed and the verified analyses methods are used for the performance evaluation of the design points required by the surrogate model. Then the best performing design in terms of aerodynamics and radar cross section is obtained with

an optimization study. In the last section, analyses with high fidelity prediction tools are conducted for the validation of the obtained design and the design method. Results showed that the surrogate based model is successful at the prediction of performance indicators and can be used for intake optimization purposes. Lastly the performance of the best design is investigated with post-process outputs revealing competitive results regarding aerodynamics and radar signature.

Keywords: Subsonic Intake Design, Computational Fluid Dynamics, Radar Cross Section, Surrogate-based Optimization

## ÖZ

### İYİLEŞTİRİLMİŞ AERODİNAMİK PERFORMANSA VE AZALTILMIŞ RADAR İZİNE SAHİP SES ALTI HAVA ALIKLARI İÇİN TASARIM YÖNTEMİ GELİŞTİRİLMESİ

Ünlü, Tezcan  
Yüksek Lisans, Havacılık ve Uzay Mühendisliği  
Tez Yöneticisi: Prof. Dr. Sinan Eyi

Eylül 2021, 136 sayfa

Bu tezde, yüksek aerodinamik performansa ve düşük radar izine sahip ses altı hava alığı tasarım yöntemi geliştirilmiştir. Hava araçlarının itki sistemlerinin önemli bir parçası olan hava alıkları, açık uçlu kavite oluşturarak yüksek radar izine sebep olmaktadır. Düşük radar izi karakteristiklerini sağlama adına parametrik çift eğimli bir hava alığı önerilmiştir. Bu çok hedefli ve çok disiplinli mühendislik probleminin doğası gereği, vekil tabanlı analiz ve eniyilime yöntemi kullanılarak hesaplamasal olarak pahalı ve zaman alıcı analizler azaltılmıştır. Bu tez üç ana kısımdan oluşmaktadır. İlk kısımda hava alığı performansı değerlendirme yöntemleri için doğrulama çalışmaları gerçekleştirilmiştir. Hesaplama akışkanlar dinamiği analizleri için çözüm açısından bağımsızlık ve türbülans modeli seçim çalışmaları, elektromanyetik analizleri için radar kesit alanı hesaplama çalışmaları gerçekleştirilmiştir. İkinci kısımda bir tasarım problemi oluşturulmuştur ve vekil tabanlı modelin ihtiyaç duyduğu tasarım noktalarının performans değerlendirilmesinde doğrulanmış analiz yöntemleri kullanılmıştır. Ardından bir optimizasyon çalışmasıyla aerodinamik ve radar kesit alanı yönlerinden en iyi performansa sahip tasarım elde edilmiştir. Son kısımda, yüksek doğruluklu kestirim

araçları kullanılarak gerçekleştirilen analizlerle, elde edilen tasarım ve tasarım yöntemi doğrulamaları gerçekleştirilmiştir. Sonuçlar vekil tabanlı modelin performans göstergelerinin kestiriminde başarılı olduğunu ve hava alığı eniyileme amacıyla kullanılabileceğini göstermiştir. Son olarak, en iyi tasarımın performansı ard işleme çıktılarıyla incelenerek aerodinamik ve radar izi açılarından rekabetçi sonuçları ortaya çıkarılmıştır.

Anahtar Kelimeler: Ses Altı Hava Alığı Tasarımı, Hesaplmalı Akışkanlar Dinamiği, Radar Kesit Alanı, Vekil Tabanlı Eniyileme

To my family

## **ACKNOWLEDGMENTS**

I would like to express my deepest gratitude to my supervisor Prof. Dr. Sinan Eyi for his support and guidance throughout the thesis.

I would like to thank my colleagues in Aerodynamics Design and Analysis team of ROKETSAN for their knowledge, comments and support during the thesis.

I am forever thankful to my parents Mrs. Meral Ünlü, Mr. Tevfik Ünlü and my sister Mrs. Firuze Evşen Özen for their support, love and motivation.

I am forever in debt to my lovely wife, Gülsüm Ünlü. Without her support, tolerance, motivation and love, this work could not pass half way.

## TABLE OF CONTENTS

ABSTRACT.....	v
ÖZ.....	vii
ACKNOWLEDGMENTS .....	x
TABLE OF CONTENTS.....	xi
LIST OF TABLES .....	xiv
LIST OF FIGURES .....	xvi
LIST OF ABBREVIATIONS .....	xx
LIST OF SYMBOLS .....	xxii
1 INTRODUCTION .....	1
1.1 Background .....	1
1.2 Air Intakes for Stealth Applications .....	8
1.3 Design Methodology.....	11
1.4 Literature Survey .....	12
1.5 Aim of the Thesis.....	14
1.6 Outline of the Thesis .....	14
2 METHODOLOGY .....	17
2.1 Intake Geometry Parameterization .....	17
2.1.1 Lip Section with Throat Station .....	18
2.1.2 1 <sup>st</sup> Duct Section with Middle Station .....	21
2.1.3 2 <sup>nd</sup> Duct Section with AIP Station.....	26
2.2 Design with Response Surface Methodology .....	31
2.2.1 DOE Study Method .....	34

2.2.2	Surrogate Model Generation Method .....	35
2.2.3	Design Optimization Method.....	36
2.3	CFD Overview.....	38
2.3.1	Pre-Process Overview .....	38
2.3.2	CFD Analysis Overview .....	41
2.3.3	CFD Post-Process Overview .....	46
2.4	RCS Overview.....	47
2.4.1	Electromagnetics Basics .....	48
2.4.2	RCS Prediction Methods .....	51
2.4.3	RCS Evaluation Method .....	53
3	VALIDATION STUDIES.....	59
3.1	CFD Validation Studies.....	59
3.1.1	RAE M2129 Intake Test Case .....	59
3.1.2	S-Shaped Duct Test Case.....	67
3.1.3	CFD Validation Overview .....	75
3.2	RCS Validation Studies.....	76
3.2.1	Triangular Prism Benchmark Test Case .....	76
3.2.2	Truncated Cone Benchmark Test Case.....	78
3.2.3	Simple Duct Test Case.....	81
3.2.4	RCS Validation Overview .....	83
4	INTAKE DESIGN PROCESS .....	85
4.1	Design Problem Description.....	85
4.2	Definitive Screening Design Study .....	92
4.2.1	DSD – PR Investigation.....	93

4.2.2	DSD – DC Investigation .....	94
4.2.3	DSD – RCS Investigation .....	95
4.2.4	DSD Overview .....	96
4.3	DOE Study .....	96
4.3.1	DOE - Investigation .....	99
4.3.2	DOE - Overview .....	101
4.4	Surrogate Model Generation .....	101
4.5	Optimization .....	105
4.5.1	Optimization Results .....	105
4.5.2	Optimization Discussion .....	112
5	VALIDATION AND DISCUSSION OF THE RESULTS .....	115
5.1	Validation Results of the Optimized Intake .....	115
5.1.1	CFD Post-Process Outputs .....	116
5.1.2	RCS Post-Process Outputs .....	121
5.2	Discussion of the Validation Results .....	126
6	CONCLUSION AND FUTURE WORK .....	129
	REFERENCES .....	133

## LIST OF TABLES

### TABLES

Table 2.1. 1 <sup>st</sup> Duct Centreline Boundary Conditions .....	23
Table 2.2. 2 <sup>nd</sup> Duct Centreline Boundary Conditions.....	28
Table 2.3. Parameters of the Study.....	31
Table 3.1 RAE M2129 Model Dimensions [19] .....	60
Table 3.2 RAE M2129 Test Conditions [19] .....	61
Table 3.3 RAE M2129 Performance Outputs [19].....	61
Table 3.4. RAE M2129 Mesh Independence Study Mesh Details .....	63
Table 3.5 RAE M2129 Mesh Independence Study Results .....	65
Table 3.6 RAE M2129 Mesh Independence Study Turbulence Investigation Results .....	66
Table 3.7 S-Shaped Duct Test Conditions [43].....	68
Table 3.8 S-Shaped Duct Performance Outputs [43] .....	69
Table 3.9 S-Shaped Duct Mesh Independence Study Mesh Details .....	71
Table 3.10 S-Shaped Duct Mesh Independence Study Results.....	74
Table 3.11 S-Shaped Duct Mesh Independence Study Turbulence Investigation Results .....	75
Table 3.12 Triangular Prism Test Conditions [21].....	77
Table 3.13 Truncated Cone Test Conditions [21] .....	79
Table 3.14 Simple Duct Test Conditions [22].....	82
Table 4.1 Design Point Flight Conditions .....	86
Table 4.2 Design Intake Lip Dimensions .....	88
Table 4.3 Design Space Parameter Limits .....	90
Table 4.4. Design RCS Conditions.....	91
Table 4.5. DSD – Design Details and Results .....	92
Table 4.6. DOE – Design Details and Results.....	97
Table 4.7. Surrogate Model Performance Outputs .....	104

Table 4.8 Surrogate Model Cross-Validation Results .....	105
Table 4.9 Design Optimization Input Limitations .....	106
Table 4.10 Design Optimization Objectives .....	106
Table 4.11 Design Optimization Constraints.....	106
Table 4.12 Design Optimization Performance Output Results.....	107
Table 4.13 Design Optimization Variable Results .....	108
Table 4.14 Design Optimization Best Performing Design Comparison.....	110
Table 4.15 Best Design Performance Outputs .....	110
Table 5.1 Validation Results and Comparison .....	115
Table 5.2 Optimization and Validation Results Comparison .....	127

## LIST OF FIGURES

### FIGURES

Figure 1.1. Simple Turbojet Engine Illustration [2] .....	2
Figure 1.2. AIP Definitions. (a) Pressure Probe Placements; (b) Sector Definition for DC60 [4] .....	4
Figure 1.3. Intake Types. (a) Integrated Intake; (b) Podded Intake [2] .....	5
Figure 1.4. Submerged Intake - Tomahawk Missile [6] .....	6
Figure 1.5. Semi-submerged Intake - ATMACA Missile [7] .....	7
Figure 1.6. Pitot Intake - NSM Missile [8] .....	7
Figure 1.7. Illustration of the Propagation of a Radar Wave Inside a Duct [11] .....	9
Figure 1.8. F35 Lightning II [13] .....	10
Figure 1.9. SOM-J Missile [14] .....	10
Figure 2.1. Intake Sections and Stations .....	18
Figure 2.2. Intake Capture Area .....	19
Figure 2.3. Intake Dimensional Definitions .....	19
Figure 2.4. Intake Angular Definitions. (a) Upper Lip Horizontal Angle; (b) Lower Lip Horizontal Angle; (c) Lip Vertical Angle .....	20
Figure 2.5. Intake Lip Airfoil Profile and Swept Surface Profile .....	21
Figure 2.6. 1 <sup>st</sup> Duct Centreline and Stations .....	22
Figure 2.7. 1 <sup>st</sup> Duct Dimensional Parameters .....	22
Figure 2.8. Middle Station Profile and Parameters .....	25
Figure 2.9. Stations Closer to Lip and Middle Stations .....	26
Figure 2.10. 1 <sup>st</sup> and 2 <sup>nd</sup> Duct Centrelines and Stations .....	27
Figure 2.11. 2 <sup>nd</sup> Duct Dimensional Parameters .....	27
Figure 2.12. Response Surfaces. (a) Simple Maximum; (b) Saddle, [30] .....	32
Figure 2.13. SBAO Method Schematic .....	33
Figure 2.14. CFD Flow Field Samples .....	39
Figure 2.15. Sample Flow Field Meshes .....	40
Figure 2.16. Sample Mesh with Refinement Regions .....	41

Figure 2.17. CFD Analysis Approach Schematic .....	45
Figure 2.18. DC Sector Definition .....	47
Figure 2.19. Electromagnetic Wave [39] .....	48
Figure 2.20. Monostatic and Bistatic Radar Configurations [40] .....	49
Figure 2.21. Aircraft Echo Scattering Mechanisms [10] .....	50
Figure 2.22. RCS Analysis Model .....	54
Figure 2.23. RCS Analysis Illumination Outlines .....	55
Figure 2.24. RCS Analysis Illumination $\theta$ Sweeps.....	55
Figure 2.25. Gaussian Modifier for $\theta$ Angle Sweeps.....	57
Figure 3.1. RAE M2129 Model (dimensions in mm) .....	60
Figure 3.2. RAE M2129 Boundary Conditions .....	62
Figure 3.3. RAE M2129 Mesh Independence Study – Coarse Mesh .....	63
Figure 3.4. RAE M2129 Mesh Independence Study – Medium Mesh.....	63
Figure 3.5. RAE M2129 Mesh Independence Study – Fine Mesh .....	64
Figure 3.6. RAE M2129 Mesh Independence Study PR Results with Experimental Results [19] .....	64
Figure 3.7. RAE M2129 Mesh Independence Study DC Results with Experimental Results [19] .....	65
Figure 3.8. RAE M2129 $y^+$ Output of the “Medium” Mesh .....	66
Figure 3.9. S-Shaped Duct Model Details [43].....	67
Figure 3.10. S-Shaped Duct Computational Model.....	69
Figure 3.11. S-Shaped Duct Boundary Conditions.....	70
Figure 3.12. S-Shaped Duct Mesh Independence Study – Very Coarse Mesh.....	71
Figure 3.13. S-Shaped Duct Mesh Independence Study – Coarse Mesh.....	71
Figure 3.14. S-Shaped Duct Mesh Independence Study – Medium Mesh .....	72
Figure 3.15. S-Shaped Duct Mesh Independence Study – Fine Mesh.....	72
Figure 3.16. S-Shaped Duct Mesh Independence Study PR Results with Experimental Results [43].....	73
Figure 3.17. S-Shaped Duct Mesh Independence Study DC Results with Experimental Results [43].....	73

Figure 3.18. S-Shaped Duct $y^+$ Output of the “Medium” Mesh .....	74
Figure 3.19. Triangular Prism Model .....	77
Figure 3.20. Triangular Prism Results Comparison with Experimental Data [21] ..	78
Figure 3.21. Truncated Cone Model.....	79
Figure 3.22. Truncated Cone Results Comparison with Experimental Data [21]...	80
Figure 3.23. Simple Duct Experimental Model [22] .....	81
Figure 3.24. Simple Duct Model .....	82
Figure 3.25. Simple Duct Results Comparison with the Experimental Data [22] ..	83
Figure 4.1. Design AIP Geometry Dimensions .....	87
Figure 4.2. Design Intake Lip Dimensional Details .....	89
Figure 4.3. Design Space Limits .....	90
Figure 4.4. Middle Station Profile Examples .....	91
Figure 4.5. DSD – PR Results .....	94
Figure 4.6. DSD – DC Results .....	94
Figure 4.7. DSD – RCS Results .....	95
Figure 4.8. DOE – PR Results.....	99
Figure 4.9. DOE – DC Results .....	100
Figure 4.10. DOE – RCS Results .....	100
Figure 4.11. Surrogate Model PR Output.....	102
Figure 4.12. Surrogate Model DC Output .....	103
Figure 4.13. Surrogate Model RCS Output .....	103
Figure 4.14. Design Optimization PR Investigation .....	109
Figure 4.15. Design Optimization DC Investigation.....	109
Figure 4.16. Design Optimization RCS Investigation.....	109
Figure 4.17. Optimized Intake Duct Isometric View .....	111
Figure 4.18. Optimized Intake Duct Dimensions .....	111
Figure 4.19. Optimized Intake Duct Middle Station Dimensions .....	112
Figure 5.1. Mach Contour of the Validation Case.....	116
Figure 5.2. Mach Contours of the Main Stations .....	117
Figure 5.3. Mach Streamline Inside the Duct.....	118

Figure 5.4. Mach Streamlines with Main Station Mach Contours.....	118
Figure 5.5. Flow Field Total Pressure Contour.....	119
Figure 5.6. PR Contour at the Throat Station .....	120
Figure 5.7. PR Contour at the Middle Station .....	120
Figure 5.8. PR Contour at the AIP Station.....	121
Figure 5.9. RCS Values of the Optimized Intake .....	122
Figure 5.10. VTR Image of 1 <sup>st</sup> Bounce.....	123
Figure 5.11. VTR Image of 2 <sup>nd</sup> Bounce .....	123
Figure 5.12. VTR Image of 3 <sup>rd</sup> Bounce .....	124
Figure 5.13. VTR Image of 4 <sup>th</sup> Bounce.....	124
Figure 5.14. VTR Image of 5 <sup>th</sup> Bounce.....	125
Figure 5.15. VTR Image of Bounces .....	126

## LIST OF ABBREVIATIONS

### ABBREVIATIONS

AIP	Aerodynamic Interface Plane
B.C.	Boundary Condition
CFD	Computational Fluid Dynamics
CFL	Courant-Friedrichs-Lewy
DC	Distortion Coefficient
DOE	Design of Experiments
DSD	Definitive Screening Design
EM	Electromagnetics
GO	Geometrical Optics
HPC	High Performance Computer
IEEE	Institute of Electrical and Electronics Engineers
MFR	Mass Flow Rate
NACA	National Advisory Committee for Aeronautics
NASA	National Aeronautics and Space Administration
PEC	Perfect Electrical Conductor
PO	Physical Optics
PR	Pressure Recovery
PTD	Physical Theory of Diffraction
RAM	Radar Absorbent Material
RANS	Reynolds Averaged Navier-Stokes
RCS	Radar Cross Section
RPM	Revolution per Minute
RSM	Response Surface Method
SBAO	Surrogate-based Analyses and Optimization
SBR	Shooting and Bouncing Ray
UAV	Unmanned Air Vehicle

UTD      Universal Theory of Diffraction  
VRT      Visual Ray Tracing

## LIST OF SYMBOLS

### SYMBOLS

$A$	Area
$E$	Total Energy
$E$	Wave Strength
$\varepsilon$	Turbulent Dissipation Rate
$\vec{f}_e$	Body Force
$k$	Turbulent Kinetic Energy
$I$	Unit Tensor
$\vec{n}$	Normal of the Surface
$P$	Pressure
$\dot{q}_h$	Heat Transfer Rate
$q$	Dynamic Head
$\rho$	Density
$R$	Universal Gas Constant
$R$	Distance from the Target
$dS$	Surface Element of the Volume Control
$\mu$	Dynamic Viscosity
$T$	Static Temperature
$\bar{\tau}$	Stress Tensor
$\omega$	Specific Dissipation Rate
$\Omega$	Small Portion of the Control Volume
$\vec{v}$	Velocity
$y^+$	Dimensionless Wall Distance
$\sigma$	Radar Cross Section
$\nabla$	Gradient Operator
$\varphi$	Solution Variable

$\theta$	Circular Angle
$\phi$	Azimuth Angle
$\theta$	Elevation Angle

#### Subscripts

Ave	Average
$\infty$	Free Stream
T	Total
Max	Maximum
Min	Minimum
Mod	Modified



# CHAPTER 1

## INTRODUCTION

Intakes are one of the key components of air breathing propulsion systems. Having a primary role of delivering quality air to a gas turbine engine, intakes and their performance are crucial for the performance of the propulsion system and the airframe. The shape of the intakes are also deciding for the low observability of an airframe since intake and the compressor/fan face create an open ended cavity acting as a reflector for radar waves.

In this thesis, a design method for an S-shaped subsonic intake with low observable characteristics is proposed. The proposed method includes the design of a double curved intake for achieving lower radar cross section while maintaining the highest aerodynamic performance. Double curved duct is expected to lower the radar cross section by increasing incident radar wave bounces on surfaces. However losses caused by the adverse pressure gradients on the double curved duct walls decrease the pressure recovery and increase the distortion at compressor entry plane, creating a design problem. Due to the nature of this multi parameter and multi objective problem, a parameter effectiveness, a design of experiments (DOE) and a response surface approach is implemented into the design method.

### 1.1 Background

Most of the aircrafts rely on air breathing systems as the mean of propulsion and gas turbine engines form the majority of the said systems. The fact that the gas turbine engines opened a new way of propulsion with lower engine weight and size than piston engines makes these engines favourable for high speed aircrafts [1]. Design,

development and integration of airframes and gas turbine powered propulsion systems created a multidisciplinary engineering problem investigated since the development of gas turbine engines at 1930's. The mentioned multidisciplinary problem requires that the design of the airframe, the design of the propulsion system and the integration of these to be done preferably in unison or separately with possible compromises in performance.

Gas turbine engines rely on air as the propelling fluid for thrust generation and the required air is supplied to the engine by a subsystem called intake. Although intakes are considered as a subsystem of the propulsion systems, being a subsystem that affects both the performance of the engine and the airframe make intakes an integrating and a vital component of the aircraft system. A simple turbojet engine with stations marking engine subsystems including the intake is given in Figure 1.1.

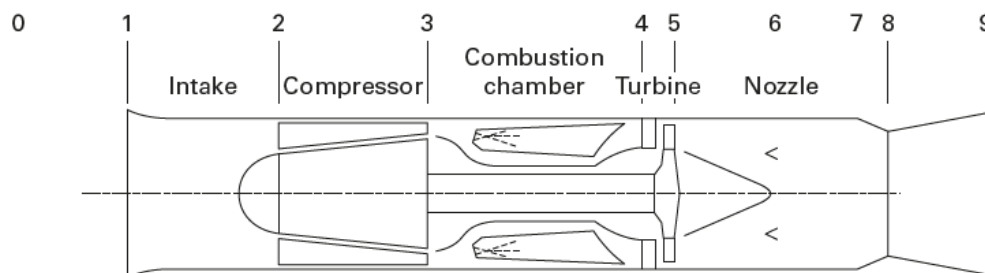


Figure 1.1. Simple Turbojet Engine Illustration [2]

An intakes' main role is providing a specific amount of air to the engine with high efficiency. Achieving this role requires dealing with the changing flow conditions from the freestream (Station-0) to the entrance of the compressor set by the engine (Station-2) [3]. Efficiency of intakes is decided by several factors with the most important one being the pressure recovery. Total pressure recovery (PR) defines how much the freestream total pressure is recovered (or maintained) at a place defined as aerodynamic interface plane (AIP) which is considered as an agreed upon interface between the engine and the intake. Other important efficiency indicators are intake distortion, drag, weight, complexity, cost, etc. [3]. Intake distortion is defined as the

non-uniform flow properties occurring at the engine compressor/fan faces that affects the reliability of the engine's operation. From the aerodynamics design aspect of intakes, pressure recovery, intake distortion and drag can be regarded as the most important performance parameters. These design and performance parameters are detailed in the list below.

- PR show how much of the freestream flow properties is delivered to the engine by the intake subsystem. Since intakes do not do thermodynamic work on the flow, total pressure across the intake decreases according to shape of the duct, flow conditions of the freestream and the engine airflow demands. The decrease of the PR is associated with several flow effects like the flow separation and boundary layer formation inside the duct.
- The non-uniformities at the engine compressor/fan face, defined as the intake distortion, can lead to serious reliability issues by causing compressor surge with reduced compressor surge margin, mechanical damage due to blade fatigue and vibration and also generating noise [2], [3]. The total pressure distortion is associated with flow separations and wakes originating inside the duct or caused by lip surfaces [4]. Distortion can especially occur on off-design points and the amount of distortion is driven by the shape and sizing of the duct and lip design. Unlike PR, there is not a universally agreed descriptor for the distortion, so several descriptors developed by engine companies are used. These descriptors originated from the experimental distortion calculation methods that are simply using pressure measurement probes radially placed at rakes at the AIP. A simple image of the said pressure probes are given in Figure 1.2.

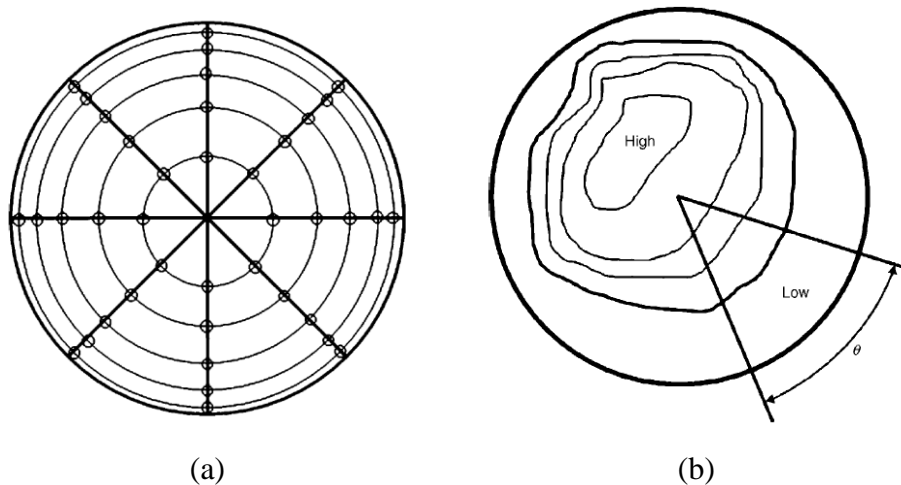


Figure 1.2. AIP Definitions. (a) Pressure Probe Placements; (b) Sector Definition for DC60 [4]

DC60 is one of the most used distortion descriptors and it quantifies distortion by forming a coefficient using average pressure values of sectors at the AIP. The pressure of the sector having the lowest value decides the DC60 value and a sample image showing the said sector is given in Figure 1.2.

- Drag is another performance parameter and like any other subsystem of an aircraft, lower drag is aimed for intakes. The drag consideration highly depends on the airframe type, role and intake configuration. Intake elements like duct shape, lip and nacelle (or external shell) are the largest drag contributors for subsonic applications. So the design phase should include the considerations regarding the configuration types.

The intake duct shape is the intake design element that the detailed performance parameters all have in common and the shaping is done according to the intake configuration driven by the airframe type and its intended role. Now that the basic intakes and their performance parameters are defined, the effect of the airframe on the sizing and configuration of intakes will be focused on.

As this thesis is focused on subsonic/transonic intakes, small scale aircrafts like unmanned vehicle systems are selected as airframes. The roles of the UVSs vary

from surveillance, target and attack drones to cruising missiles [1]. A big portion of high subsonic/transonic applications of these systems rely on turbojet engines. These systems have smaller footprint in size with respect to fighter jet aircrafts and aim to achieve minimal cost with the best performance according to their role. Intended role and the size of these systems drive the propulsion system selection/design and the intake system configuration selection is done according to these considerations.

Intakes on the mentioned systems can be categorized as “podded” and “integrated” implementations [5]. Both types of intakes are selected according to the airframe needs. Podded types allow clear internal flow reaching to the engine with less complex flow dynamics inside the duct but engine needs to be cased with nacelle or external shell that arises structural needs. Integrated types allow the engine to be placed in the airframe axially centred eliminating the need for a nacelle but the flow inside the duct gets complex with the duct usually requiring bends. Sample implementation examples of these types of intakes on a bigger scale passenger aircraft is shown in Figure 1.3.

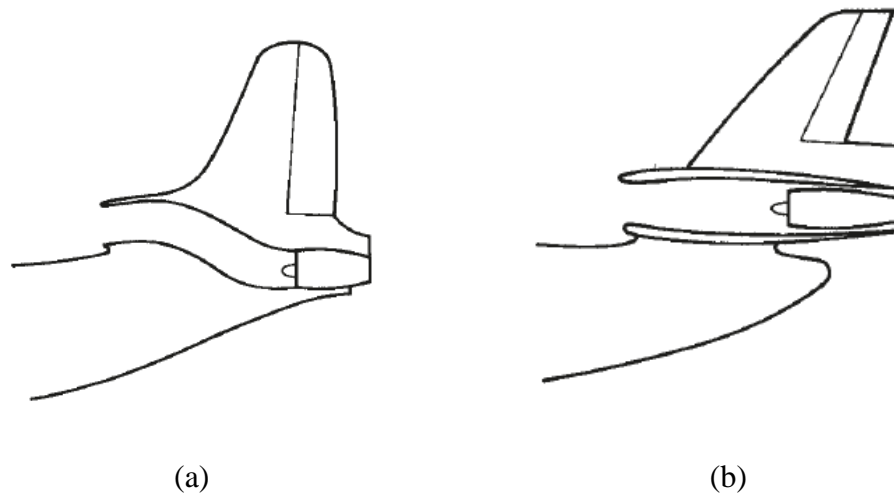


Figure 1.3. Intake Types. (a) Integrated Intake; (b) Podded Intake [2]

Another consideration regarding the integrated intakes is that the integrated type offers stealth advantage over podded ones with a large cross sectional area of the

propulsion system kept hidden inside the fuselage. Considering the mentioned small scale UVSs, integrated intake applications are widely implemented regarding the weight, structural and stealth demands even though complex flow formations occur inside the duct.

Integrated type intakes can also be categorized as submerged or flushed (NACA) type, semi-submerged type and pitot type. All these types of integrated intakes have several advantages and disadvantages over each other regarding aerodynamics and stealth properties. Sample intake images implemented for missiles for these types are shown in Figure 1.4, Figure 1.5 and Figure 1.6.



Figure 1.4. Submerged Intake - Tomahawk Missile [6]



Figure 1.5. Semi-submerged Intake - ATMACA Missile [7]

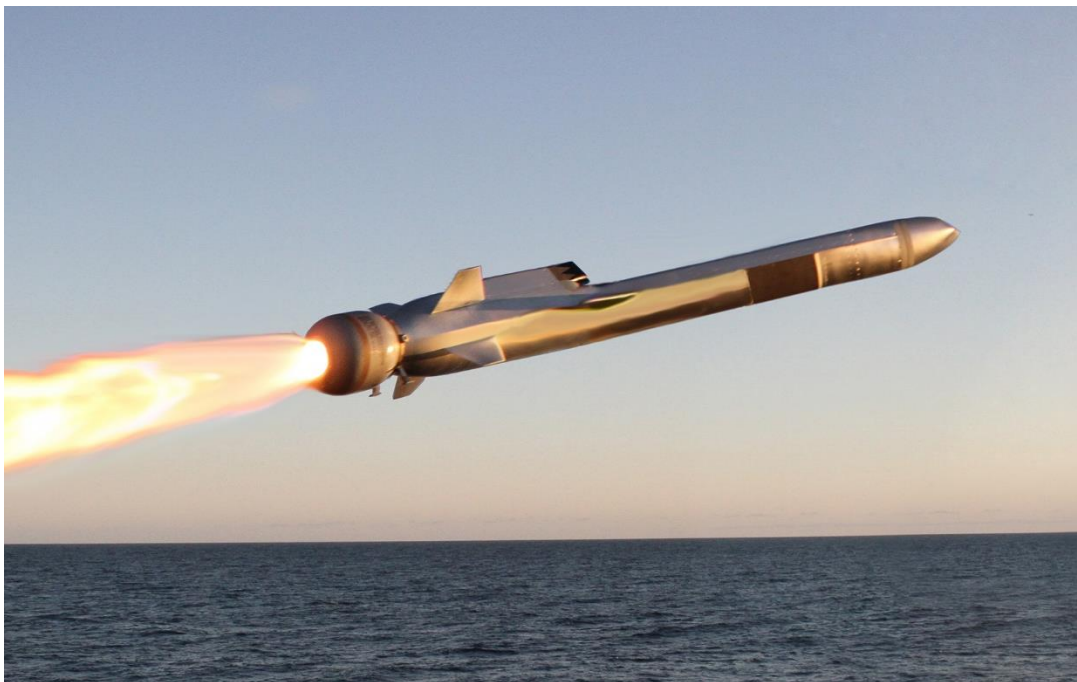


Figure 1.6. Pitot Intake - NSM Missile [8]

For the given types of intakes, aerodynamics performance is affected by the placement of the intake with respect to airframe body. While the submerged intakes offer smaller cross-sectional area and hence having lower drag property, the flow with a boundary layer formed over the airframe body entering the duct makes submerged intakes prone to possess lower PR values [3]. Likewise, pitot type intakes offer good PR values with a possible drag disadvantage. Semi-submerged intakes offer an option between the submerged and pitot types, carrying both their advantages and disadvantages. Sizing and geometrical limitations of the aircraft,

operational and stealth demands of the aircrafts and the demands of the engine are the parameters that drive the selection of the intake type. The stealth aspect that affect the intake design is investigated in the following section.

## **1.2 Air Intakes for Stealth Applications**

Stealth is a more and more desired feature that military aircrafts intend to possess. An aircraft is said to be stealth if it has low observable characteristics that help it avoid detection from opposing forces. The detection technologies consists of radar systems and visual/acoustic detection technologies with the former one being the most used and popular one since World War 2. The observability of an aircraft to a radar system is decided by its shape and the use of electronic protection technologies. The amount of detectability is defined with a unit of measure called radar cross-section (RCS) and it simply denotes the amount of radar energy radiated (scattered) from the object back to the radar system. This amount is driven by both the properties of the radar system and the target object.

Aircrafts having complex geometries consisting of multiple components are great scatterers of radio waves caused by several electromagnetic phenomena. Among these components, intakes are one of the major contributors to the overall RCS signature of an aircraft [9]. The reason behind the importance of intakes is that intakes form an open ended cavities that tend to reflect a fair amount of radar energy back to the radar receiver [10]. A sample image of the propagation of a radar wave inside a duct is given in Figure 1.7.

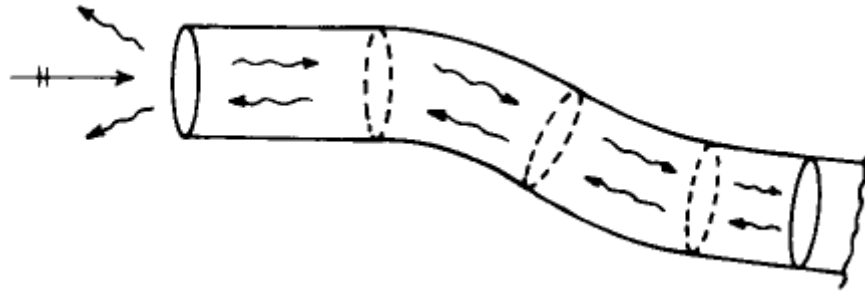


Figure 1.7. Illustration of the Propagation of a Radar Wave Inside a Duct [11]

A study given in [12] shows that for a small drone, the intake edges and intake interior components are the main RCS contributors for the nose-on radar threat angles along with the tips of the wings and tails.

To lower the radar signature caused by intakes, firstly the intake configuration selection can be made according to the demand and then several echo reduction methods can be applied. Considering the integrated intake types mentioned in 1.1, intakes with smaller cross-sectional footprint like submerged intakes are expected to have smaller radar signature contribution. For all intake types, RCS reduction methods like shaping, using absorbing materials and cancellation technologies can be used. Among these methods, shaping of the intake elements to prevent back scattering is an effective one. Mentioned shaping method includes the surfaces of the lip geometry, diverters (for pitot type intakes) and the ducts. The manipulation of the duct surfaces to hide the compressor of the engines is a common practice used by fighter jets and UVSs with a sample image of F35 Lightning II given in Figure 1.8. Even though the intake duct lays in the airframe axially, with duct shaping the compressor face is hidden from nose-on angles. For the UVSs with S-duct intake systems, the bent duct surfaces help hiding compressor face.



Figure 1.8. F35 Lightning II [13]

Lip shaping is also implemented to lower the radar signature by diverting the incoming radar waves to directions other than the radar receiver. Lip shaping is a challenging problem that requires the surfaces to be designed flatter rather than circular/elliptical with surfaces angled between each other. As this method contradicts the aerodynamic practices like the duct shaping, optimization bringing the best of both practices are applied. A sample image of SOM-J missile with the implementation of lip shaping is given in Figure 1.9.

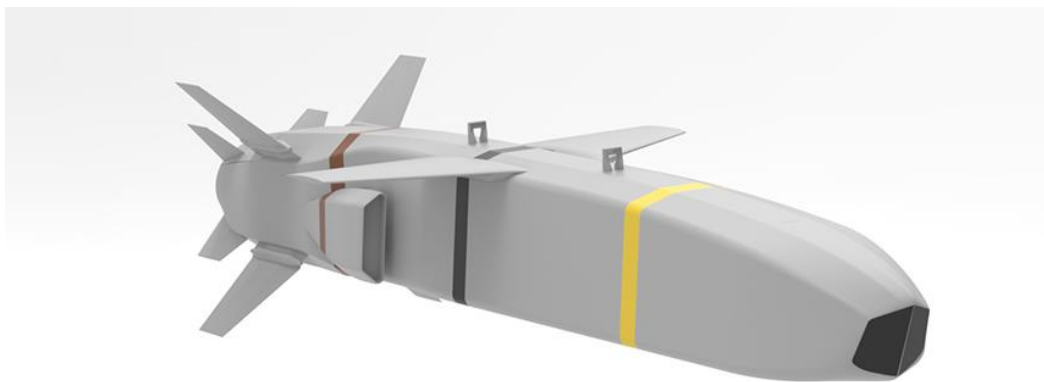


Figure 1.9. SOM-J Missile [14]

Using radar observant materials and implementing cancellation methods are other counter measures along with the shaping precautions and these are often used together.

Considering the mentioned aerodynamics aspects of intake types, using pitot type intakes with the signature precautions applied is a common practice followed by the recent missile systems like NSM, JSM, SOM and SOM-J. In this thesis a similar approach will be taken focusing on duct shaping to reduce the intake signature while achieving highest aerodynamic performance with a pitot type intake. Proposed method of design along with the literature survey is introduced in the following sections.

### **1.3 Design Methodology**

Current design methodology for intakes consist of a multi-objective iterative process utilizing several sub-processes that belong to different disciplinary fields. The engineering problem of intake design has become more challenging throughout the years that more complex geometries and systems are required due to the demand of more capable or combat effective air vehicles. Shape optimization is an important part of this problem and it is generally carried out with CFD softwares coupled with optimization algorithms [15]. Assessment of the performance values of aerodynamics and signature mentioned in 1.1 and 1.2 are done with prediction tools that require high performance computers (HPCs) as they often employ computationally costly analyses.

Using the high accuracy prediction tools for the design and optimization of aircraft subsystems like intakes create a computationally expensive and time consuming problem that can be overcome by using the methodology of surrogate-based analysis and optimization (SBAO) [16]. SBAO allows obtaining a process's output for given inputs with a mathematical model [17]. In SBAO method, high-fidelity simulations are carried out at design points in a design space and these points are decided by a design of experiment (DOE) study. Obtained design point results are fed to a surrogate construction tool and the obtained model is used in an optimization algorithm. Since the obtained model offers a lower fidelity solution, the quality of the results are validated using high-fidelity tools or experimentation. With the

explained SBAO methodology, the design process can be handled efficiently that would be otherwise expensive and time consuming with high-fidelity tools and gradient-based or stochastic optimization methods.

Another advantage of the SBAO methodology is that it allows the investigation of variables' (factors) effect on performance parameters (responses) thanks to the DOE sampling process and also instant access to generated design point's performance values which can be useful in an early design stage of a system. In the following section, the literature survey on the topics mentioned in 1.1, 1.2 and 1.3 is covered.

#### **1.4 Literature Survey**

The studies and reviews in the literature on intake design, CFD and RCS validation and optimization methods are covered in this section. Validation studies are crucial for the validation of the high-fidelity tools of CFD and RCS as the SBAO methodology requires. Since the studies on intake design and validation are often confidential due to secrecy reasons, literature work is scarce but similar concepts are available in a limited amount.

On the CFD validation studies, fluid dynamics problem of an S-shaped channel is highly investigated in literature with one of the most researched on is carried out in [18] with a generic S-duct diffuser. This study investigates the separation in a highly curvature duct and also includes experimental data. Since the focus of this thesis is on a pitot type intake with a full sized lip geometry, another highly researched study is presented in [19] that features an S-duct high curvature intake operating at subsonic regime. The same intake is also researched in [20] and the comparisons are carried out with the experimental and computational results. In this thesis, fluid dynamics phenomena inside the duct are investigated with transient numerical analyses.

On the RCS validation studies, the literature studies are even scarcer especially for intakes with measured RCS data. There are numerous data for the validation of

electromagnetics prediction tools with generic geometrics like spheres, dihedrals, prisms and conic surfaces. A benchmark study is carried out in [21] with prismatic and conic surfaces that is useful for the validation of several electromagnetic phenomena. Another essential study is presented in [22] and it is on the RCS of a full-scale aircraft straight duct with and without compressor blades. This study is useful as it has the desired experimental RCS data of a duct. Other studies on duct-like geometries are carried out in [9], [23], [24] mainly for the purposes of electromagnetics code and method generation and investigation of ducts.

There are several intake design studies and parametric investigation studies carried out in the literature. Most of the work is done on integrated submerged UAV intakes with low observable characteristics. All of these ducts feature shielding of the engine compressor fans from direct nose-on threat angles. In [25], an intake design that features an axially swept duct surface is carried out with a parametric model studied with detailed CFD analyses. In [26], another submerged intake design is carried out that features a parametric intake model consisting of 2 S-shaped ducts. This study also puts emphasis on lip geometry design and the designed final intake geometry is investigated experimentally with detailed CFD analysis carried out at on-design and off-design points. In [27], a propulsion system design with a highly compact intake duct is carried out. In this study, an axially placed intake that features 2 S-shaped duct surfaces is studied which shows the current trend is favouring compact stealth designs.

Several studies are carried out with duct only geometries with high curvature S-shapes suitable for pitot-type intakes. In [15], a parametric intake design with a single S-duct surface is carried out considering both the aerodynamic and signature performances. The study approaches the design process with a gappy proper orthogonal decomposition method to minimize the computational cost. This detailed study shows that the intake design can be handled with a multidisciplinary approach while reducing the computation cost but lacks intake lip geometry in the design process. The thesis [28] and the study [29] feature designs of intakes with circular

and rectangular cross-sections respectively and utilizes evolutionary algorithms for the optimization processes.

There are numerous sources and studies on experimentation, design and optimization fields in the literature. In [30], an extensive guide on experimentation is given and it is used as a source of information on DOE methods. In [16], an extensive discussion on SBAO methodology is presented that is used in the design and optimization part of this thesis. Lastly in [17], Kriging, a popular surrogate construction method, is reviewed which is also used in the thesis.

## **1.5 Aim of the Thesis**

The aim of this thesis is to develop a design method for a double curved single S-duct intake that maximizes the aerodynamic performance and minimizes the radar signature. The proposed double curved duct is expected to lower the signature contribution of the intake to the overall aircraft with a possible aerodynamics performance penalty.

The engineering problem of this multidisciplinary design process is handled with a surrogate based optimization methodology to reduce the number of computationally expensive and time consuming computer analyses. After the methodology is established, a study is carried out with a decided design space and the performance of the design output is validated using high-fidelity computational tools. Also discussions on the proposed intake model are carried out.

## **1.6 Outline of the Thesis**

This thesis consists of 6 chapters. In chapter 1, basics of intakes, application of them to UVSSs, stealth considerations regarding intakes and intake design methodologies are introduced. Also the literature review on the topic of this thesis and the aim of this thesis are provided.

In chapter 2, information on the intake analyses and design methodology is presented. Extensive information on the parameterization of the proposed intake, design methodology with the response surface approach and the overview on the CFD and RCS analyses methods are provided.

In chapter 3, validation studies for the CFD and RCS analyses methods are covered. 2 validation cases for CFD validation and 3 validation cases for RCS validation are provided with the discussions on the results.

In chapter 4, intake design process for a selected design space is carried out. After generating the design problem, design point sampling, construction of the surrogate model and the optimization are conducted out in this section.

In chapter 5, the validation and discussion on the optimization output is presented. Discussions are made with several post-process results and deductions on the results are provided.

Finally in chapter 6, concluding remarks regarding the conducted studies and the recommendations for future works will be presented.



## CHAPTER 2

### METHODOLOGY

In this chapter the proposed method of design process will be described. The method starts with the parameterization of the intake geometry and carry on with the multi-objective optimization approach. Finally the overview of the CFD and RCS processes used in the optimization are covered.

#### 2.1 Intake Geometry Parameterization

Parameterization and the generation of intake geometry are essentially important parts of the design process for several reasons listed below:

- Parameters should define the intake geometry in a decided design space. Also design geometries should be valid for parameters' differentiating values as these designs will be used in the optimization processes.
- Planned optimization processes of Definitive Screening Design (DSD), Design of Experiments (DOE) and Response Surface Method (RSM) depend on the parameter count as it will decide studies' design number and the accuracy of these studies.
- Accurate generation of the intake model is important for CFD and RCS processes as the tools relevant to the analysis tools uses the shape of the geometries as input for performance calculations.

For the reasons listed, a conceptual intake geometry consisting several elements shown in Figure 2.1 is proposed which is a double curved intake duct. Proposed intake geometry consists of a quadrilateral intake lip, a conventional S-shaped duct part and a second S-shaped duct part connected with an elliptical section. Each duct parts have centre lines connected at the said elliptical section. Sample generated duct

image consisting of a lip, duct sections and throat, middle and aerodynamic interface plane (AIP) stations is shown in Figure 2.1.

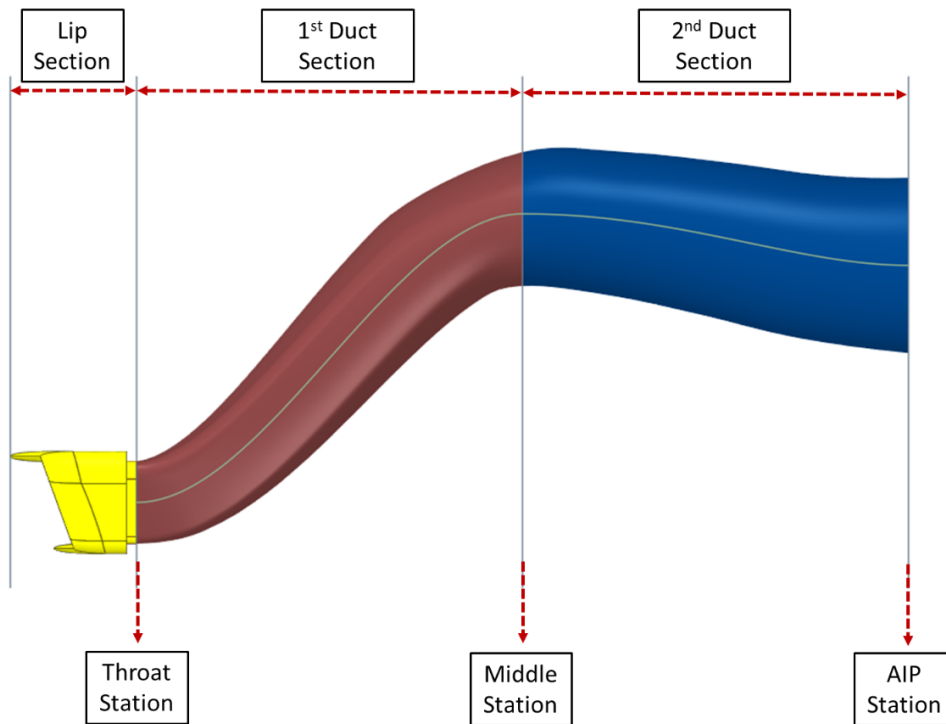


Figure 2.1. Intake Sections and Stations

The sections shown in Figure 2.1 along with the parameters defining the parametric model are explained in detail in subsections below.

### 2.1.1 Lip Section with Throat Station

The start of the first part of the intake has a rounded quadrilateral intake lip which has a fixed geometry and consists of the capture section and throat section. The intake lip shape, the area of the capture section and the throat are fixed and will not be variables in the parametric model. It is decided so that to lower the parameters in the optimization studies. Sample generated intake lip model and its details are shown in Figure 2.2. The capture area (marked with yellow lines) and the throat area (marked with red surface) can be seen on Figure 2.2 and Figure 2.3.

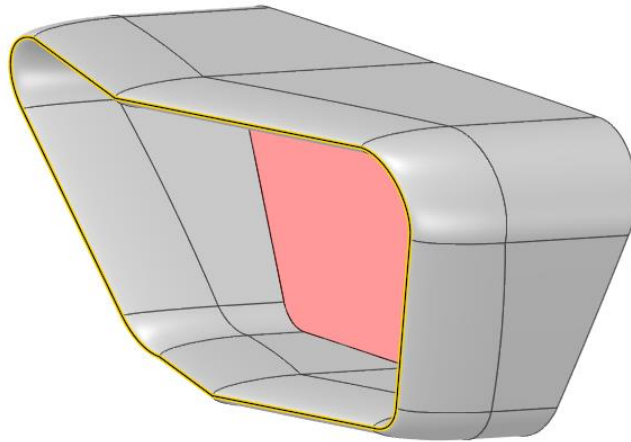


Figure 2.2. Intake Capture Area

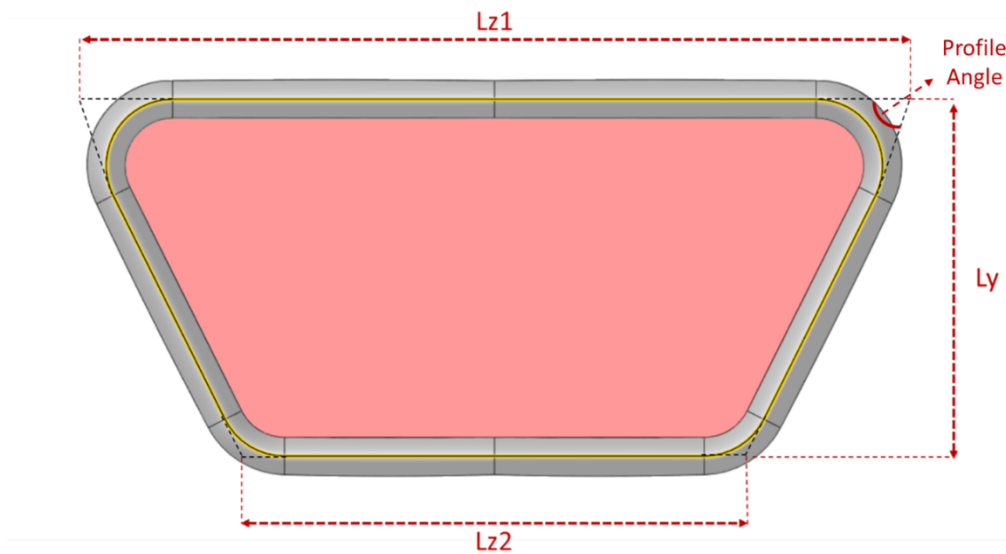


Figure 2.3. Intake Dimensional Definitions

The inlet lip has swept profile features angled both horizontally and vertically. Horizontal angle feature is to assure that incoming incident plane wave is not directed towards the radar wave source and diverted according to the horizontal angle called “V-angle”. The V-angle is applied on the upper and lower profiles. Vertical angle feature has a different purpose which is to prevent the incident plane wave

bouncing on the airframe from entering the duct and lowering the chance of scattering back through multiple bounces. Mentioned horizontal and vertical angles can be seen on Figure 2.4.

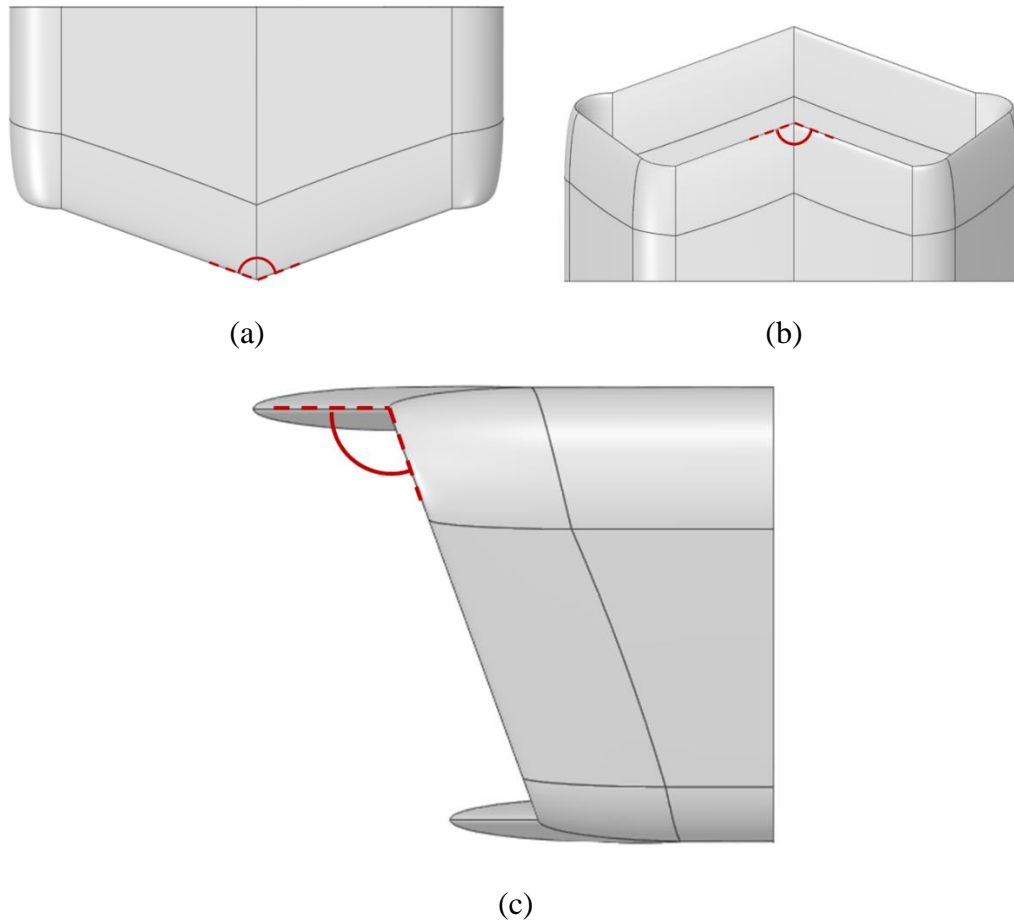


Figure 2.4. Intake Angular Definitions. (a) Upper Lip Horizontal Angle; (b) Lower Lip Horizontal Angle; (c) Lip Vertical Angle

The swept lip profile is a NACA 1-series airfoil (NACA 16-015) that is swept along the line defined by the  $Lz1$ ,  $Lz2$ ,  $Ly$  lengths and the V-angle, vertical angle and profile angle. Related airfoil profile (marked with yellow line) and the swept surface profile can be seen on Figure 2.5.

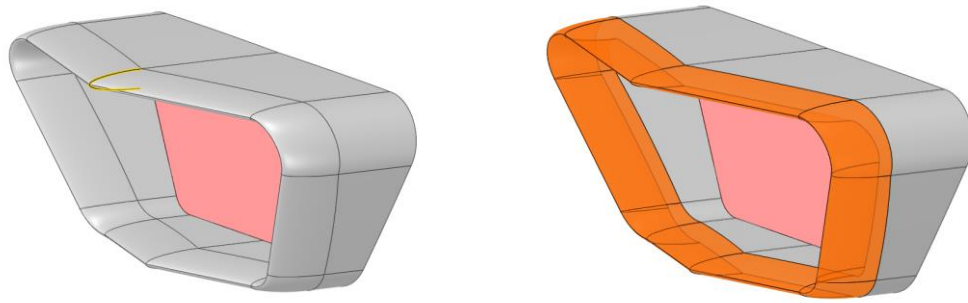


Figure 2.5. Intake Lip Airfoil Profile and Swept Surface Profile

Proposed inlet lip profile has a longer upper edge (Lz1) than the lower edge (Lz2). This is to achieve “Gerlach Shaping” in S-inlets [31], to have the higher energy flow on the inside turning of the duct. Area of the capture area and the throat area are determined by the isentropic relations consisting of the area of said sections and the engine compressor starting section called aerodynamic interface plane (AIP). The calculations of the capture and the throat area depend on the airframe and the engine selection and will be explained in the design study.

### 2.1.2 1<sup>st</sup> Duct Section with Middle Station

1<sup>st</sup> duct section starts with the rounded quadrilateral throat section connected to a double elliptical section called the middle station. Said stations are connected with a centreline which is a 4<sup>th</sup> order polynomial spline. Centreline defines the curvature of the duct and so the path the air follows. Centreline’s start and end points are at the centre of the main stations and the duct is generated by sweeping the station profiles along the centreline while each mid station profile points are constructed according to the main station profile points. The steepness of the centreline is one of the key parameters as it determines the flow separation locations in the high curvature duct and the distribution of flow properties across the stations. Centreline is constructed so that the start and end points have tangency to ensure the smooth continuity of the flow. Sample image of the stations and the 1<sup>st</sup> duct centreline is shown in Figure 2.6.

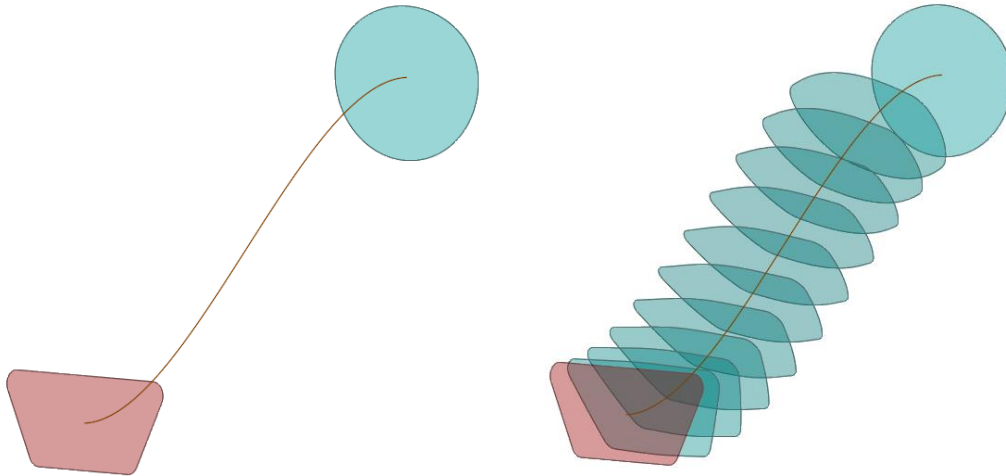


Figure 2.6. 1<sup>st</sup> Duct Centreline and Stations

The parameters defining the centreline are the horizontal and vertical length of the 1<sup>st</sup> duct ( $L_1$  and  $H_1$ ) and the saddle point ( $k_1$ ) of the 4<sup>th</sup> order polynomial which decides the steepness. Centrelines lie on the X-Y plane and the starting point is at the origin of the model (0, 0), the ending point of the 1<sup>st</sup> duct is at the middle station ( $L_1, H_1$ ). Sample image representing  $L_1$  and  $H_1$  parameters is shown in Figure 2.7.

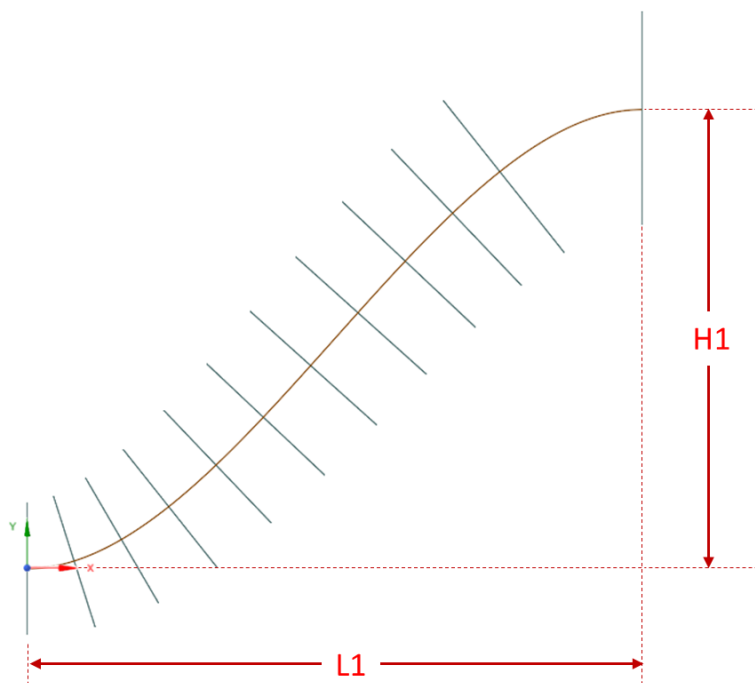


Figure 2.7. 1<sup>st</sup> Duct Dimensional Parameters

The shape of the S-curve is decided by the 4<sup>th</sup> order polynomial which is shown in Equation 2.1.

$$y = ax^4 + bx^3 + cx^2 + dx + e \quad (2.1)$$

The parameterization of the S-curve driven by the polynomial shown is done with the method used by [32]. With this method along with the start-end points, the shape of the spline is driven by a point called the saddle point. The saddle point ratio (k) represents a point where the double derivative of the polynomial changes from positive to negative. It is defined as a percentage of the horizontal length of the spline in the x-axis. Several boundary conditions (B.C.) specified for the parameterization problem is listed in Table 2.1.

Table 2.1. 1<sup>st</sup> Duct Centreline Boundary Conditions

<b>B.C. Name</b>	<b>B.C. Definition</b>
Start point B.C.	$x = 0, \quad y = 0$
End point B.C.	$x = L1, \quad y = H1$
Start point tangency B.C.	$x = 0, \quad y' = 0$
End point tangency B.C.	$x = L1, \quad y' = 0$
Any point along the line (in terms of percentage of L1, here k1 is the saddle point)	$x = k1 * L1, \quad y'' = 0$

The steps of parameterization of the first duct using the boundary conditions is listed below.

- Inserting start point B.C. to the 4<sup>th</sup> order polynomial:

$$e = 0 \quad (2.2)$$

- Inserting start point tangency B.C. to the derived 4<sup>th</sup> order polynomial:

$$d = 0 \quad (2.3)$$

- Inserting end point B.C. to the 4<sup>th</sup> order polynomial:

$$aL1^4 + bL1^3 + cL1^2 = H1 \quad (2.4)$$

- Inserting end point tangency B.C. to the derived 4<sup>th</sup> order polynomial:

$$4aL1^3 + 3bL1^2 + 2cL1 = 0 \quad (2.5)$$

- Inserting any point along the line B.C. to the double derived 4<sup>th</sup> order polynomial:

$$12ak1^2L1^2 + 6bk1L1 + 2c = 0 \quad (2.6)$$

- In order to obtain the 3 coefficients of the polynomial (a, b, c), 3 equations are solved and rearranged to acquire the coefficients in terms of k1:

$$a = \frac{12k1H1 - 6H1}{12k1^2L1^4 - 12k1L1^4 + 2L1^4} = f(k1) \quad (2.7)$$

$$b = -\frac{2H1}{L1^3} - 2aL1 = f(k1) \quad (2.8)$$

$$c = \frac{3H1}{L1^2} + aL1^2 = f(k1) \quad (2.9)$$

- The shape of the 1<sup>st</sup> centreline now can be defined by a single coefficient “k1”, since all coefficients of the 4<sup>th</sup> order polynomial are in terms of saddle point ratio (k1) and the length/height of the end point.

Now that the 1<sup>st</sup> duct centreline is defined and parameterized, the middle station is defined. The middle station consists of two elliptical profiles as upper and lower section connected at the x-axis. An ordinary ellipse has a semi-major and semi-minor lengths defining the ellipticity and has a feature of tangency at the outer points of x

and y axes. The tangency feature is used to connect the two elliptical profiles. Sample image representing the middle station is shown in Figure 2.8.

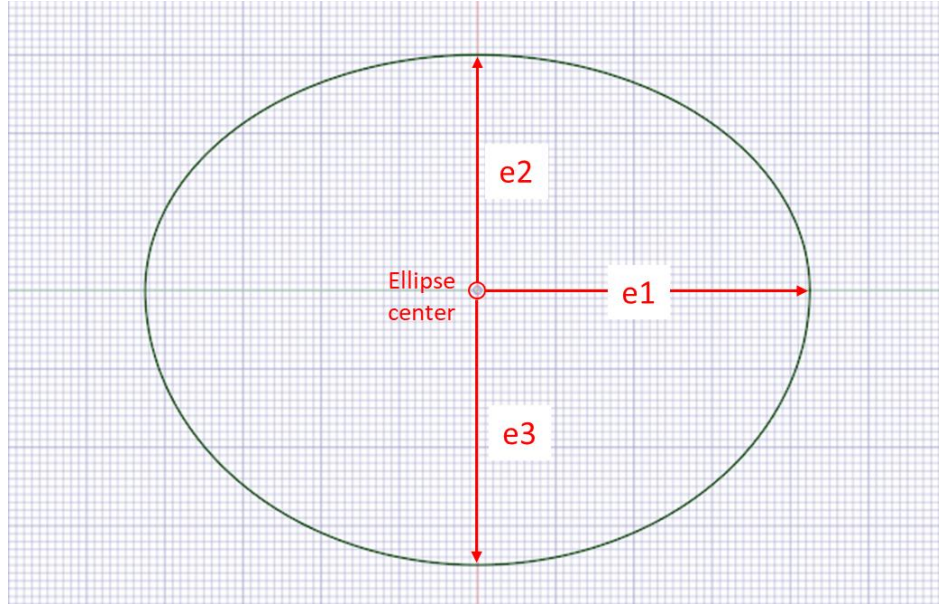


Figure 2.8. Middle Station Profile and Parameters

Upper and lower ellipses share the same semi-major lengths “e1” with the upper and lower semi-minor lengths are “e2” and “e3” respectively. The profile is constructed by trimming upper and lower ellipses at tangency locations. The formulas used for upper and lower ellipses are shown at Equation 2.10 and Equation 2.11.

$$\frac{x^2}{e1^2} + \frac{y^2}{e2^2} = 1 \quad (2.10)$$

$$\frac{x^2}{e1^2} + \frac{y^2}{e3^2} = 1 \quad (2.11)$$

With the construction of the middle profile, the parameters defining the 1<sup>st</sup> duct and the middle profile are finalized as L1, H1, k1, e1, e2 and e3.

The generation of duct is done with the main stations and the mid station profiles which are swept using the centreline constructed. Mid station profiles are constructed according to the throat station and middle station profiles by using the points used to

generate the main stations. The method of constructing the mid stations is explained in steps below:

- Main station profiles are scanned radially from the centre each profile and a set of point coordinates are obtained with their radial locations.
- A mid station location is set at a ratio of duct length and a sketch plane is created using the normal of centreline at the set ratio of duct.
- Points are placed at the sketch plane using the difference of main station points at all radial locations. The transition of points is done considering the mid station location, meaning the points of stations closer to the throat station will be closer to the throat station profile points. Sample image of stations closer to the main stations are provided in Figure 2.9.



Figure 2.9. Stations Closer to Lip and Middle Stations

- With the mid station profiles created, duct is generated by sweeping profiles of all of the stations along the centreline.

With the method of generating mid station profiles, the profiles are placed on the S-line normal to the curvature and the area of the profiles change linearly from the throat to the middle main stations.

### 2.1.3 2<sup>nd</sup> Duct Section with AIP Station

2<sup>nd</sup> duct section starts with the middle station connected to a circular section called the AIP station where the aerodynamic performance coefficients are calculated. The

main stations are connected with a second 4<sup>th</sup> order polynomial centreline. Sample image of the stations and both duct sections is shown in Figure 2.10.

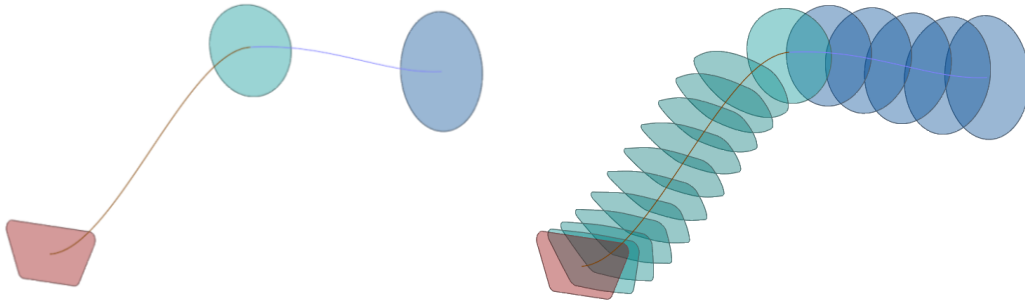


Figure 2.10. 1<sup>st</sup> and 2<sup>nd</sup> Duct Centrelines and Stations

The parameters defining the second centreline are similar to the first one, being the length, height and saddle point. The length and height parameters are defined in the global X-Y plane coordinates. 2<sup>nd</sup> duct starting point is at the middle station (L1,H1) and the ending point at the AIP station (L2,H2). Sample image representing L2 and H2 parameters is shown in Figure 2.11.

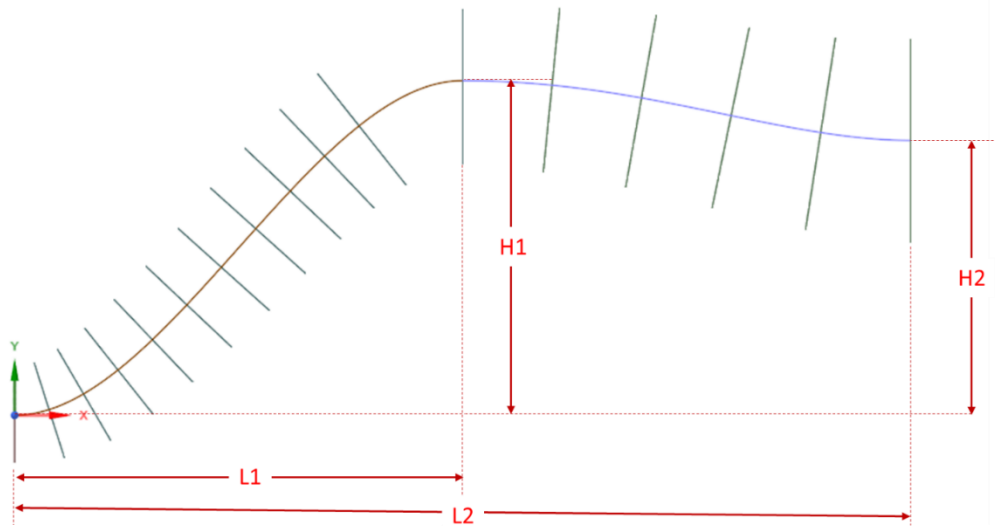


Figure 2.11. 2<sup>nd</sup> Duct Dimensional Parameters

The 2<sup>nd</sup> duct centreline is a 4<sup>th</sup> order polynomial and parameterization of it is done in the same approach taken with the 1<sup>st</sup> duct centreline. Boundary conditions specified for the parameterization of 2<sup>nd</sup> duct centreline is listed in Table 2.2.

Table 2.2. 2<sup>nd</sup> Duct Centreline Boundary Conditions

B.C. Name	B.C. Definition
Start point B.C.	$x = L1 , \quad y = H1$
End point B.C.	$x = L2 , \quad y = H2$
Start point tangency B.C	$x = L1 , \quad y' = 0$
End point tangency B.C.	$x = L2 , \quad y' = 0$
Any point along the line (in terms of percentage of (L2-L1), where k2 is the saddle point)	$x = k2 * (L2 - L1), \quad y'' = 0$

The steps of parameterization of the first duct using the boundary conditions is listed below.

- Inserting start point B.C. to the 4<sup>th</sup> order polynomial:

$$aL1^4 + bL1^3 + cL1^2 + dL1 + e = H1 \quad (2.12)$$

- Inserting start point tangency B.C. to the derived 4<sup>th</sup> order polynomial:

$$4aL1^3 + 3bL1^2 + 2cL1 + d = 0 \quad (2.13)$$

- Inserting end point B.C. to the 4<sup>th</sup> order polynomial:

$$aL2^4 + bL2^3 + cL2^2 + dL2 + e = H2 \quad (2.14)$$

- Inserting end point tangency B.C. to the derived 4<sup>th</sup> order polynomial:

$$4aL2^3 + 3bL2^2 + 2cL2 + d = 0 \quad (2.15)$$

- Inserting any point along the line B.C. to the double derived 4<sup>th</sup> order polynomial:

$$12ak2^2(L2 - L1)^2 + 6bk2(L2 - L1) + 2c = 0 \quad (2.16)$$

- After inserting boundary conditions into the 4<sup>th</sup> order polynomial, following steps are followed to obtain the coefficients:

- Multiplying L1 with Equation 2.13 , then subtracting Equation 2.12 following is obtained:

$$3aL1^4 + 2bL1^3 + cL1^2 - e = -H1 \quad (2.17)$$

- Multiplying L2 with Equation 2.15 , then subtracting Equation 2.14 following is obtained:

$$3aL2^4 + 2bL2^3 + cL2^2 - e = -H2 \quad (2.18)$$

- Combining Equation 2.17 and 2.18 following is obtained:

$$3a(L2^4 - L1^4) + 2b(L2^3 - L1^3) + c(L2^2 - L1^2) = H1 - H2 \quad (2.19)$$

- Combining Equation 2.13 and Equation 2.15 following is obtained:

$$4a(L2^3 - L1^3) + 3b(L2^2 - L1^2) + 2c(L2 - L1) = 0 \quad (2.20)$$

- Multiplying with (L2+L1) following is obtained:

$$4a(L2^3 - L1^3)(L2 + L1) + 3b(L2^2 - L1^2)(L2 + L1) + 2c(L2^2 - L1^2) = 0 \quad (2.21)$$

- Subtracting Equation 2.19 multiplied by 2 from Equation 2.21, coefficient “b” is defined in terms of coefficient “a”:

$$b = \frac{2(H2 - H1) - a[4(L2^3 - L1^3)(L2 + L1) - 6(L2^4 - L1^4)]}{(L1 - L2)^3} \quad (2.22)$$

- Inserting coefficient “b” obtained at Equation 2.22 into Equation 2.20, coefficient “c” is defined in terms of “a”:

$$c = -2a(L2^2 + L2L1 + L1^2) - \frac{3b(L2 + L1)}{2} \quad (2.23)$$

- Inserting coefficient “b” and “c” into Equation 2.13, coefficient “d” is defined in terms of “a”:

$$d = -4aL1^3 - 3bL1^2 - 2cL1 \quad (2.24)$$

- Inserting coefficient “b”, “c” and “d” into Equation 2.12, coefficient “e” is defined in terms of “a”:

$$e = H1 - aL1^4 - bL1^3 - cL1^2 - dL1 \quad (2.25)$$

- Inserting “b” and “c” which are defined in terms of “a” into Equation 2.16, “a” is defined in terms of saddle point ratio (k2):

$$a = \frac{(H2 - H1)[6(L2 + L1) - 12k2(L2 - L1)]}{[4(L2^3 - L1^3)(L2 + L1) - 6(L2^4 - L1^4)][12k2^2(L2 - L1)^2 - 6k2(L2 - L1) - 4(L2^2 + L2L1 + L1^2) + 3(L2 + L1)]} \quad (2.26)$$

- The shape of the 2<sup>nd</sup> centreline now can be defined by a single coefficient “k2”, since all coefficients of the 4<sup>th</sup> order polynomial are in terms of saddle point ratio (k2) and the length/height of the start and end points.

Now that the 2<sup>nd</sup> duct centreline is defined and parameterized, the AIP station is defined. The AIP station is a circular profile which is defined by the diameter of the engine compressor face. The centre of the AIP station is at the (L2, H2) point. The diameter of the AIP station profile is decided by the engine and the centre of the AIP station H2 is decided by the airframe the intake will be installed and the diverter height. With these considerations in mind, L2 and k2 are the parameters that drive the 2<sup>nd</sup> duct geometry.

The generation of the 2<sup>nd</sup> duct is done using the middle and AIP station with the method used for the 1<sup>st</sup> duct section.

## 2.2 Design with Response Surface Methodology

The design and optimization of studies with multiple parameters and objectives creates a challenging problem. The extent of this problem changes with the nature of the problem and the count of parameter and objectives. The parameter count of 8 is defined in 2.1 as the parameters of the parametric model and shown in Table 2.3.

Table 2.3. Parameters of the Study

Parameter	Explanations
K1	The saddle of the first 4 <sup>th</sup> order spline
K2	The saddle of the second 4 <sup>th</sup> order spline
L1	X-distance from the throat to the middle station
L2	X-distance from the throat to the AIP station
H1	Y-distance of the middle station
H2 (fixed)	Y-distance of the AIP station
e1	1 <sup>st</sup> Ellipticity parameter of the middle section
e2	2 <sup>nd</sup> Ellipticity parameter of the middle section

With the parameter and the objective count in mind, a conventional method of optimization based design may result in a long time considering the computationally costly CFD and RCS analyses. Also if the nature of the problem (the reaction of the responses to the parameters) is not known or cannot be foreseen, a conventional

method may lead to a non-converged result or give not the user a chance to search for an alternative design in a reasonable time.

An example of surfaces created by two functions with two parameters is visualized in Figure 2.12. The Figure 2.12 (a) shows a function with a “simple maximum” featuring a single peak point while the Figure 2.12 (b) shows a more complex “saddle point” featuring two maximums. For these relatively simple surfaces that do not possess multiple local peak or low points, a DOE study can be done with small number of experiments/designs and an optimization method like “Steepest Ascent” can be used. But the problems with multiple parameters and responses may result in complex quadratic surfaces that a special set of methods can be used for the design.

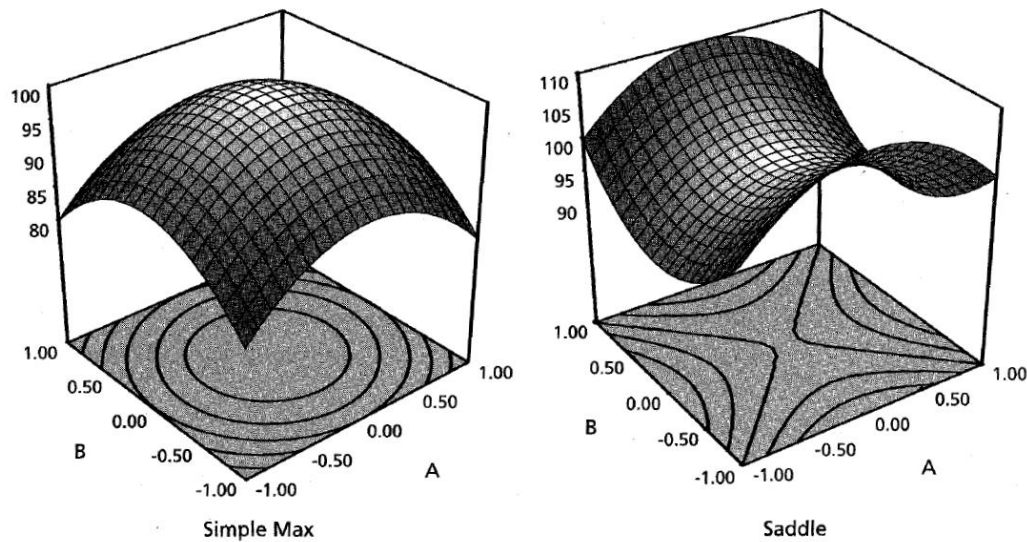


Figure 2.12. Response Surfaces. (a) Simple Maximum; (b) Saddle, [30]

With the count of the parameters and the unknown nature of the problem, the design study is planned to be made with a Surrogate-based Analysis and Design (SBAO) approach, which is also called the Response Surface Method (RSM). The RSM approach is simply the modelling of a response affected by several variables, fitting a surface to the response and using the fit surface design for investigation or optimization [33]. The RSM procedure is explained in the list below:

- A DOE study is carried out with a set of design points selected considering the expected effect of variables on responses,
- Required analyses/experiments are done at the DOE design points,
- A fit model method is selected and the data is fit using the DOE design points,
- The validity of the fit model is investigated through several indicative coefficients,
- The fit model is used with an optimization tool to obtain the best result and the result is validated through analyses.

The flowchart of the RSM procedure followed on the study is shown in Figure 2.13.

The methods of studies are in the sections below.

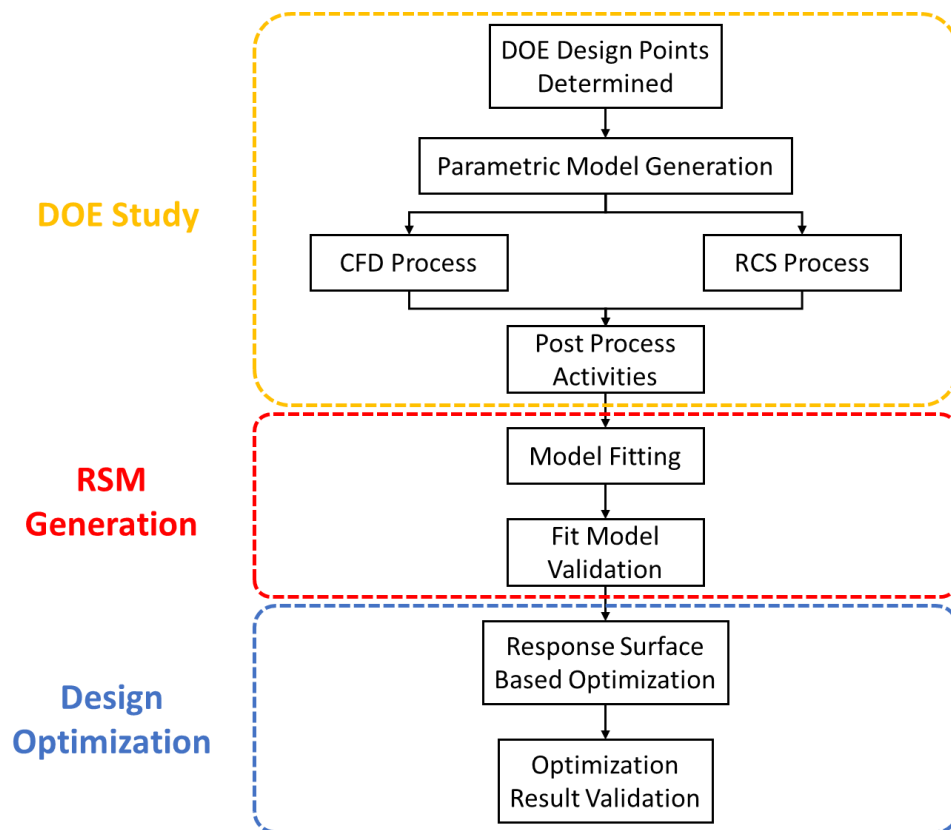


Figure 2.13. SBAO Method Schematic

### 2.2.1 DOE Study Method

The explained RSM procedure starts with the selection of design points that are driven by the variables (factors), but for the design purpose of the thesis, the effect of the parameters of the intake model (factors) on the aerodynamics and radar cross section performance is unknown. At this point, it is a recommended practice to carry out a “Screening” study. Screening designs are used to identify the factors that have the greatest effect on the responses [34]. Achieving the identification of variables with few designs makes screening designs preferable.

In this study “Definitive Screening Design” (DSD) [34], a variant of standard screening design, is carried out. In DSDs, factors are defined as continuous values at three levels (low, medium, high) to track the nonlinear effects on responses. Unlike standard screening designs, confounding of factors up to second order is avoided, so along with the main effects, two-factor interaction effects are also obtained without confounding with each other. With DSDs main effects are orthogonal (uncorrelated) to two-factor interactions and quadratic effects are orthogonal to main effects.

For the DSD and DOE study, a commercial data analysis software JMP 12 is used which has large set of DOE generation, analysis and post-process tools. For the DSD study, 8 variables ( $n$ ) requires 17 design points ( $2n+1$ ) for the identification of these variables.

After the DSD, the variables to be included in the rest of the design study are fixed. For the DOE study, several sampling methods like factorial, fractional factorial and space-filling designs are considered. Factorial designs (e.g.  $2^k$  factorial design) are eliminated due to number of runs required ( $2^k$  runs for  $k$  factors) and the aim of a design approach with low number of runs. Fractional factorial designs are eliminated due to the lack of effective quadratic effect estimation [34]. The space-filling designs like Latin Hypercube Sampling (LHS) are useful for problems needing samples placed on all portions of the design space. The feature of changing uniformity of the sample sets and the correlation among the sample data makes the space-filling

designs unsuitable for response surface approach [16]. Other than the mentioned non-response surface design approaches, methods like central composite design (CCD) and Box-Behnken designs are available. These methods follow the approach of centre point placement with a fractional factorial design for the factors of design space. For the sake of lowering the count of sample points, JMP's custom design generation tool which allows the user to set the model effects properties is used. The custom design is set with the factors again defined as continuous values at three levels. Considering the expectation of interactions of factors and quadratic relations, the custom design is set with the properties listed below:

- Main effects are included for all factors including the polynomial terms of each factor. ( $L1$ ,  $L1^2$ , etc.)
- Interaction effects are included up to 2<sup>nd</sup> order for all factors.
- Quadratic terms are included up to 2<sup>nd</sup> order for all factors.

The DOE design points are generated using custom design generation tool and the automated CFD and RCS processes are carried out with the parametric model generator. The output of the processes are used to RSM fitting and generation.

For both the DSD and DOE designs, the effect of parameters on the responses are analysed using the p-value approach. It is stated in [33] that "The P-value is the probability that the test statistic will take on a value that is at least as extreme as the observed value of the statistic when the null hypothesis  $H_0$  is true.". Simply, the p-value quantifies the statistical significance of a factor that a smaller p-value means higher level of significance. For both studies the p-values of the factors (parameters) are investigated.

### **2.2.2 Surrogate Model Generation Method**

The output of the DOE study is used for the generation of the response surface (surrogate) model. The model is generated using Kriging method which is a parametric surrogate modelling method.

Kriging method is based on global function where the responses are a function of all variables. Kriging method is an exact interpolator, meaning that the function output at the supplied DOE design points are the exact outputs of the said design points [35]. At the unsampled locations, the output estimation calculation is done with a combination of a linear and variation (small and large scale) models [16]. The variation model estimates the fluctuation around the trend modelled by the linear part and the said fluctuations are calculated considering the distance between the locations.

In this study, HEEDS MDO, a modelling and simulation software is used for the generation of RSM. HEEDS MDO features a RSM generation tool with several modelling options and model validation capabilities. As was mentioned, DOE design points and obtained outputs are supplied to the tool for the generation of the Kriging surrogate model. The smoothness and the shape of the response surface is affected by the fitting of the functions. For the Kriging modelling, Gaussian surface approximation is used with the automatic shape factor adjustment done by the HEEDS MDO.

After the generation of the model, validation of the model is done by examining the actual and predicted model outputs at the supplied design points and the cross-validation results. Using a Kriging modelling method, the difference between the actual and predicted results are expected to be nearly exact, so the cross-validation results will be the indicative values for the performance of the model. In HEEDS MDO, cross-validation is handled with a leave-one-out approach where the surrogate model is generated by leaving the supplied design points one by one and calculating the maximum residual between the predicted and actual outputs at a left out point.

### **2.2.3 Design Optimization Method**

The design optimization is carried out with the HEEDS MDO using the RSM generated. The surrogate model actually consists of three models for the three

performance outputs, so the problem becomes a multi objective parameter optimization. HEEDS MDO features a hybrid-adaptive optimization algorithm called SHERPA which employs multiple search algorithms with adaptation capability according to the optimization problem [36].

The SHERPA algorithm is used for the optimization with the variables defined by the parametric model and with the objectives defined by the CFD and RCS performance coefficients. Since the optimization tool is based on the RSM, the performance of a design is obtained instantaneously. This provides the user flexibility on the resolution of the variables (the count of values that a parameter can take in a bounded space) and the maximum number of evaluations. For the study, following properties are decided to be used:

- The resolution of each variable is set to 101 meaning that each variable can take a value in the bounded space divided by 100.
- The optimization algorithm decides the values that the variables take and the performance of a design is calculated as a “weighted sum of all objectives” approach. This approach takes all objectives into consideration for the calculation of the design performance. The weight of the objectives which are the PR, DC and RCS, are set equally and normalized with the baseline design for all designs. The performance calculation is given in the Equation 2.27.

$$Performance_{design} = 0.3\bar{3} \frac{PR}{PR_{baseline}} + 0.3\bar{3} \frac{DC60}{DC60_{baseline}} + 0.3\bar{3} \frac{RCS}{RCS_{baseline}} \quad (2.27)$$

- The optimization is set to maximize the PR and minimize the DC60 and RCS performance coefficients.
- A constraint limit is assigned for the DC60 at a value of 0.6 so that the designs with a higher value gets penalized with the performance ratings. With this approach, the designs that are limited by the constraint are pre-eliminated through optimization.

- The number of evaluations is set to a random evaluation number of 4000. The convergence of the optimization is checked through the performance value. If the convergence is not ensured for the set evaluation number, additional evaluations can be done.

With the conclusion of the optimization, the validation of the highest performing design is done by performing with the CFD and RCS analyses. The results are compared in terms of percentile difference from the analyses results.

## **2.3 CFD Overview**

The CFD processes applied are to obtain the aerodynamic performance coefficients of the parametric intake models. CFD processes are summarized in the list below and explained in sections.

- Pre-process section includes the steps for the preparation of the intake model for the CFD analysis.
- CFD analysis section includes the tools and method of carrying out CFD analysis of the fluid dynamics problem.
- Post-process section includes the method of obtaining aerodynamic performance coefficients and post-process images.

### **2.3.1 Pre-Process Overview**

In the pre-process activities, parameterized intake model is prepared for the CFD analysis by implementing a volume mesh representing the flow field. The external flow field is constructed as a rectangular prism using the end of the outer lip of the pitot type intake. The internal flow inside the duct is terminated at a surface which is created by extending the AIP station of the duct along the axis with the implementation of a fixed engine hub geometry. The extension of the AIP station is done to improve the convergence of the solution so the flow is straightened at the

boundary. Half of the flow field is modelled in order to reduce the size of the mesh. Sample flow field with the external and extended internal section is shown in Figure 2.14.

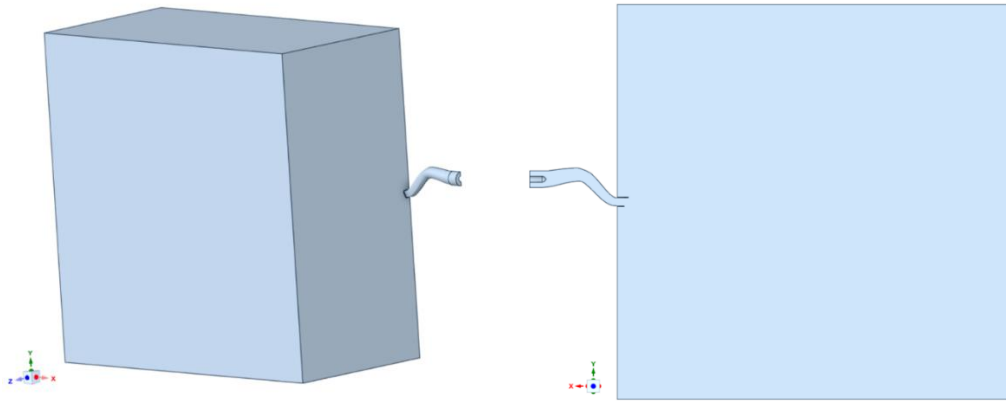


Figure 2.14. CFD Flow Field Samples

In the meshing process, Ansys Fluent Meshing meshing tool is used for both the validation studies and design studies. For the surface mesh, triangular face elements are used on all surfaces. For the volume mesh, triangular prisms are used for the boundary layers on the wall surfaces and tetrahedrals are used for the flow field volume meshes. In the flow field, the duct, lip and hub surfaces are wall surfaces which the boundary layers are grown.

Properties of the boundary layers grown on the walls are adjusted according to the flow regime and turbulence modelling method to be used. The first layer height is determined with the turbulence modelling method driven  $y^+$  number which ensures the flow is resolved in the viscous sublayer imposed by the Law of the Wall [37]. The number of the boundary layers is driven by the total boundary layer thickness height. Sample images of the flow field meshes are shown in Figure 2.15.

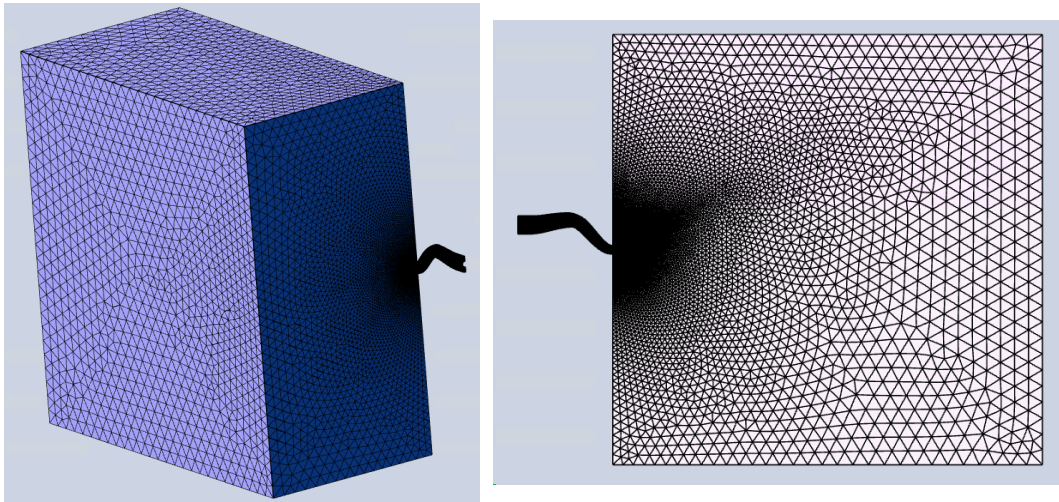


Figure 2.15. Sample Flow Field Meshes

For the surface and volume mesh sizes, the sizes decided on the validation cases' mesh convergence studies are used. Local refinement regions are applied in the duct area with special refinements for the lip and hub surfaces. With the refinements mentioned, the mesh is intended to be denser at the throat and AIP stations. A sample mesh inside the duct with the refinement regions and the boundary layers is shown in Figure 2.16.

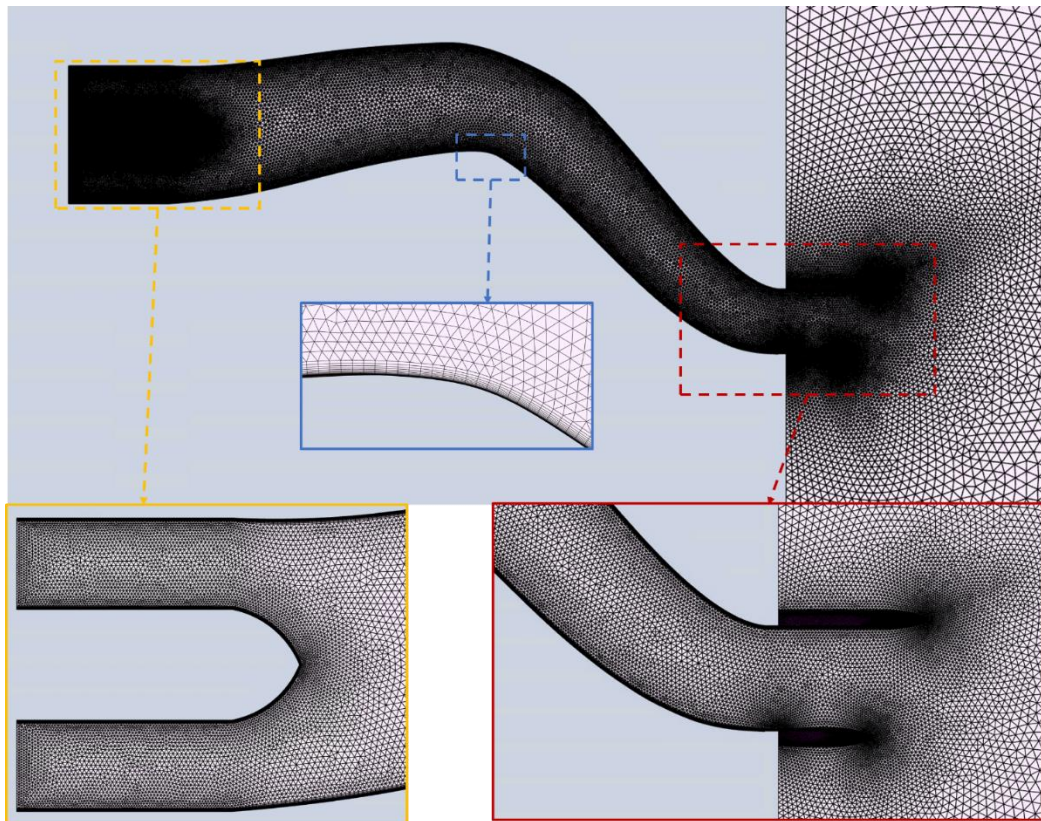


Figure 2.16. Sample Mesh with Refinement Regions

The activities shown in this section are automatized using the named selections assigned on the surfaces. Flow field is constructed with the parameterized intake model and the mesh is generated according to the named selections (lip surface, hub surface, etc.) making the process independent of the model used.

### 2.3.2 CFD Analysis Overview

In the CFD analysis activities, ANSYS Fluent CFD tool is used. ANSYS Fluent is a commercial CFD solver which is capable of solving Navier-Stokes equations for the compressible flow in three dimensional space with unstructured mesh. The governing equations, the turbulence treatment and the analysis approach are investigated in the sections below.

### 2.3.2.1 CFD - Governing Equations

In all of the CFD analysis activities, Reynolds Averaged Navier-Stokes (RANS) equations are used with several turbulence modelling methods investigated. The equations make use of conservation equations listed below:

- Conservation of mass:

$$\frac{\partial}{\partial t} \int_{\Omega} \rho d\Omega + \oint_{\partial\Omega} \rho (\vec{v} \cdot \vec{n}) dS = 0 \quad (2.28)$$

- Conservation of momentum:

$$\frac{\partial}{\partial t} \int_{\Omega} \rho \vec{v} d\Omega + \oint_{\partial\Omega} \rho \vec{v} (\vec{v} \cdot \vec{n}) dS = \int_{\Omega} \rho \vec{f}_e d\Omega - \oint_{\partial\Omega} \rho \vec{n} dS + \oint_{\partial\Omega} (\bar{\tau} \cdot \vec{n}) dS \quad (2.29)$$

- Where  $f_e$  is an external body force and  $\bar{\tau}$  is the stress tensor

- Conservation of energy:

$$\begin{aligned} \frac{\partial}{\partial t} \int_{\Omega} \rho E d\Omega + \oint_{\partial\Omega} (\rho E + P) (\vec{v} \cdot \vec{n}) dS \\ = \int_{\Omega} (\rho \vec{f}_e \cdot \vec{v} + \dot{q}_h) d\Omega + \oint_{\partial\Omega} \kappa (\nabla T \cdot \vec{n}) dS + \oint_{\partial\Omega} (\bar{\tau} \cdot \vec{v}) \cdot \vec{n} dS \end{aligned} \quad (2.30)$$

- Where  $E$  is the total energy,  $P$  is the pressure,  $\dot{q}$  is the heat transfer rate,  $T$  is the temperature.

The stress tensor,  $\bar{\tau}$ , is defined as:

$$\bar{\tau} = \mu \left[ (\nabla \vec{v} + \nabla \vec{v}^T) - \frac{2}{3} \nabla \cdot \vec{v} I \right] \quad (2.31)$$

Where  $\mu$  is the molecular viscosity and  $I$  is the unit tensor.

The RANS equations make up 5 equations for the density, velocity (for three components) and energy unknowns. For the unknowns of pressure and temperature, ideal gas relation given in Equation 2.32 is used.

$$P = \rho RT \quad (2.32)$$

For the viscosity of fluid used in the stress tensor, Sutherland's law is used which is an approximation formula defining the change of viscosity with temperature.

$$\mu = \frac{1.458 T^{3/2}}{T + 110.4} 10^{-6} \quad (2.33)$$

Much of the present industrial turbulent CFD analysis applications are done with the Reynolds Averaged (time averaged) Navier-Stokes (RANS) equations. The other methods of solving turbulent flows through Navier-Stokes equations are direct numerical simulation (DNS) and large eddy simulation (LES) and both of them offers much more computationally expensive solutions comparing to the RANS method for the industrial applications [38].

In Reynolds averaging, the solution variables (scalars and vectors) are decomposed into time averages and fluctuations about the average:

$$\varphi = \bar{\varphi} + \varphi' \quad (2.34)$$

Substituting the decomposed version of variables creates additional terms of stress gradients and heat flux quantities associated with the turbulence of the flow. These terms are handled through a selection turbulence modelling methods which are summarized in the following sections.

### 2.3.2.2 Turbulence Modelling Methods

The modelling of the stresses for the RANS approach is done with methods utilizing the Boussinesq hypothesis. With the methods, the computation of turbulent viscosity is carried out with transport equations representing the turbulent variables as turbulent kinetic energy and dissipation coefficients. The methods using this approach and investigated are Spalart-Allmaras model which uses one transport

equation and Realizable  $k-\varepsilon$  and  $k-\omega$ -sst models which use two transport equations. The application and the characteristics of these methods which are available in ANSYS Fluent are summarized in the list below:

- Spalart-Allmaras (SA) model, is a one equation model that solves the turbulent viscosity as the transport equation. Originally created for aerospace applications, SA model is designed to approximate turbulent viscosity for wall-bounded flows; however the model tend to produce errors for separated flows and do not offer other improvements over the simpler algebraic models [38]. Even though separated flow regions are expected for the intake design application, the performance of this model at predicting the aerodynamic performance coefficients is studied with validation cases in the validation sections.
- Realizable  $k-\varepsilon$  model is a two equation model that solves the turbulent kinetic energy and turbulence dissipation rate as the transport equations. Realizable  $k-\varepsilon$  model is an improved version of the standard  $k-\varepsilon$  model which is a popular model used for the industrial and practical flow problems due to its accuracy and cost for a wide range of turbulent applications. The standard  $k-\varepsilon$  model assumes the flow is fully turbulent as it does not include the damping effect of turbulence in the viscous sublayer, while the Realizable variant uses a modified version of the equation for the dissipation rate, which makes this variant more logical in calculating the Reynolds stresses. The features mentioned makes this model applicable to cases with steep flow curvatures and vortices within reasonable accuracy. Considering the usage of this model, the performance of it is studied with the validation cases.
- $k-\omega$ -SST model is a two equation model that solves the turbulent kinetic energy and the specific dissipation rate as the transport equations.  $k-\omega$ -SST is an improved version of standard  $k-\omega$  model. The standard model offers advantage over the  $k-\varepsilon$  models at predicting the boundary layer flows and separation but suffers at prediction of the flow outside the shear layer. SST (Shear Stress Transport) improvement allows the model to avoid freestream

sensitivity by using the  $\omega$  and  $\varepsilon$  equations. The  $k$ - $\omega$ -SST model may predict the flow separation better than the Realizable  $k$ - $\varepsilon$  model due to its performance at predicting the boundary layer flow, but may lack ease of convergence. The model and the mentioned comparisons will be studied with the validation cases.

### 2.3.2.3 CFD Analysis Approach

The analyses for the validation and design studies are carried out using the steady density based solver with Green Gauss Node Based gradient discretization. Second-order upwind scheme is used for the flow and turbulence related coefficients. The solution is initialized by the pressure far field or the inlet conditions. Solution convergence control is done by adjusting the CFL number through iterations. The convergence check is done with checking the aerodynamic performance coefficients (PR and DC60) and the mass flow rate required by the specified engine. The convergence check scheme is visualized in Figure 2.17.

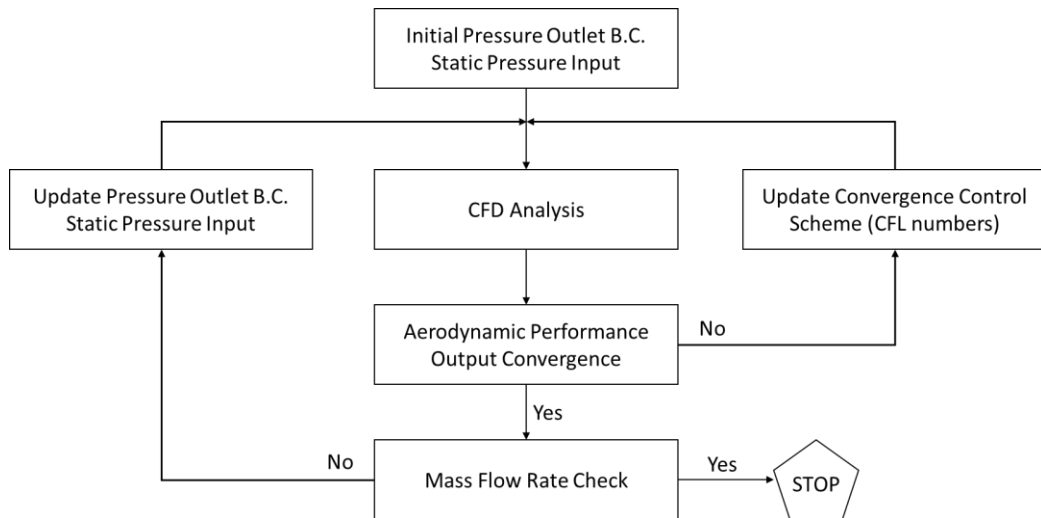


Figure 2.17. CFD Analysis Approach Schematic

The convergence check procedure is done firstly by the initial value of the pressure outlet static pressure guess. With the analysis carried out, the aerodynamic performance output convergence check is achieved when the difference of the

coefficients of the last iteration are less than 1% of the average of last 200 iterations. If the convergence of the mass flow rate is not achieved, the static pressure is updated and the process continues until the convergence check of both processes are achieved and the post-process activities can start.

### **2.3.3 CFD Post-Process Overview**

In the post-process activities, the aerodynamic performance outputs are calculated and used for the DOE studies. The two outputs are explained in details in the sections below.

#### **2.3.3.1 Pressure Recovery (PR)**

The pressure recovery (PR) is the ratio of average total pressure at the AIP to the freestream total pressure. The PR simply shows the quality air that is delivered to the engine through the intake. In aerodynamic aspect, the primary role of the intake is to deliver air to engine with the highest total pressure recovery [5].

In the post-process activities, the mass-weighted averaged total pressure is used at the AIP for the PR calculation.

$$PR = \frac{P_{T \text{ AIP}}}{P_{T \infty}} \quad (2.35)$$

#### **2.3.3.2 Distortion Coefficient (DC)**

Distortion of the flow at the compressor is an undesirable incident as it may lead to compressor stall or engine surge making the engine inoperable. A distortion may cause a part of the flow at AIP has a pressure higher than the other segments causing an effect on the compressor map. DC60 is a usually employed coefficient used for the calculation of distortion [4]. The method of calculation DC60 consists of dividing the AIP into 60° sectors and calculating the difference between the most distorted

sector total pressure wise and the average total pressure of the all sectors. A visualization of the sectors mentioned is shown in Figure 2.18.

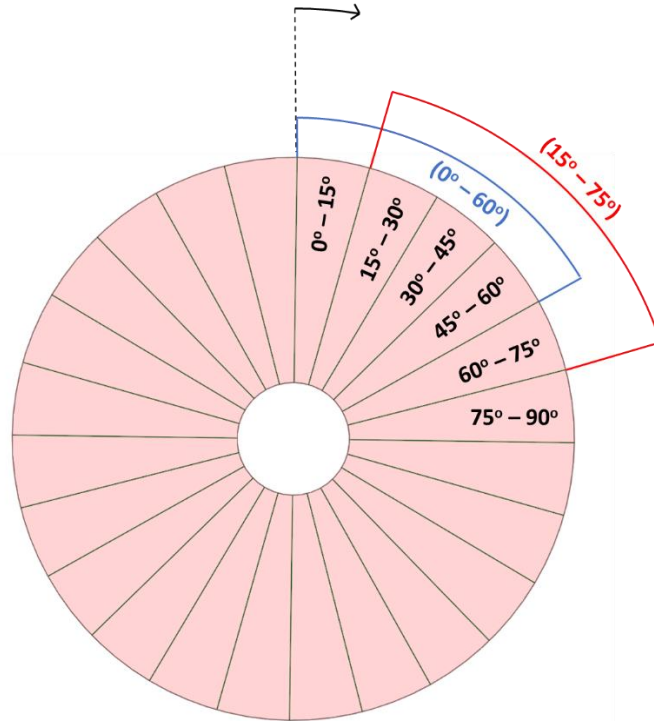


Figure 2.18. DC Sector Definition

To calculate the variables in the said 60° sector, smaller 15° pieces are obtained and the average of the sectors are calculated using the smaller pieces. After obtaining the average total pressure values all of the sectors, the minimum of these sectors is used in the DC60 calculation by subtracting the average of all sectors and dividing by the dynamic head as follows:

$$DC60 = \frac{|P_{T,min} - P_{T,ave}|}{q_{AIP}} \quad (2.36)$$

## 2.4 RCS Overview

The RCS processes applied are to obtain the radar cross section output of the parameterized intake model. RCS overview approach is different from the CFD overview as intake design is not necessarily handled with stealthy approach.

Electromagnetics basics, RCS prediction methods and the applied RCS evaluation method are explained in sections.

### 2.4.1 Electromagnetics Basics

Before the evaluation of RCS characteristics of an object, electromagnetics basics, echo scattering mechanisms and suitable prediction tools should be covered. Electromagnetic scattering is the scattering of a radar wave off an object which is dependent on the properties of the incoming radar wave, the shape of the object and the electromagnetics properties of the object. The amount of related scattering is defined as an area called radar cross section.

Electromagnetic waves are harmonic functions consisting of oscillating electric and magnetic fields which are perpendicular to each other. A schematic of a wave is shown in Figure 2.19.

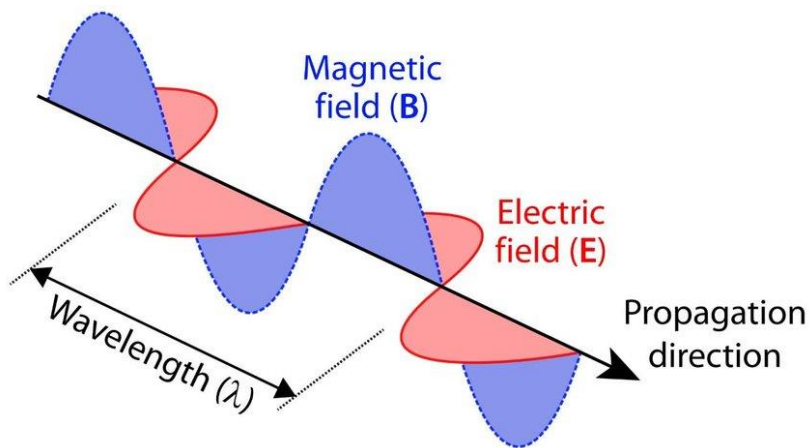


Figure 2.19. Electromagnetic Wave [39]

Electromagnetic waves are characterized by the frequency (or the wavelength) and the polarization of the wave. The polarization of the wave decides the geometric orientation of the said wave's oscillation and it is defined by the local direction of the electric field for linear polarization.

A target's RCS value is defined by the amount of radar wave power reflected back from the effective surface area of the target. The formula of the RCS is shown in Equation 2.37.

$$\sigma = \lim_{R \rightarrow \infty} 4\pi R^2 \frac{|E_s|^2}{|E_0|^2} \quad (2.37)$$

In Equation 2.37, the R is the distance from the target, the E<sub>o</sub> and E<sub>s</sub> are the strengths of the incoming and scattered waves making the RCS having a dimension of area. RCS is defined in terms of m<sup>2</sup> or dBm<sup>2</sup>. Using the decibel scale is preferred to accommodate the values both small and large values.

The RCS value of an object is also dependent on the antenna configuration of the radar system. If the radar transmitter and receiver are on the place, the system is called monostatic and if they are apart the system is called bistatic. A monostatic radar system is considered for the RCS evaluation and a sample schematic of monostatic/bistatic configurations are shown in Figure 2.20.

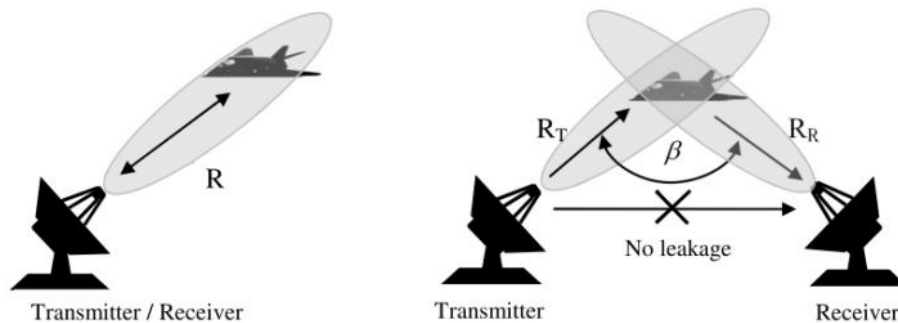


Figure 2.20. Monostatic and Bistatic Radar Configurations [40]

RCS reduction of objects depends on the echo scattering mechanisms present on the objects. A typical airframe's surfaces cause echo scattering mechanisms through several electromagnetic phenomena. These scattering mechanisms are shown on Figure 2.21.

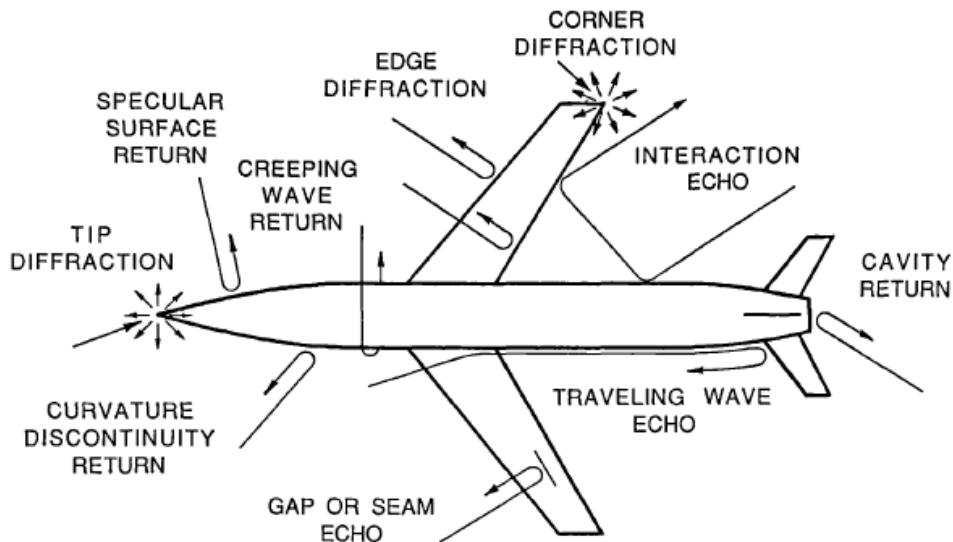


Figure 2.21. Aircraft Echo Scattering Mechanisms [10]

One of the most effective scattering mechanisms is specular/interaction scattering which is caused by waves reflecting back to the source from surfaces either directly or after several bounces on the surfaces. Cavity return is a special kind of this scattering mechanism which is a result of cavities present on the airframe like intakes or exhausts.

The RCS reduction method that is in focus is for the cavity returns and as like other mechanisms three main RCS reduction methods are used.

- Shaping is the first method and it is done by diverting the incoming radar waves to directions other than the possible radar receiver locations. Decreasing the curvature of target surfaces, adjusting the angles between planar surfaces and reduction of surface discontinuities are common practices used for this method. These practises commonly contradict with the aerodynamic shaping practices so these must be applied in line with aerodynamic design processes.
- Using radar absorbing materials (RAM) is the second method and it is done by using RAM materials which are effective at absorbing the radar waves at

the specific wave frequencies. Related materials are either multi-layer composite materials or RAM paints. Mentioned composite materials are hard to apply at specific areas of the airframe and the paints require regular maintenance [41].

- Applying radar cancelling measures is the third method and it is done by placing structural or electromagnetic details as countermeasures for readjusting the radar reflections. Several limitations are present for this method as these countermeasures tend to create secondary scattering mechanisms at some other threat angles, lower the aerodynamic performance or work at specific frequency range.

The study is focusing on the RCS reduction method of shaping as other methods are either in need of additional technologies like RAM and maintenance or complex cancelling details. The reduction is planned to be done by changing the geometrical properties of the intake with the parametric model.

#### **2.4.2 RCS Prediction Methods**

There are several analysis methods for assessing an object's RCS value other than experiments. Related methods are Maxwell equations based exact techniques, approximate techniques and hybrid methods comprising of elements from both techniques. Related methods are summarized in the list below:

Exact techniques include numerical methods of Maxwell equations handled either as differential or integral forms.

“Finite Difference-Time Domain (FD-TD)” [10] method uses differential form of Maxwell equations by transforming these into finite difference equations. The method includes the solution of the electric field in marching time steps and obtaining magnetic field according to the electric field output.

“Method of Moments (MOM)” [10] method uses integral form of Maxwell equations by transforming these into homogeneous linear equations. With this method, the target geometry is modelled with a surface grid and a system of matrix containing homogeneous linear equations is solved to obtain the surface currents on the target surfaces. Related surface currents are used to calculate the reflecting electric field to obtain the RCS output.

Approximate techniques includes surface integrals or ray tracing methods which are applicable in the optic region where the size of the target model is much bigger than the wave length.

“Physical Optics (PO)” [10], a surface integral approximate method, solves the Stratton-Chu integral form of Maxwell equations and the calculations of electric-magnetic fields are done on any point on the surface with tangent surface assumption. This method alone lacks accuracy at highly skew surfaces or surface discontinuities. “Physical Theory of Diffraction (PTD)” is basically an expansion of PO method where the current on the surface edges or discontinuities are added to the total surface current calculation.

“Geometrical Optics (GO)” [10], a ray tracing approximate method, applicable at the optical region where the waves act as rays, uses ray tracing while the wave is propagating and reflecting according to the curvature of the target surfaces. The reflected rays are used to calculate the RCS output. Extensional methods “Geometrical Theory of Diffraction (GTD)” and “Uniform Theory of Diffraction (UTD)” are used to correct the RCS output considering diffractions and the field strengths caused by these diffractions.

“Shooting and Bouncing Rays (SBR)” [42], a ray tracing approximate method, uses a combination of PO and GO methods for calculating RCS output in the optical region. With this method, the calculations of fields of rays propagating according to the GO method are done with PO method to evaluate the RCS output. This method produces quality outputs for complex geometries using two approximate methods considering the fast solution times with respect to exact techniques. As an extension

of SBR, SBR+ method uses PTD and UTD corrections to catch scattering mechanisms caused by surface edges and discontinuities causing diffractions.

The study at hand targets an RCS analysis of a complex intake geometry at high frequencies. Considering the mentioned analysis methods, SBR+ method is chosen as it is applicable at high frequencies, supports multiple reflections, takes diffractions into consideration and is computationally fast. Multiple validation studies for this method will be covered in the validation sections.

### **2.4.3 RCS Evaluation Method**

For the RCS analysis, ANSYS HFSS electromagnetic simulation software is used which has the SBR+ method integrated into it. The SBR+ method requires a target model, analysis frequency set and incident plane waves assigned to propagate onto the target at specific angles. After carrying out the analysis, the tool gives the RCS values in  $\text{dBm}^2$  for each incident plane wave angle specified.

For the study, since the expected output is the RCS contribution of the intake system alone, parametric intake model is prepared by putting the duct into an enclosure. Since the only RCS reduction method considered is shaping, the lip and duct surfaces are assigned as perfect electrical conductor (PEC) material to obtain the nominal outcome with no other precaution applied whatsoever. The enclosure used has Fresnel boundary assigned which has a perfect absorber property. The airframe that the intake is planned to be installed is not included in the analyses for two reasons listed below.

- The intake lip has a vertical angle property preventing the waves bouncing from the airframe into the duct.
- The incident plane wave angles are decided in accordance with the lip vertical angle so the need to include the airframe is eliminated.

Sample electromagnetic analysis ready model with enclosure is shown on Figure 2.22.

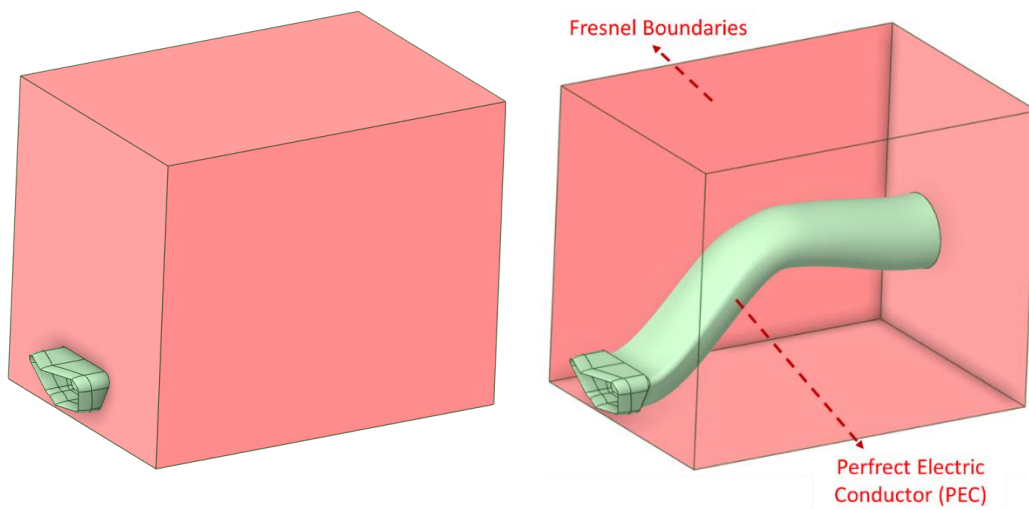


Figure 2.22. RCS Analysis Model

The SBR+ method requires target model to be bigger than the wave length, with this notion in mind, a radar system working at the IEEE standard X-band (8-12 GHz) is assumed. The target model size will be covered in the intake design process section. Since there is not a generalized way of selecting the incident plane wave propagation directions in intake RCS analysis, a new method is defined. Several assumptions are made for the method to be defined and these assumptions are listed below.

- The airframe that the intake is installed on is a cruising aircraft, and it is flying towards a target with a radar system.
- Incident radar waves can approach the airframe according to the place and the orientation of the radar system and the airframe, so the intake may be exposed to radar waves approaching at differentiating angles. This requires a sweep of incident plane wave approach angles.

With these assumptions in mind, an azimuthal sweep of  $60^\circ$  with  $1^\circ$  steps and elevation sweep of  $20^\circ$  with  $5^\circ$  steps is assigned. In electromagnetics reference axis system, this sweep set is defined in a spherical vector definition angles  $(\phi, \theta)$ . In spherical vector notation, mentioned sweep set is set as  $180^\circ$ - $200^\circ$   $\theta$  and  $60^\circ$ - $120^\circ$   $\phi$  angles. The sweep system is visualized as a total sweep zone in Figure 2.23 and as

a  $\theta$  sweep planes in Figure 2.24. Also the number of bounce a wave can do is set to 8.

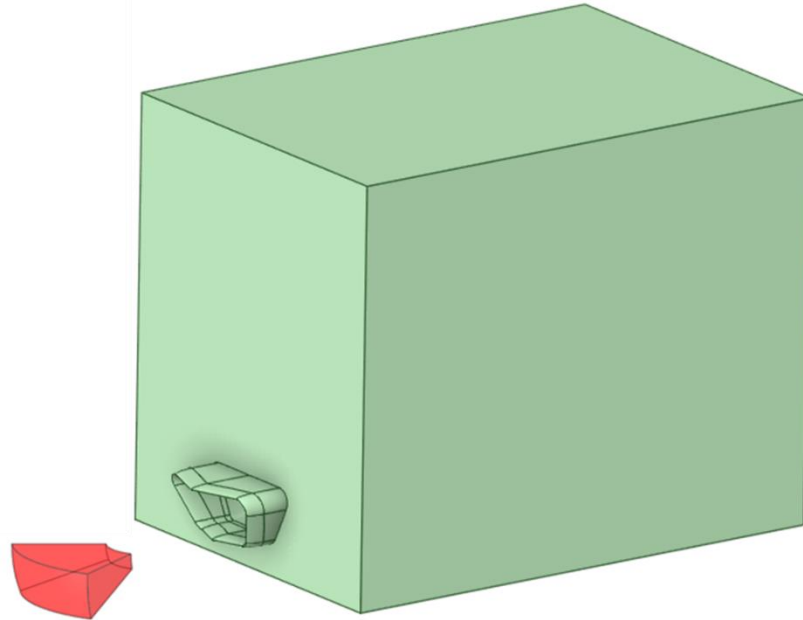


Figure 2.23. RCS Analysis Illumination Outlines

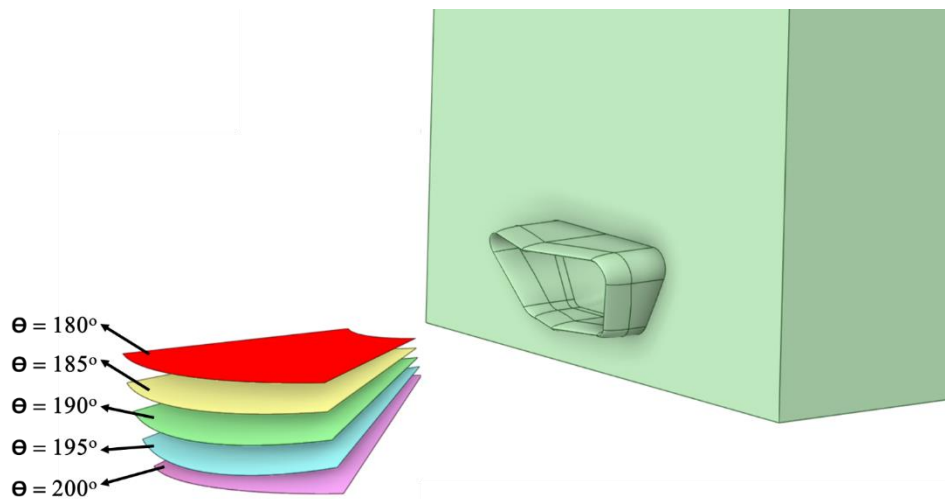


Figure 2.24. RCS Analysis Illumination  $\theta$  Sweeps

With the incident plane wave propagation angles are assigned, a total of 305 RCS values will be obtained per analysis. For the RCS performance output, a single

performance value is generated with the method defined. The method of assessing RCS performance output is summarized in the list below.

The obtained RCS values are modified to assign importance to each plane wave.

- Considering the assumption of the airframe flying towards the radar system, the plane wave defined as  $\phi=180^\circ$  and  $\theta=90^\circ$  should have higher importance, and importance should get lower moving away from this plane wave.
- Assigning the importance for the wave's RCS values is done by multiplying each value with a coefficient created with a Gaussian function. The generalized Gaussian function is given in Equation 2.38.

$$f(x) = a e^{\left(-\frac{(x-b)^2}{2c^2}\right)} \quad (2.38)$$

- In Equation 2.38, “a” defines the peak of curve which changes with  $\phi$  sweep set, “b” defines the center of the peak set as 90 and “c” defines the standard deviation set as 20. The peak of the curve defines the coefficient of each  $\theta$  sweep set as 1.0 for  $\theta=180^\circ$ , 0.9 for  $\theta=185^\circ$ , 0.8 for  $\theta=190^\circ$ , 0.7 for  $\theta=195^\circ$ , 0.6 for  $\theta=200^\circ$ . The defined importance of values changes for both  $\phi$  with Gaussian function and  $\theta$  with changing the peak value.
- The Gaussian functions showing the modifier coefficients for all  $\phi$  sweep sets are shown in Figure 2.25.

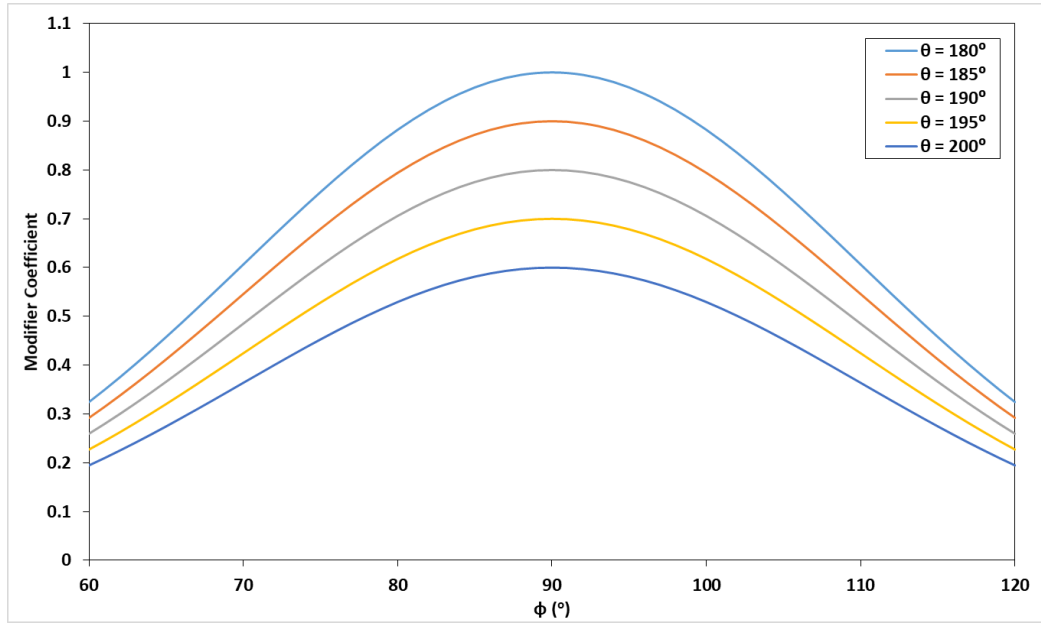


Figure 2.25. Gaussian Modifier for  $\theta$  Angle Sweeps

- The RCS values of all incident plane waves are multiplied with the modifier coefficients and modified RCS values are obtained.

Using the modified RCS values, the maximum ( $RCS_{max}$ ), the minimum ( $RCS_{min}$ ) and the average ( $RCS_{ave}$ ) of all RCS values are calculated. It is expected that the average of different designs will be similar to each other because all designs will share the same intake lip, so the average value will be monitored rather than being used for performance calculation.

Using the modified RCS values, RCS performance output,  $RCS_{mod}$ , is defined as in Equation 2.39.

$$RCS_{mod} = \frac{RCS_{max} + RCS_{min}}{2} \quad (2.39)$$

With the RCS performance output is defined, the method of RCS evaluation is completed and can be used in the intake design process DOE activities after the validation cases.



## CHAPTER 3

### VALIDATION STUDIES

In this chapter, validation cases for CFD and RCS processes are presented. Cases for both processes are selected and investigated for the several reasons listed below.

- Validation of CFD pre-process methods of meshing (local/global mesh sizes, etc.),
- Validation of CFD performance outputs along with the mesh convergence studies,
- Validation of RCS performance outputs.

Validation studies are given in the following sections.

#### 3.1 CFD Validation Studies

Two validation cases are selected for the CFD validation studies. The first one is RAE M2129 intake which is an s-duct intake with a lip geometry operating at low subsonic speed. The second is an S-shaped intake only duct geometry operating at subsonic speed. The cases are investigated in the following sections.

##### 3.1.1 RAE M2129 Intake Test Case

###### 3.1.1.1 Model Details and Test Conditions

RAE M2129 intake is an S-duct intake with a lip geometry designed at the Royal Aircraft Establishment. It is investigated extensively through wind tunnel testing and used for CFD validation purposes. The geometry is modelled according to the

centreline and diameter definitions given in [19]. The key model parameters is given in Table 3.1 and the image of the intake geometry is given in Figure 3.1.

Table 3.1 RAE M2129 Model Dimensions [19]

Parameter	Value [mm]
Capture Area Face Diameter	144.0
Throat Section Diameter	128.8
S-duct Length	457.2
AIP Section Diameter	152.4

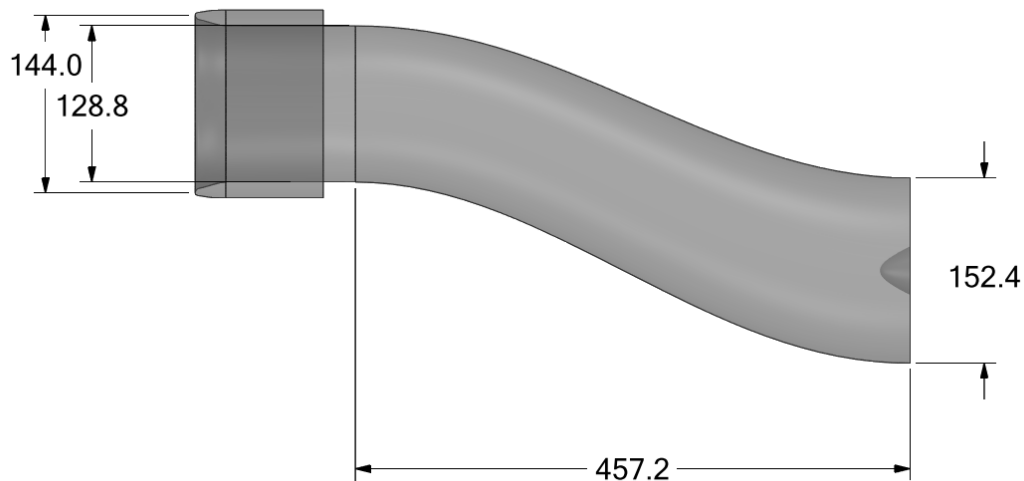


Figure 3.1. RAE M2129 Model (dimensions in mm)

The tests on the given model is done by GARTEUR Aerodynamic Action Group AD/AG-43 “Application of CFD to High Offset Intake Diffusers” consisting of several participating nations. The model of subject features a hub (bullet) geometry with probe rakes attached for the obtainment of the pressure values to acquire aerodynamic performance coefficients. The test is done to obtain the static data at the said rakes at flow conditions given in Table 3.2.

Table 3.2 RAE M2129 Test Conditions [19]

<b>Flow Conditions</b>	
Free Stream Mach	0.204
Free Stream Total Pressure	105139.5 Pa
Free Stream Total Temperature	293.7 K
Angle of Attack	0°
Sideslip Angle	0°
Mass Flow Rate	1.9382 kg/s

The aerodynamic performance outputs (PR, DC60) obtained from the wind tunnel test is given in Table 3.3. The calculation method of the DC60 is the same method presented in 2.3.3.2.

Table 3.3 RAE M2129 Performance Outputs [19]

<b>Aerodynamic Performance Output</b>	<b>Value</b>
PR	0.9744
DC60	0.313

### 3.1.1.2 Analysis Details and Boundary Conditions

For the CFD analysis, Ansys Fluent 2020R1 CFD solver is used. The analysis is carried out using the details given in 2.3.2. A half dome volume is constructed for the computational domain and an extension at the AIP station is added to improve convergence. An image of the computational domain with the applied boundary conditions is shown in Figure 3.2.

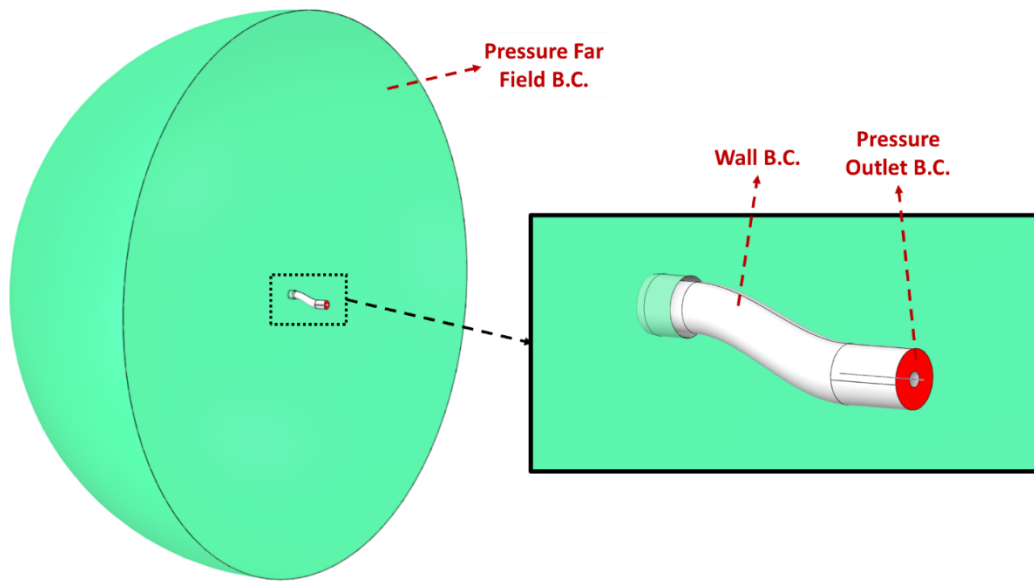


Figure 3.2. RAE M2129 Boundary Conditions

For the free-stream flow part of the outer computational domain, “Pressure Far Field” boundary condition is used which is defined by the test flow speed, static pressure, static temperature. The intake geometry is modelled as an adiabatic and no-slip wall boundary condition. The extended AIP station surface is assigned as a pressure outlet boundary condition and it is defined by the static pressure and total temperature. In the following “Mesh Independence” and “Turbulence Model Investigation” studies, the pressure outlet inputs are adjusted so that the mass flow rate at the boundary is in a certain percentile of the test result.

The mesh independence study is carried out with  $k-\omega$ -SST turbulence model to obtain the optimum mesh and after that a turbulence model selection study is carried out to obtain the most suitable turbulence model with the optimum mesh.

### 3.1.1.3 Mesh Independence Study

A mesh independence study is carried out to make the analysis results independent from the mesh size while maintaining steady result outputs. For the study, three meshes are created with increasing size. While the surface and volume sizes change

for the five meshes, the first boundary layer height is kept the same to ensure the  $y^+$  value of 1 on the wall zones. The number of volume elements of the meshes is given in Table 3.4.

Table 3.4. RAE M2129 Mesh Independence Study Mesh Details

<b>Mesh Name</b>	<b>Volume Element Count (x10<sup>6</sup>)</b>
Coarse	1.63
Medium	4.60
Fine	9.37

Sample images of the meshes are given in Figure 3.3, Figure 3.4 and Figure 3.5.

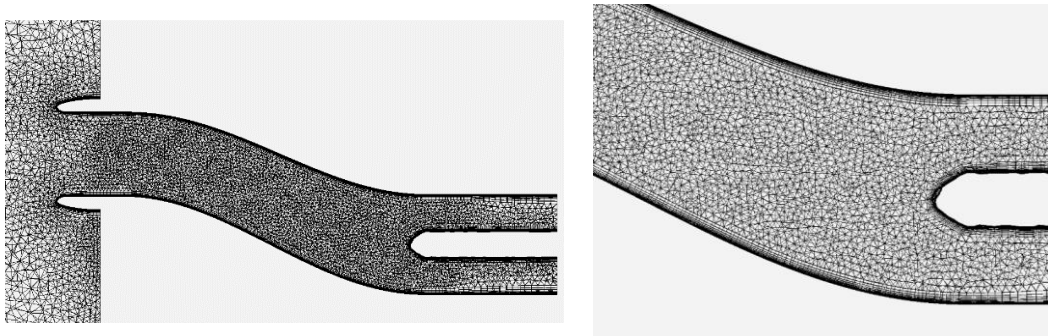


Figure 3.3. RAE M2129 Mesh Independence Study – Coarse Mesh

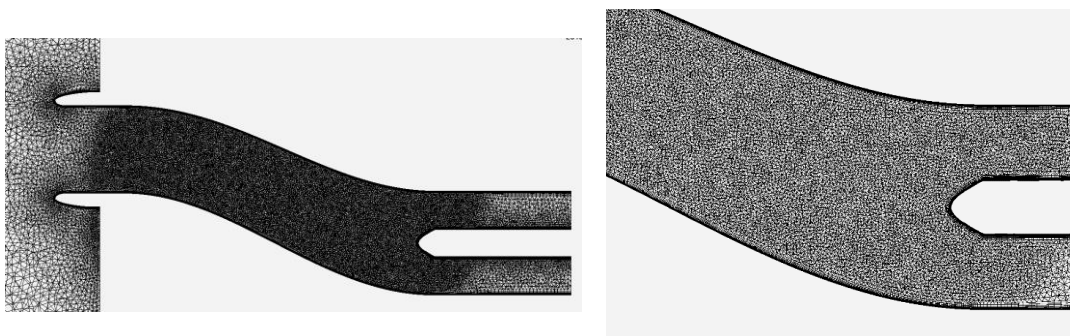


Figure 3.4. RAE M2129 Mesh Independence Study – Medium Mesh

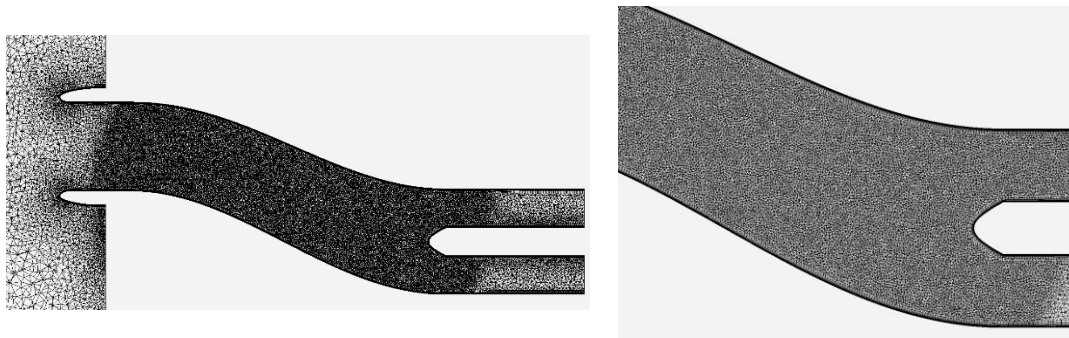


Figure 3.5. RAE M2129 Mesh Independence Study – Fine Mesh

The analyses are carried out for the flow conditions given in 3.1.1.1 and boundary conditions mentioned in 3.1.1.2. The result of the study is given in Figure 3.6 and Figure 3.7 for PR and DC60 respectively.

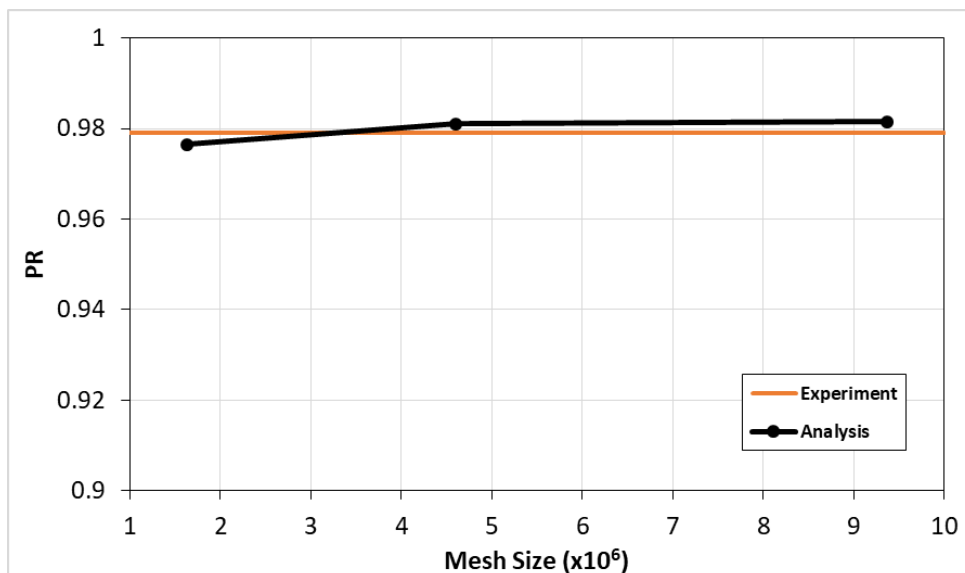


Figure 3.6. RAE M2129 Mesh Independence Study PR Results with Experimental Results [19]

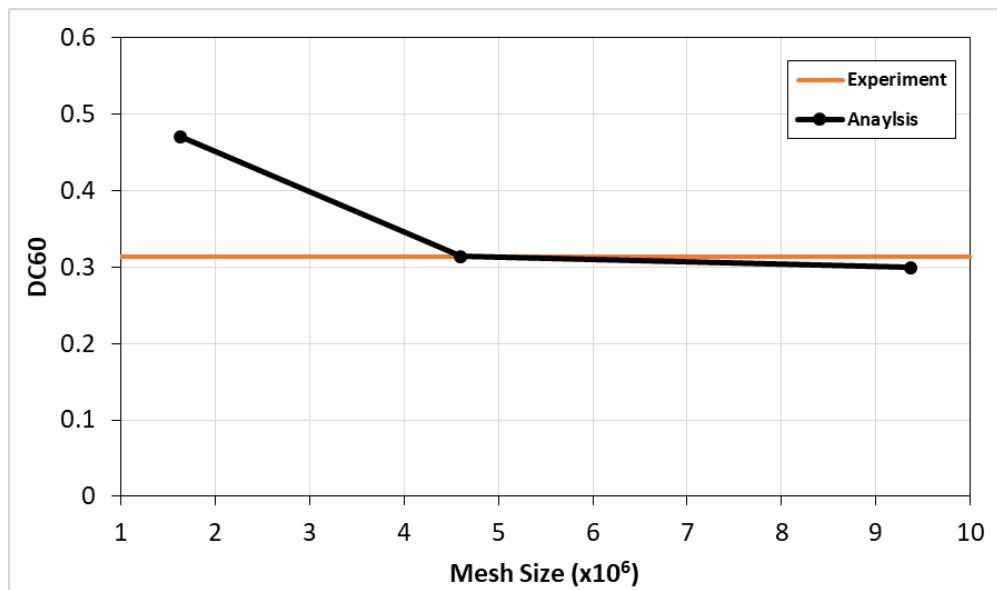


Figure 3.7. RAE M2129 Mesh Independence Study DC Results with Experimental Results [19]

The results are presented in terms of difference from the finest mesh in percentage in Table 3.5.

Table 3.5 RAE M2129 Mesh Independence Study Results

Mesh Name	Volume Element Count (1xe6)	PR	$\Delta$ PR (%)	DC60	$\Delta$ DC60 (%)
Coarse	1.63	0.9765	0.27	0.4712	-57.18
Medium	4.60	0.9810	0.03	0.3141	-4.77
Fine	9.37	0.9815	-	0.2998	-

After the graphs and tabulated data, the mesh independence study shows that the difference of PR between meshes is relatively small compared to the DC60. The difference of values is all under 1% for PR while for the DC60, the difference is under 5% for the “Medium” mesh. Also considering the experimental results, “Medium” mesh is chosen for the “Turbulence Model Investigation” study. The  $y^+$  output of wall surfaces of the “Medium” mesh is given in Figure 3.8.

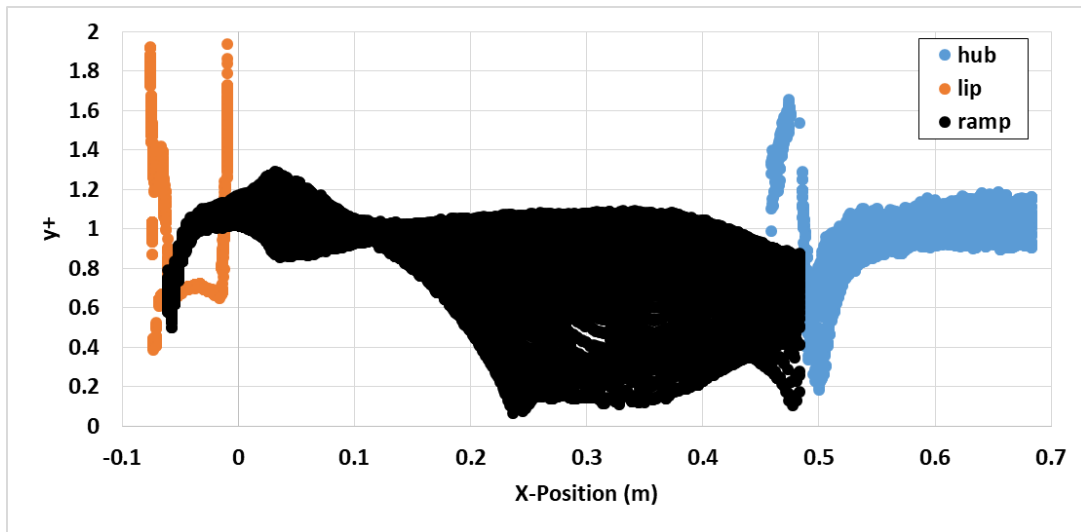


Figure 3.8. RAE M2129  $y^+$  Output of the “Medium” Mesh

### 3.1.1.4 Turbulence Model Selection

Turbulence model investigation is carried out with the “Medium” mesh to obtain the model best fitting the experimental results. Turbulence models of S-A, Realizable  $k-\varepsilon$  and  $k-\omega$ -SST are investigated using the same meshes and analysis methods mentioned in 2.3.2. The aerodynamic performance coefficients of PR and DC60 are compared with the difference from the experimental results in percentage in Table 3.6.

Table 3.6 RAE M2129 Mesh Independence Study Turbulence Investigation Results

<b>Turbulence Model</b>	<b>PR</b>	<b><math>\Delta</math>PR (%)</b>	<b>DC60</b>	<b><math>\Delta</math>DC60 (%)</b>
S-A	0.9852	-0.64	0.2873	8.21
Realizable $k-\varepsilon$	0.9819	-0.30	0.2797	10.65
$k-\omega$ -SST	0.9810	-0.21	0.3141	-0.35

It can be seen from the results that all turbulence models achieve capturing the PR value under 1% difference from the experimental results, while for the DC60, S-A

and Realizable  $k-\varepsilon$  models gives poor results by predicting the distortion of the flow poorly.

### 3.1.2 S-Shaped Duct Test Case

#### 3.1.2.1 Model Details and Test Conditions

A diffusing S-duct designed and tested at the NASA Lewis Research Center is chosen for the second validation case [43]. It is used for the research of flow physics inside S-ducts and validation of CFD solvers and methods. A sample half cut image is given in Figure 3.9.

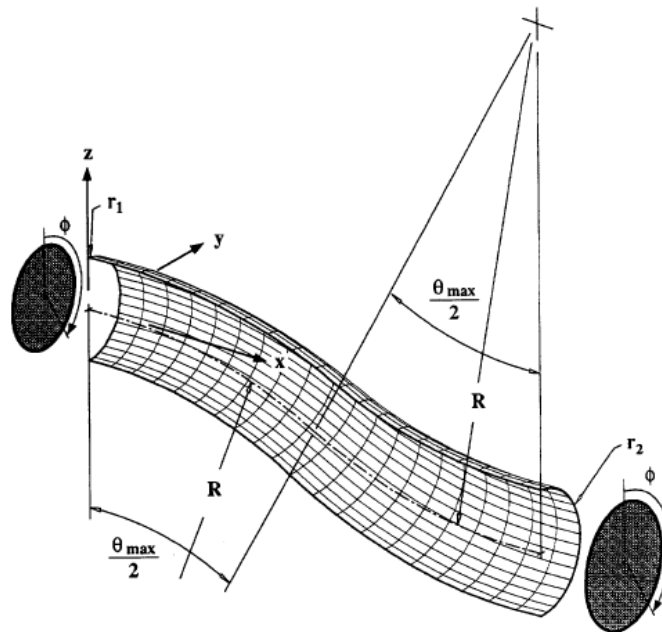


Figure 3.9. S-Shaped Duct Model Details [43]

The duct model is generated using the centreline and radius definitions provided in [43]. The centreline is defined by points of two circular arcs in 3 dimensional space using the Equations 3.1 and Equation 3.2. The radius of the circular sections between the start and end of the duct changes according to the Equation 3.3.

$$x = \begin{cases} R \sin\theta & , 0 \leq \theta \leq \theta_{max}/2 \\ 2 R \sin\left(\frac{\theta_{max}}{2}\right) - R \sin(\theta_{max} - \theta) & , \frac{\theta_{max}}{2} \leq \theta \leq \theta_{max} \end{cases} \quad (3.1)$$

$$z = \begin{cases} R \cos\theta - R & , 0 \leq \theta \leq \theta_{max}/2 \\ 2 R \cos\left(\frac{\theta_{max}}{2}\right) - R (1 + \cos(\theta_{max} - \theta)) & , \frac{\theta_{max}}{2} \leq \theta \leq \theta_{max} \end{cases} \quad (3.2)$$

$$\frac{r}{r_1} = 1 + 3 \left(\frac{r_2}{r_1} - 1\right) \left(\frac{\theta}{\theta_{max}}\right)^2 - \left(\frac{r_2}{r_1} - 1\right) \left(\frac{\theta}{\theta_{max}}\right)^3 \quad (3.3)$$

The entry section radius ( $r_1$ ) is 102.1 mm, the exit section radius is 125.7 mm and the radius used to define the circular arcs ( $R$ ) is 1020 mm. The experiment is done with the flow going through the said entry and exit sections at flow conditions given in Table 3.7.

Table 3.7 S-Shaped Duct Test Conditions [43]

<b>Flow Conditions</b>	
Free Stream Mach	0.6
Free Stream Total Pressure	115400 Pa
Free Stream Total Temperature	308.7 K
Angle of Attack	$0^\circ$
Sideslip Angle	$0^\circ$
Mass Flow Rate	7.135 kg/s

The aerodynamic performance outputs (PR, DC60) obtained from the wind tunnel test is given in Table 3.8.

Table 3.8 S-Shaped Duct Performance Outputs [43]

<b>Aerodynamic Performance Output</b>	<b>Value</b>
PR	0.971
DC60	0.358

### 3.1.2.2 Analysis Details and Boundary Conditions

For the CFD analysis, Ansys Fluent 2020R1 CFD solver is used. The analysis is carried out using the details given in 2.3.2. A duct only volume is constructed for the computational domain and extensions at the entry and the exit planes are added to improve convergence. An image of the modelled geometry with the said extensions is shown in Figure 3.10. An image of the computational domain with the applied boundary conditions is shown in Figure 3.11.

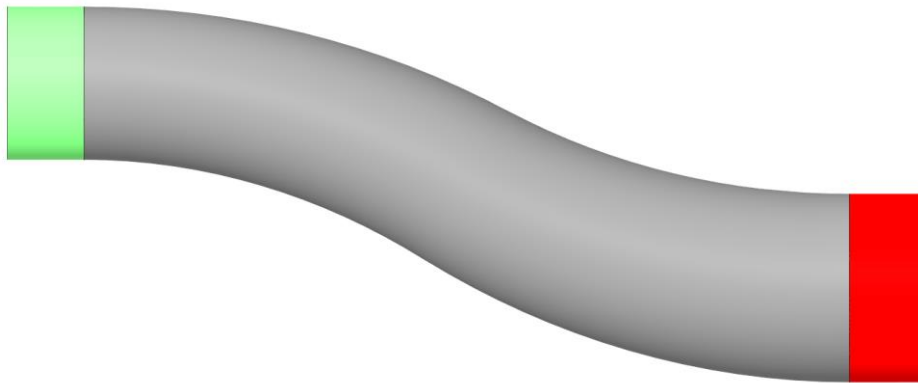


Figure 3.10. S-Shaped Duct Computational Model

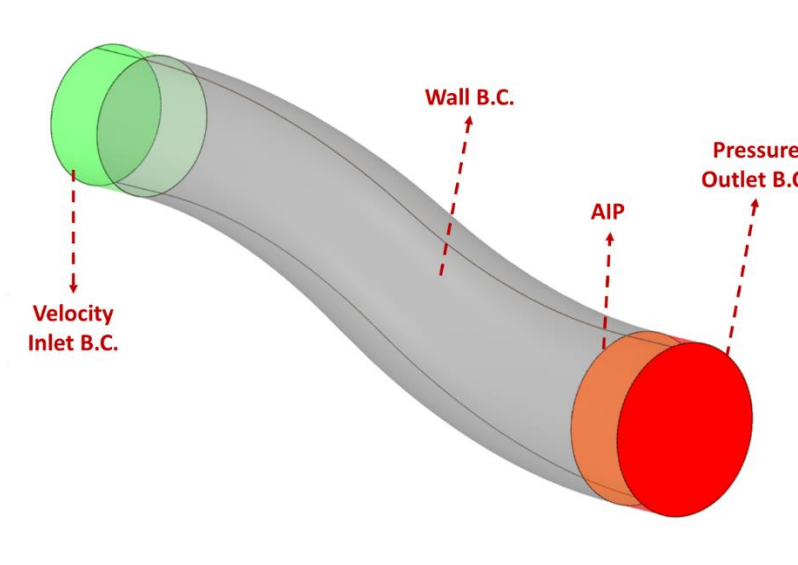


Figure 3.11. S-Shaped Duct Boundary Conditions

For the inlet of the flow, “Velocity Inlet” boundary condition is used which is defined by the flow speed, static pressure and static temperature stated in 3.1.2.1. The duct geometry with the extension outer surfaces are modelled as an adiabatic, no-slip wall boundary condition. For the exit of the flow, “Pressure Outlet” boundary condition is used which is defined by the static pressure and total temperature. The static pressure is adjusted for the following studies so that the mass flow rate at the AIP is in a certain percentile of the test result given in 3.1.2.1. The mesh independence and turbulence selection studies are done with the method followed in the previous validation case.

### 3.1.2.3 Mesh Independence Study

The mesh independence procedure followed on 3.1.1.3 is repeated for the second validation case. For the study, four meshes are created with increasing size. The number of volume elements of the meshes is given in Table 3.9.

Table 3.9 S-Shaped Duct Mesh Independence Study Mesh Details

<b>Mesh Name</b>	<b>Volume Element Count (x10<sup>5</sup>)</b>
Very Coarse	4.2
Coarse	8.3
Medium	14.0
Fine	20.0

Sample images of the meshes is given in Figure 3.12, Figure 3.13, Figure 3.14 and Figure 3.15.

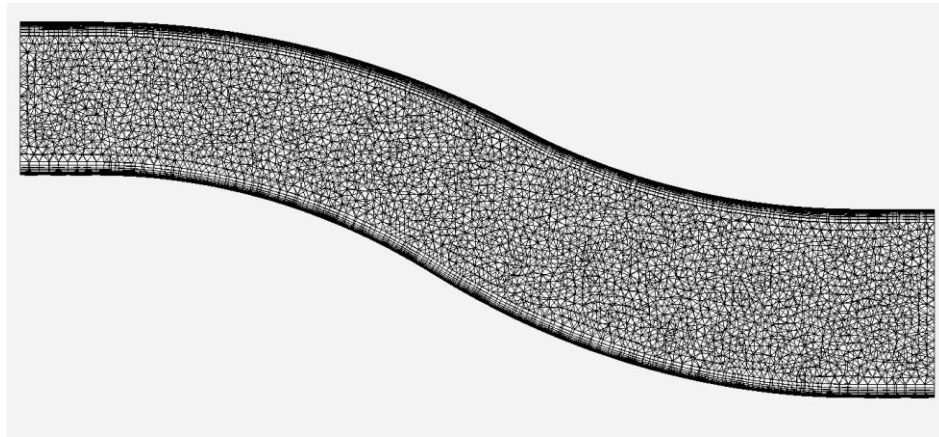


Figure 3.12. S-Shaped Duct Mesh Independence Study – Very Coarse Mesh

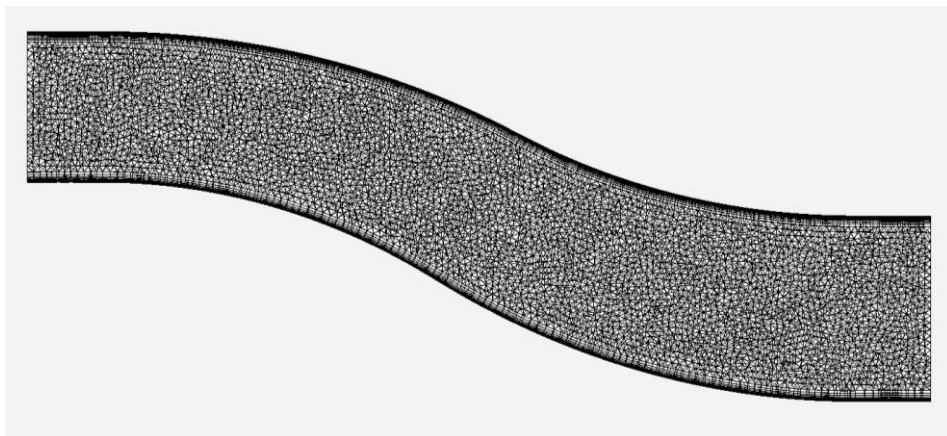


Figure 3.13. S-Shaped Duct Mesh Independence Study – Coarse Mesh

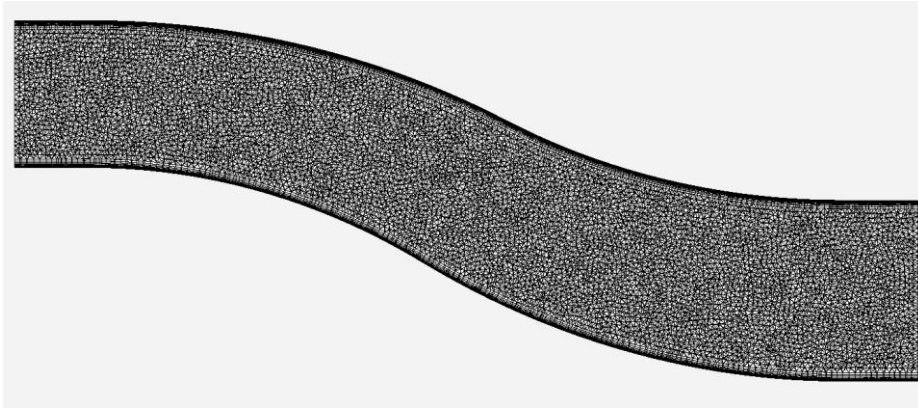


Figure 3.14. S-Shaped Duct Mesh Independence Study – Medium Mesh

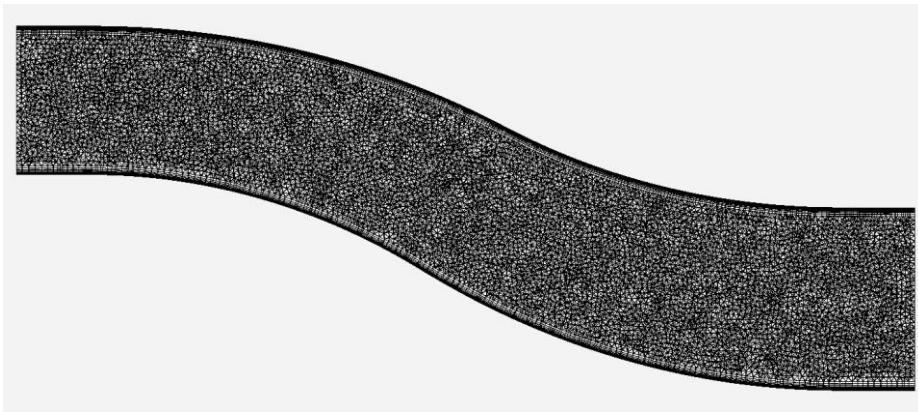


Figure 3.15. S-Shaped Duct Mesh Independence Study – Fine Mesh

The analyses are carried out for the flow conditions given in 3.1.2.1 and boundary conditions mentioned in 3.1.2.2. The result of the study is given in Figure 3.16 and Figure 3.17 for PR and DC60 respectively.

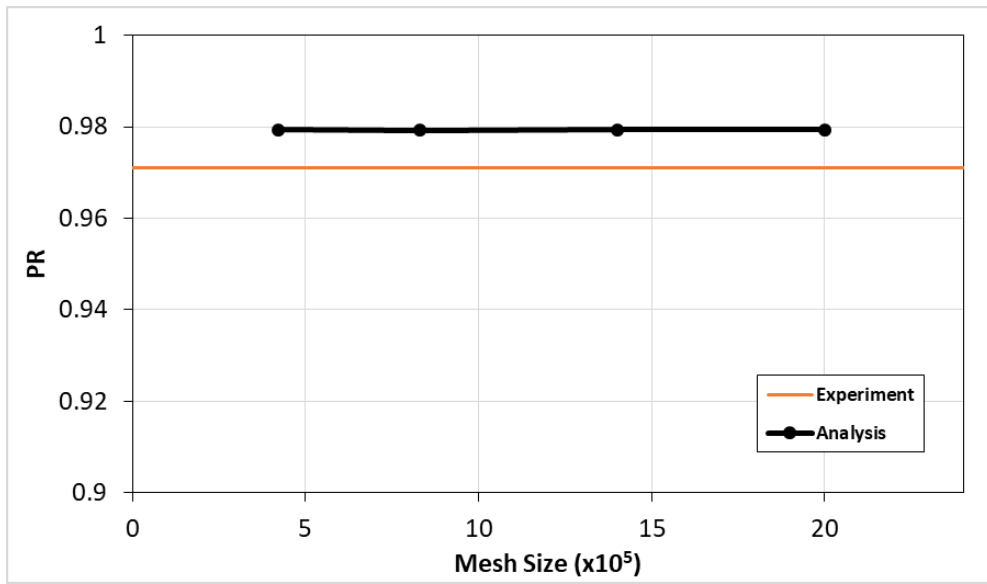


Figure 3.16. S-Shape Duct Mesh Independence Study PR Results with Experimental Results [43]

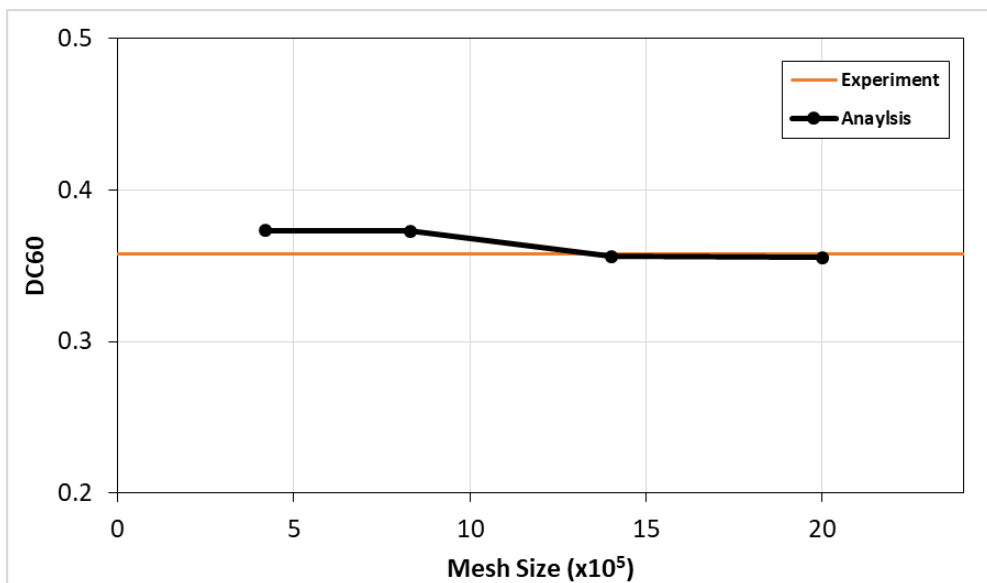


Figure 3.17. S-Shape Duct Mesh Independence Study DC Results with Experimental Results [43]

The results are presented in terms of difference from the finest mesh in percentage in Table 3.10.

Table 3.10 S-Shaped Duct Mesh Independence Study Results

Mesh Name	Volume Element Count (x10 <sup>5</sup> )	PR	$\Delta$ PR (%)	DC60	$\Delta$ DC60 (%)
Very Coarse	4.2	0.9794	0.01	0.3731	-4.94
Coarse	8.3	0.9793	0.02	0.3729	-4.87
Medium	14.0	0.9793	0.01	0.3561	-0.15
Fine	20.0	0.9794	-	0.3555	-

After the graphs and tabulated data, the PR values of the meshes are quite close, the difference of values is all under 0.1% while for the DC60, the difference is under 1% for the “Medium” mesh. Also considering the experimental value, “Medium” mesh is chosen for the “Turbulence Model Investigation” study. The  $y^+$  output of the “Medium” mesh is given in Figure 3.18.

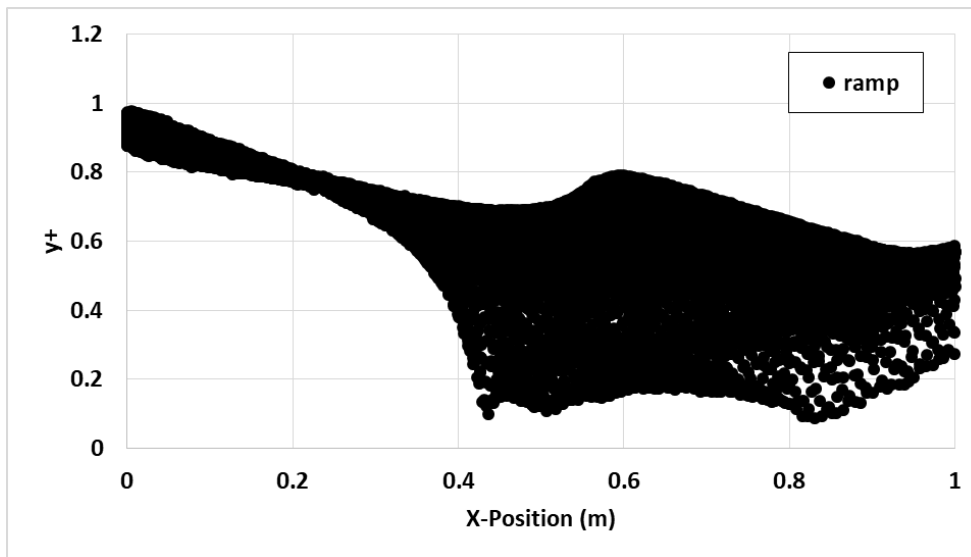


Figure 3.18. S-Shaped Duct  $y^+$  Output of the “Medium” Mesh

### 3.1.2.4 Turbulence Model Selection

Turbulence model investigation is carried out with the “Medium” mesh to obtain the model best fitting the experimental results. Turbulence models of S-A, Realizable k- $\varepsilon$  and k- $\omega$ -SST are investigated using the same meshes and analysis methods mentioned in 2.3.2. The aerodynamic performance coefficients of PR and DC60 are compared with the difference from the experimental results in percentage in Table 3.11.

Table 3.11 S-Shaped Duct Mesh Independence Study Turbulence Investigation Results

<b>Turbulence Model</b>	<b>PR</b>	<b><math>\Delta</math>PR (%)</b>	<b>DC60</b>	<b><math>\Delta</math>DC60 (%)</b>
S-A	0.9759	-0.51	0.3813	-6.51
Realizable k- $\varepsilon$	0.9743	-0.34	0.1930	46.10
k- $\omega$ -SST	0.9793	-0.85	0.3561	-0.53

It can be seen from the results that all turbulence models achieve capturing the PR value under 1% difference from the experimental results, while for the DC60, only k- $\omega$ -SST model predicts under 1% difference.

### 3.1.3 CFD Validation Overview

With the two validation cases, an S-duct intake with lip operating at low subsonic speed and an S-duct operating at subsonic speeds are covered. With the intake concepts similar to the intake design of topic discussed, the method of meshing and CFD analyses are covered. For both of the cases, similar sizing is used for the meshing and “Fine” sized meshing is selected and k- $\omega$ -SST gave out the best result at capturing the aerodynamic performance outputs. According to the obtained results, S-A and Realizable k- $\varepsilon$  models achieve predicting the PR sufficiently while

they fail at predicting the swirling and distortion of the flow. Considering the obtained results, following methods for the meshing and analyses will be followed in the design studies.

- Since the intake design will be done via a DOE processes with intake designs of various sizes, method of meshing of the duct is fixed with the sizing settings used for “Fine” mesh sizes.
- $k-\omega$ -SST turbulence model will be used for the CFD analyses as it gave the best results for the both aerodynamic performance outputs.

## **3.2 RCS Validation Studies**

Three validation cases are selected for the RCS validation studies. The cases are selected for the validation of the method explained in 2.4.2, the solver and the feasibility of the usage of this method on intakes. The cases are investigated in the following sections.

### **3.2.1 Triangular Prism Benchmark Test Case**

#### **3.2.1.1 Model Details and Test Conditions**

A benchmark triangular prism model which is experimented for the validation of electromagnetics prediction tools is used for the test case [21]. The case is chosen to test the ability of the tool to predict the diffraction as the planar surfaces of the prism forms sharp edges. The base of the triangular prism have edges of different dimensions, so the diffraction caused by the edges should differentiate. The target model geometry is shown in Figure 3.19.

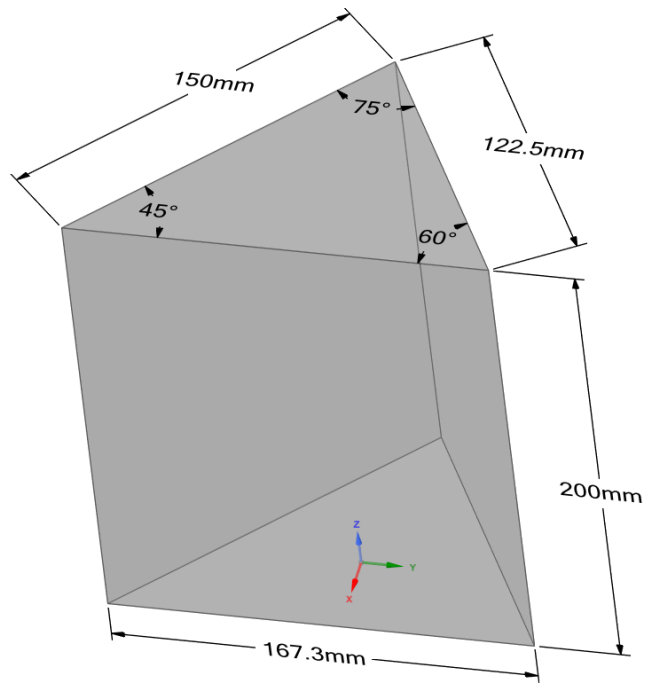


Figure 3.19. Triangular Prism Model

The test conditions are given in Table 3.12. The test model is made of aluminium material. The outputs of the tests are available as RCS in terms of  $\text{dBm}^2$  with respect to azimuth angle.

Table 3.12 Triangular Prism Test Conditions [21]

<b>Frequency</b>	8 GHz
<b>Azimuth Angle Interval (<math>\phi</math>)</b>	$0^\circ$ to $360^\circ$ with $1^\circ$ step
<b>Elevation Angle Interval (<math>\theta</math>)</b>	$0^\circ$
<b>Polarization</b>	Vertical – Vertical

### 3.2.1.2 Analysis Results and Comparison

The electromagnetics analysis is carried out with the commercial tool Ansys HFSS using the SBR+ method mentioned in 2.4.2. The geometry is modelled as PEC

material and the analysis is carried out with settings mentioned in 2.4.3. The results of RCS output in comparison with the experimental results are given in Figure 3.20.

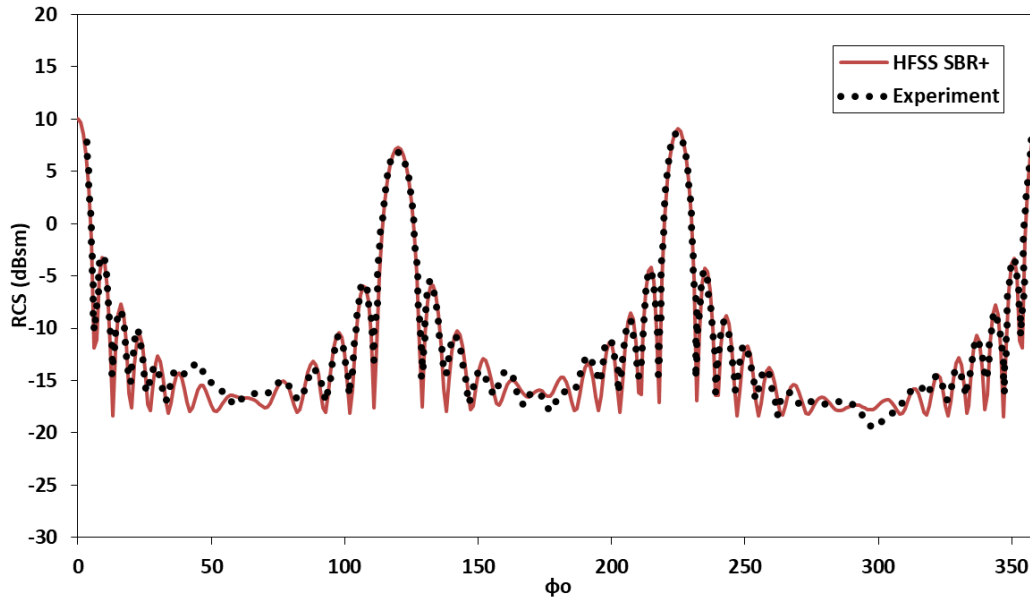


Figure 3.20. Triangular Prism Results Comparison with Experimental Data [21]

The results show that the analysis results shows good agreement with the experiment. It can be seen that at azimuth angles directed towards the planar surfaces at the right angles, the RCS values are expectedly the highest and the agreement is the best between data. However at azimuth angles directed towards the edges ( $60^\circ - 175^\circ - 300^\circ$ ), it can be seen that analysis results are not on point. The disagreement can be evaluated as the method do not perfectly capture the diffraction effect caused by the edges, but the small differences are considered acceptable.

## 3.2.2 Truncated Cone Benchmark Test Case

### 3.2.2.1 Model Details and Test Conditions

A benchmark truncated cone model which is experimented for the validation of electromagnetics prediction tools is used for the test case [21]. The case is chosen to test the ability of the tool to predict the reflection off of inclined surfaces and the

diffraction caused by the curved edges. Being a truncated cone, the circular surfaces have edges of different diameters, so like the triangular prism, the diffraction caused by the edges should differentiate. The target model geometry is shown in Figure 3.21.

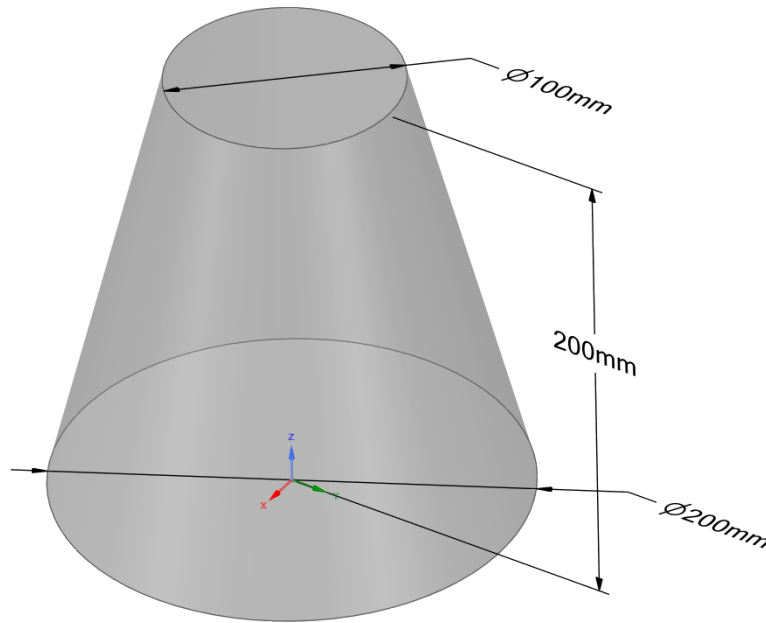


Figure 3.21. Truncated Cone Model

The test conditions are given in Table 3.13. The test model is made of aluminium material. The outputs of the tests are available as RCS in terms of  $\text{dBm}^2$  with respect to elevation angle.

Table 3.13 Truncated Cone Test Conditions [21]

<b>Frequency</b>	6 GHz
<b>Azimuth Angle Interval (<math>\phi</math>)</b>	$0^\circ$
<b>Elevation Angle Interval (<math>\theta</math>)</b>	$0^\circ$ to $180^\circ$ with $1^\circ$ step
<b>Polarization</b>	Horizontal – Horizontal

### 3.2.2.2 Analysis Results and Comparison

The electromagnetics analysis is carried out with the commercial tool ANSYS HFSS using the SBR+ method mentioned in 2.4.2. The geometry is modelled as PEC material and the analysis is carried out with settings mentioned in 2.4.3. The results of RCS output in comparison with the experimental results are given in Figure 3.22.

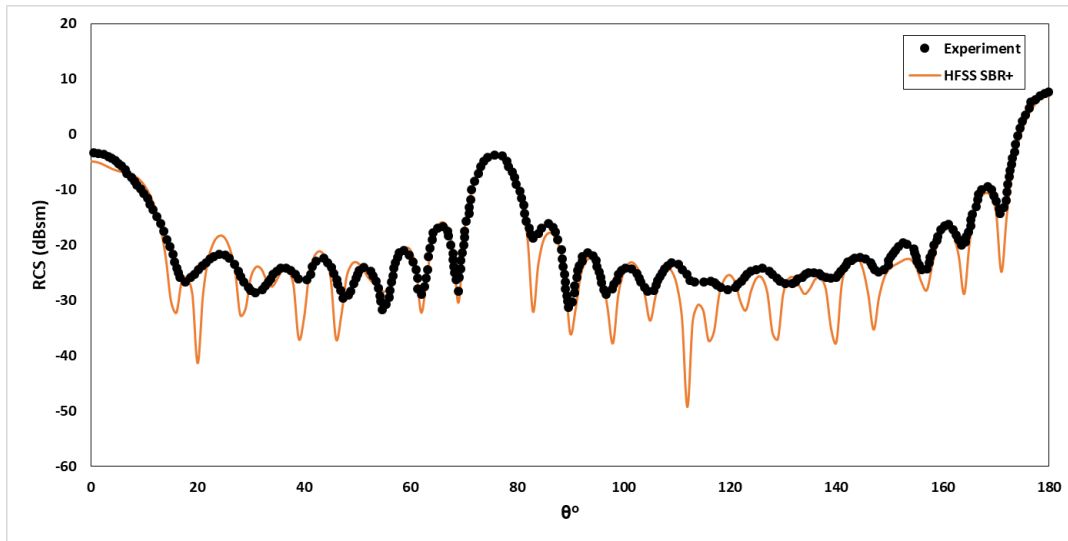


Figure 3.22. Truncated Cone Results Comparison with Experimental Data [21]

The results show that the analysis results captures the trend of the experiment. It can be seen that at elevation angles directed towards the surfaces at the right angles, the RCS values are expectedly the highest and the agreement is the best between data. However at other elevation angles, the analysis results show oscillations and fails to capture the low RCS values. The disagreement at low RCS values is evaluated such that either method fails to capture the creeping wave effect caused by the curved surfaces or the experimental values are over-smoothed since the experimental RCS data tend to include large amount of noise. Since the maximum values and the overall trend are captured well, the results are considered acceptable.

### 3.2.3 Simple Duct Test Case

#### 3.2.3.1 Model Details and Test Conditions

A full-scale intake duct model is used for the test case [22]. The case is chosen to test the ability of the tool to predict the RCS of cavities which is essential for the intake design process. Experimental RCS data of full-scale objects are much desired for the validation of electromagnetics codes but rarely available in the literature for secrecy concerns as most studies are done for military applications. Unlike the previous RCS validation cases, multiple wave bounces inside the duct are expected to occur.

The test case at hand features a cavity consisting of a straight duct and a terminating plate at the end. The duct opening is 0.7 m in diameter and the duct is 1.9 m long. The duct wall is 1 mm in thickness. The scattering caused by the wall thickness at the front face is considered negligible because of the X-band test frequency. The experimental setup features RAM on the exterior part of the setup so only the duct is illuminated by the waves. An image of the experimental setup obtained from [22] and the model details are shown in Figure 3.23 and Figure 3.24.

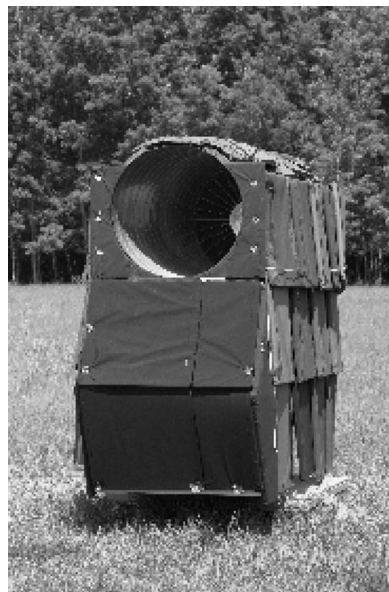


Figure 3.23. Simple Duct Experimental Model [22]

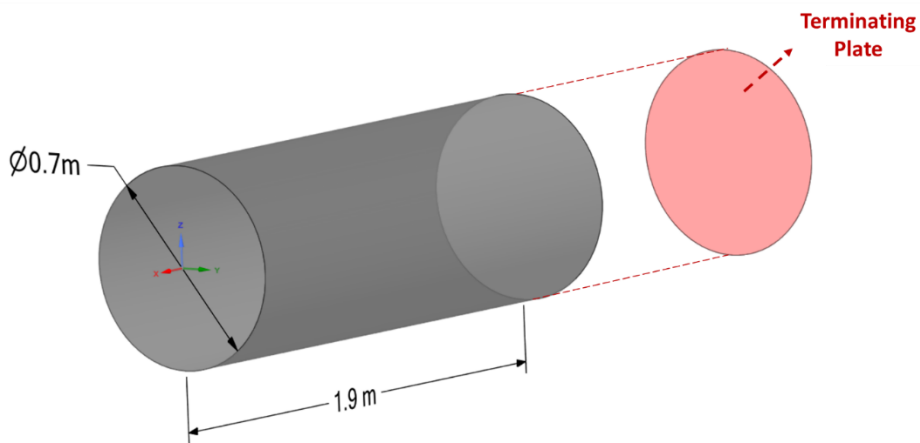


Figure 3.24. Simple Duct Model

The test is done satisfying the far-field condition with the test conditions given in Table 3.14.

Table 3.14 Simple Duct Test Conditions [22]

<b>Frequency</b>	8.9 GHz
<b>Azimuth Angle Interval (<math>\phi</math>)</b>	$-60^\circ$ to $+60^\circ$
<b>Elevation Angle Interval (<math>\theta</math>)</b>	$90^\circ$
<b>Polarization</b>	Horizontal – Horizontal

### 3.2.3.2 Analysis Results and Comparison

The electromagnetics analysis is carried out with the commercial tool Ansys HFSS using the SBR+ method mentioned in 2.4.2. The geometry is modelled as PEC material and the analysis is carried out with settings mentioned in 2.4.3. The analysis is carried out at the azimuth angles between  $-50^\circ$  and  $+50^\circ$ , because the experimental data outside this bound include a lot of noise. The results of RCS output in comparison with the experimental results are given in Figure 3.25.

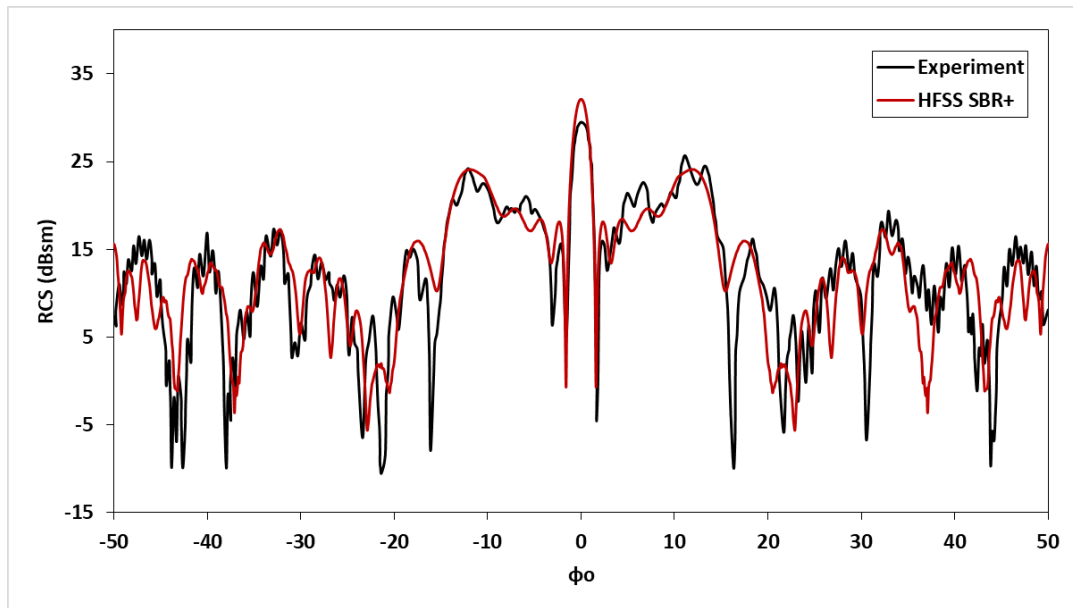


Figure 3.25. Simple Duct Results Comparison with the Experimental Data [22]

It can be seen from the results that even though the experimental data include a fair amount of noise, the analysis data show good agreement. Even though the model has a symmetrical profile in the azimuthal plane, the experimental data have unsymmetrical features across the azimuth angles. The direct illumination angle ( $\phi = 0^\circ$ ) shows maximum RCS output for both results with the analysis slightly overshooting. For the other illumination angles, the analysis results follow the trend of the experimental results at the local base and peak locations. With the deductions made, the SBR+ method is deemed usable for the cavity like structures.

### 3.2.4 RCS Validation Overview

With the three validation cases, two benchmark and a simple intake duct RCS analyses are covered. The commercial electromagnetics analysis program, ANSYS HFSS tool is used with the SBR+ method mentioned in 2.4.2. For all cases, the comparison of analysis results with the experimental data showed good agreement. For the simple geometries like the prism and cone, the experimental results include smooth data without noise, the RCS outputs are captured best at maximum reflection

angles and small differences are seen at diffraction angles. For more complex geometries like the cavities, the experimental results include noisier data but the general trend of the experimental data is captured, so it can be deduced that the multiple bounces of waves are predicted well enough. Regarding the deductions made, SBR+ method is validated for the use of intake design RCS analyses.

## CHAPTER 4

### INTAKE DESIGN PROCESS

The intake design process follows the design optimization with the SBAO methodology explained in “2.2.”. The design procedure includes the following steps with the intended outcomes.

- A “definitive screening design” is carried out for the parameter screening and selection. The effect of parameters on the performance coefficients are investigated.
- A “design of experiments” study is carried out with the selected parameters for the RSM sample points. Parameters’ effect on the performance coefficients are again investigated with the DOE sample set and compared to the DSD study.
- A “response surface model” is generated with the obtained DOE sample points. The validation of the model is investigated with the cross-validation approach.
- A “multi-objective optimization” is carried out using the generated model. Highest performing design is investigated and prepared for the validation.

The given design procedure is carried out for the intake concept proposed in 2.1. The problem of the intake concept design is elaborated in the following sections and the design procedure elements thereafter.

#### **4.1 Design Problem Description**

The proposed intake concept features a double curved S-duct geometry with an objective of achieving the highest aerodynamic performance while lowering the RCS. The intake model can be installed on cruising airframes such as UAVs or

missiles with air breathing propulsion systems. The size and operation condition of the intake is driven by the airframe and the turbojet engine. The selection of the size and operating conditions are done considering the intended integration of the intake with a small turbojet engine. The selections and assumptions made for the operation conditions is given in the list below.

- The airframe’s steady flight conditions (the intake design point) is given in Table 4.1.

Table 4.1 Design Point Flight Conditions

<b>Flight Speed [Mach]</b>	0.9
<b>Flight Altitude [m]</b>	0 (Sea Level)
<b>Angle of Attack [°]</b>	0
<b>Sideslip Angle [°]</b>	0
<b>Ambient Pressure [Pa]</b> (ISA - Sea Level)	101325
<b>Ambient Temperature [K]</b> (ISA - Sea Level)	288.15

- The engine requires an air mass flow rate (MFR) of 4.5 kg/s at 100% RPM with the assumption that the required mass flow rate does not change with the changing intake PR. Also the CFD analyses with achieving the MFR between 4.275 kg/s and 4.725 kg/s ( $\pm 5\%$  of target MFR) are counted valid.

The selections and assumptions made for the sizing of the intake is given in the following section.

The airframe houses both the propulsion system and the intake. The engine and a part of the intake are contained in a hypothetical circular space with the engine system placed axially at the centre of it. The said circular space is fixed with a diameter of 300 mm. The airframe limits the height that the duct can take up in.

The parametric intake model features a fixed AIP station profile which represents the engine compressor face determined by the engine. Several turbojet engines aimed to be used with UAV or missile platforms available in literature are examined including TDI-J85, PBS TJ150 and TEI TJ300 [44]–[46]. Examined engines can be categorized as micro turbojet engines with outside diameters around 250 mm. Although the exact AIP profile dimensions of the said engines are unknown, an AIP station profile with similar properties are assumed. The decided profile features an AIP diameter of 172 mm and a hub diameter of 64 mm, forming an AIP area of  $\sim 0.0195 \text{ m}^2$ . The hub geometry has a conic feature with a base of said diameter of 64 mm and a height of 39 mm. The AIP geometry is shown in Figure 4.1.

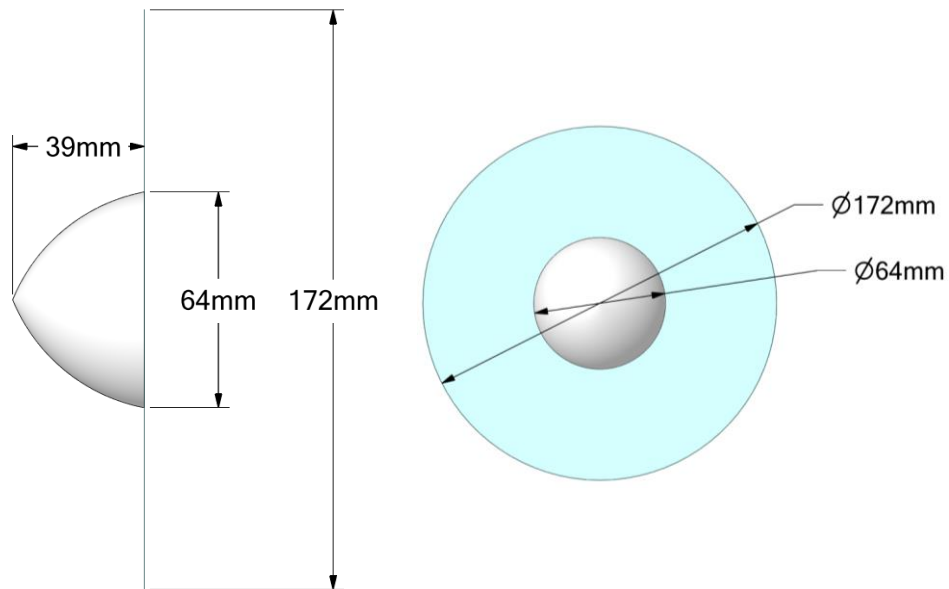


Figure 4.1. Design AIP Geometry Dimensions

The parametric intake model features a fixed lip section with throat station mentioned in 2.1. The throat area is determined through isentropic relations with the design point flight conditions and the mass flow the engine requires at the design point. The steps of calculating throat area is listed below.

- Same amount of air must pass through the throat and AIP stations, which means the continuity equation can be applied between the stations. With the

AIP area are set previously, determination of the throat area is done with the calculations of the primitive air properties at the stations.

- A PR of 0.9 is assumed for the area calculation and the resulting total pressure loss is included in the calculations. Average flow speed of 0.45 Mach is assumed at the AIP. An area ratio of 1.25 is assumed between the capture and throat area ( $A_{\text{capture}}/A_{\text{throat}}$ ).
- With the assumptions in mind, mass flow rate calculation is done at the stations with the flow speed reduction from 0.9 Mach at the capture area to 0.45 at the AIP. Resulting throat area is  $\sim 0.0125 \text{ m}^2$  and the capture areas is  $\sim 0.0157 \text{ m}^2$ .

A lip model with a throat area is constructed using the features mentioned in 2.1.1. Constructed model satisfies the throat area of  $\sim 0.0157 \text{ m}^2$  with the features of the lip model given in Table 4.2. An image of the lip geometry with the dimensions is given in Figure 4.2.

Table 4.2 Design Intake Lip Dimensions

<b>Lip Parameter</b>	<b>Value</b>
LZ1	215.0 mm
LZ2	125.7 mm
LY	89.3 mm
Profile Angle	63.4°
H-angle	140°
V-angle	110°

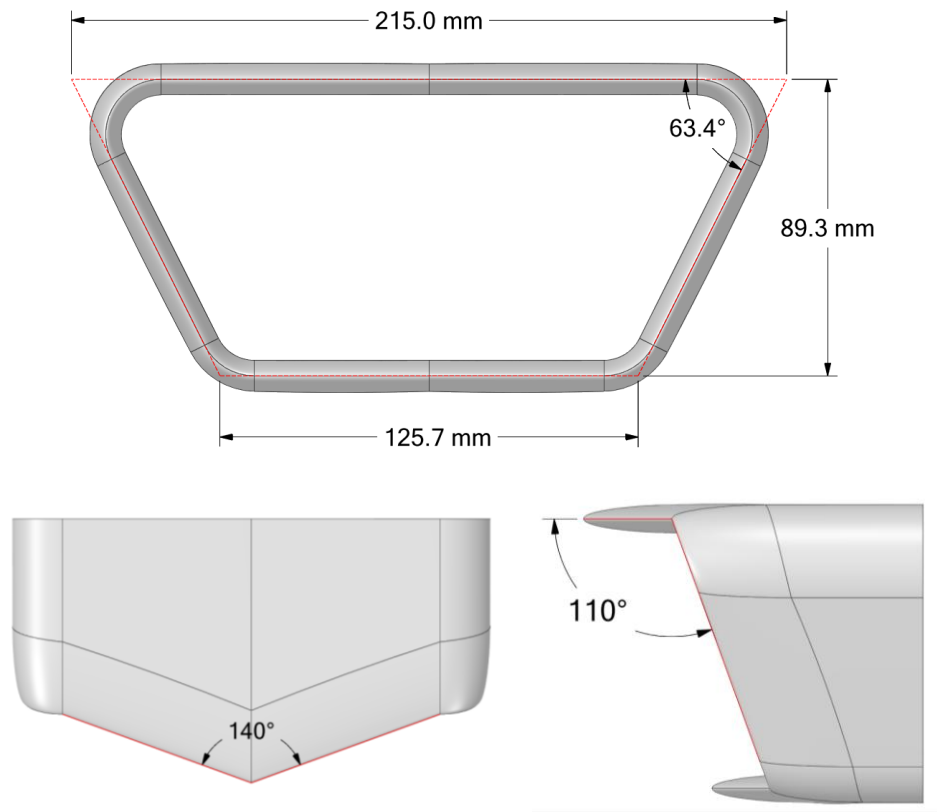


Figure 4.2. Design Intake Lip Dimensional Details

With the lip model and the AIP station details determined, limits of the parametric model is decided. Considering the parametric model mentioned in 2.1, there are total of 9 parameters,  $L_1$ ,  $H_1$  and  $k_1$  for the first duct part,  $L_2$ ,  $H_2$  and  $k_2$  for the second duct part and  $e_1$ ,  $e_2$ ,  $e_3$  for the middle station. Length and height dimensions are defined from the centre of the throat area. The height of the AIP station centre,  $H_2$ , is fixed and determined by the lip geometry, a hypothetical diverter height of 30 mm and the hypothetical airframe circular diameter of 300 mm. The limits of the 9 parameters are defined as in Table 4.3.

Table 4.3 Design Space Parameter Limits

		Minimum	Baseline	Maximum
<b>First Duct Part</b>	<b>L1 [m]</b>	0.3375	0.375	0.45
	<b>H1 [m]</b>	0.26	0.28	0.30
	<b>k1</b>	0.4	0.5	0.6
<b>Second Duct Part</b>	<b>L2 [m]</b>	0.675	0.75	0.9
	<b>H2 [m]</b>	-	0.23	-
	<b>k2</b>	0.4	0.5	0.6
<b>Middle Station</b>	<b>e1 [mm]</b>	75	85	95
	<b>e2 [mm]</b>	50	60	70
	<b>e3 [mm]</b>	65	70	75

The design space driven by the given parameters is visualized in Figure 4.3. The length and the height of the first duct part can vary with the changing middle station parameters. The AIP station profile and height is fixed and its design space is limited axially. The selection of the AIP station parameters were explained previously, but the selection of other parameters like the duct lengths are estimated as there are no official information on such dimensions in literature due to secrecy concerns.

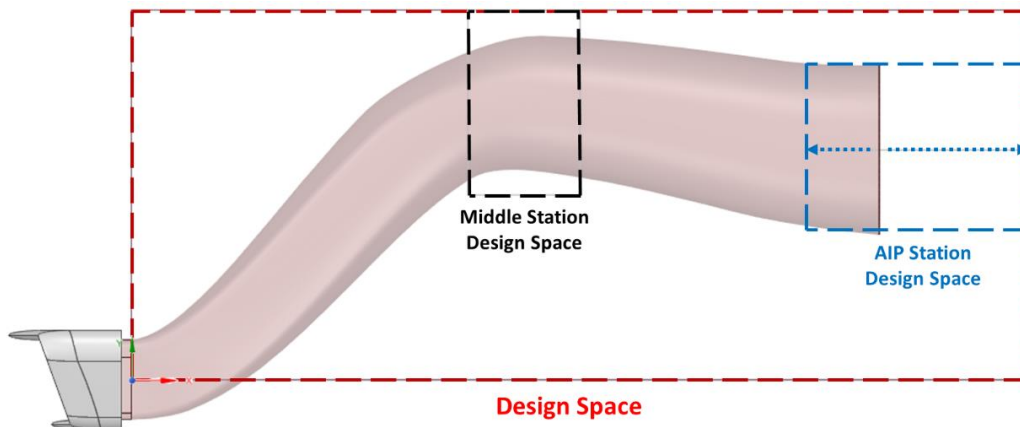


Figure 4.3. Design Space Limits

The middle station parameters are selected in accordance with the AIP profile. Parameter limits are selected so that elliptical, circular and semi-circular profiles are tried. Several profiles are shown in Figure 4.4.

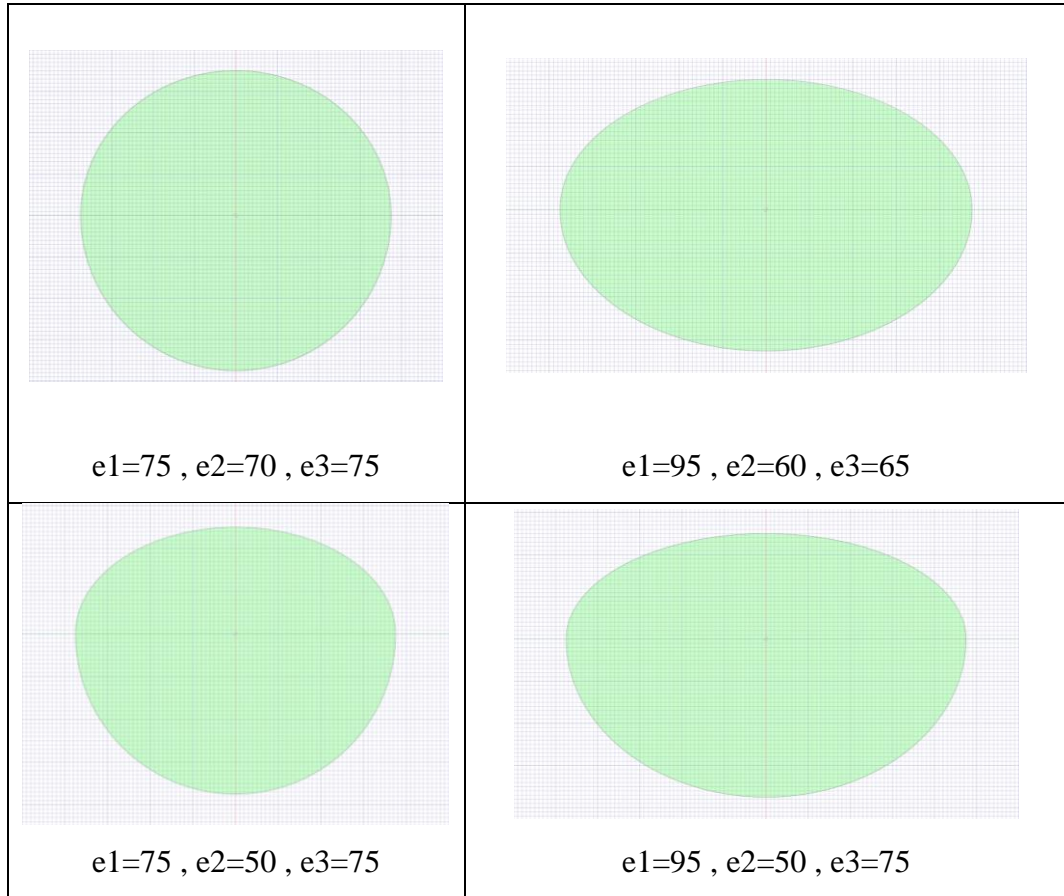


Figure 4.4. Middle Station Profile Examples

Apart from the flight conditions defined as the aerodynamic design point, the RCS analysis is carried out at the conditions given in Table 4.4.

Table 4.4. Design RCS Conditions

<b>Frequency</b>	8 GHz
<b>Azimuth Angle Interval (<math>\phi</math>)</b>	60° to 120° with 1° step
<b>Elevation Angle Interval (<math>\theta</math>)</b>	180° to 200° with 5° step
<b>Polarization</b>	Vertical – Vertical

With the operating conditions and sizings defined, the design space is described and the problem is ready for the studies explained in the following sections.

## 4.2 Definitive Screening Design Study

A DSD study with the method explained in 2.2.1 is carried out for the identification of the parameters and their effect on the performance parameters of PR, DC and RCS. The DSD is used to decide on parameters to be used in the DOE study. The mentioned parameters of the intake are taken in hand as continuous values at three levels given in the design space. The three levels are indicated as -1, 0 and 1 representing low, medium and high values. JMP creates  $2n+1$  design points for  $n$  variables, which makes 17 design points for 8 variables. The CFD and RCS processes are carried out at the said design points. The design points along with the performance outputs are given in Table 4.5.

Table 4.5. DSD – Design Details and Results

Design #	Factors								Responses		
	L1	L2	K1	K2	H1	e1	e2	e3	PR	DC	RCS [dBm <sup>2</sup> ]
1	0	0	0	0	0	0	0	0	0.9386	0.7889	-7.7
2	1	-1	-1	1	1	0	-1	-1	0.9514	0.6808	-10.5
3	1	1	-1	-1	0	1	1	-1	0.9124	0.3065	-7.8
4	1	0	1	1	1	1	1	1	0.9393	0.5267	-10.4
5	-1	-1	1	-1	1	1	0	-1	0.9134	0.8967	-9.6
6	1	-1	0	-1	-1	1	-1	1	0.9415	0.3068	-12.0
7	-1	1	1	-1	-1	0	1	1	0.9311	0.7531	-7.5
8	0	-1	-1	-1	1	-1	1	1	0.8068	0.7149	-11.0
9	-1	1	-1	0	1	1	-1	1	0.7483	1.0177	-14.5
10	-1	0	-1	-1	-1	-1	-1	-1	0.8290	1.3046	-7.2

Table 4.5. DSD – Design Details and Results (continued)

Design #	Factors								Responses		
	L1	L2	K1	K2	H1	e1	e2	e3	PR	DC	RCS [dBm <sup>2</sup> ]
11	1	1	1	-1	1	-1	-1	0	0.9167	0.9816	-8.8
12	1	1	-1	1	-1	-1	0	1	0.8751	0.8720	-7.2
13	1	-1	1	0	-1	-1	1	-1	0.9510	0.7872	-7.7
14	0	1	1	1	-1	1	-1	-1	0.9327	0.7274	-8.4
15	-1	1	0	1	1	-1	1	-1	0.8270	0.9471	-10.8
16	-1	-1	-1	1	-1	1	1	0	0.8032	0.8764	-10.8
17	-1	-1	1	1	0	-1	-1	1	0.8974	1.1634	-8.8

The baseline design is the first design and all of its variables are at the baseline values. The PR values range from 0.7483 to 0.9514, the DC from 0.3065 to 1.3046 and the RCS from -7.2 to -14.5 dBm<sup>2</sup>. The variables are investigated for all responses (performance outputs) using the approach mentioned in 2.2.1. Investigations are explained in the sections as follows.

#### 4.2.1 DSD – PR Investigation

The JMP output for the PR is given in Figure 4.5. The output for PR shows the main effects of the factors and the significant two-factor interactions. Considering the lower p-value meaning higher level of significance, K1, L1 and K1\*L1 are below the 0.1 the p-value threshold causing highest effects on PR. The results for the PR makes sense as it is expected that the first duct part should be more important for the pressure recovery; the curvature is more severe for the first duct part and the L1, K1 are the parameters that drives the first spline.

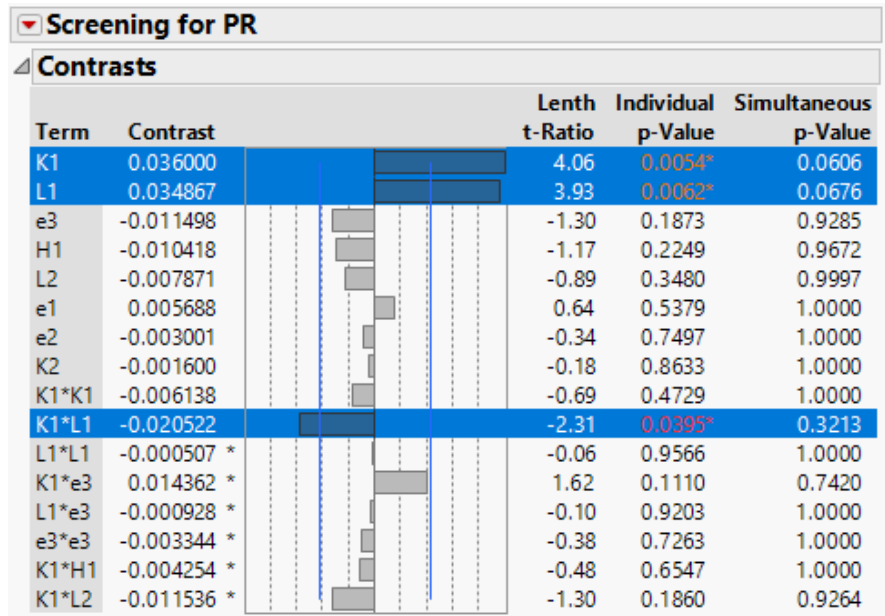


Figure 4.5. DSD – PR Results

#### 4.2.2 DSD – DC Investigation

The JMP output for the DC is given in Figure 4.6.

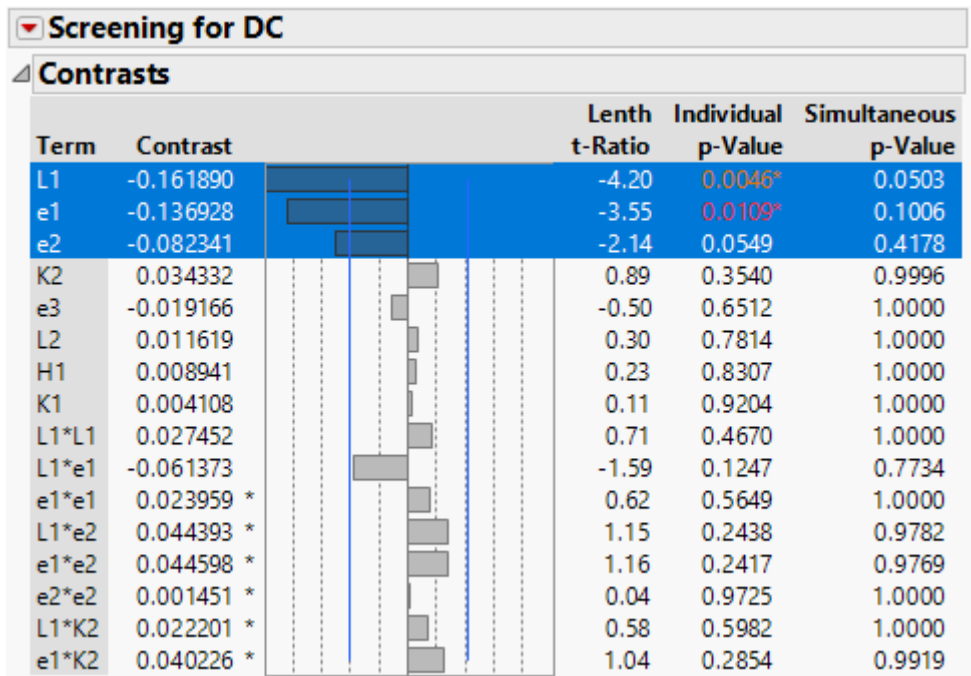


Figure 4.6. DSD – DC Results

Same deductions made for the PR output are made for the DC and the results show that L1, e1 and e3 factors are important with the L1\*e1 interaction following next. The results show that that the length of the first duct part and the middle profile parameters are effective for the DC output.

### 4.2.3 DSD – RCS Investigation

The JMP output for the RCS is given in Figure 4.7.

Screening for RCS						
Contrasts						
Term	Contrast		Lenth	Individual	Simultaneous	
			t-Ratio	p-Value	p-Value	
H1	-0.959342		-1.79	0.0783	0.6293	
e1	-0.777844		-1.45	0.1407	0.8569	
e3	-0.609312		-1.14	0.2356	0.9794	
K1	0.505599		0.94	0.3172	0.9987	
L2	0.350030		0.65	0.5278	1.0000	
L1	0.311138		0.58	0.5917	1.0000	
e2	0.272246		0.51	0.6441	1.0000	
K2	-0.194461		-0.36	0.7436	1.0000	
H1*H1	-0.626290		-1.17	0.2240	0.9739	
H1*e1	0.364073		0.68	0.4868	1.0000	
e1*e1	-0.296399 *		-0.55	0.6126	1.0000	
H1*e3	-0.067743 *		-0.13	0.9088	1.0000	
e1*e3	-0.587901 *		-1.10	0.2520	0.9866	
e3*e3	-0.230982 *		-0.43	0.6952	1.0000	
H1*K1	0.557832 *		1.04	0.2760	0.9940	
e1*K1	-0.031428 *		-0.06	0.9574	1.0000	

Figure 4.7. DSD – RCS Results

The same deductions is carried out for the RCS and the results show that the most important factor is H1. The result makes sense that the RCS is driven by the height of the middle station since it decides number of the bounces the waves make.

#### 4.2.4 DSD Overview

Considering the results and deductions made for performance outputs, in summary L1, K1, e1, e2 and H1 are the most important factors leaving out K2, L2 and e3 factors. Following deductions are listed for the remaining factors.

- K2 factor which is the saddle of the second duct part spline was expected to be important for the DC output but turned out to be less important according to DSD. It is still the 4<sup>th</sup> important factor in main effects and also L1\*K2 and e1\*K2 two-factor interactions are considerably important. Also considering the expectation of the saddle point being effective on DC output, K2 factor is decided to be included in the following DOE study.
- L2 factor which is the axial length of the duct was expected to be important for both the DC and RCS outputs but turned out to be less important according to DSD. L2 main effect and K1\*L2 interaction turned out to be considerable important for the PR output. The duct length is crucial in the actual design and limitations process, so the factor L2 is decided to be included in the following DOE study.
- e3 factor which is the 3<sup>rd</sup> ellipticity parameter of the middle section is the 3<sup>rd</sup> important factor in main effects for both PR and RCS and also several two factor interactions. So the factor e3 is decided to be included in the following DOE design points.

With all the deductions made, all of the factors are decided to be included in the DOE design point generation process.

#### 4.3 DOE Study

After fixing the variables to be used in the optimization process, the DOE study with the method explained in 2.2.1 is carried out for the generation of the design points to be used in the RSM model generation. The factors are taken again as continuous

values at three levels (-1, 0, 1) given in the design space. With the main effects, interaction effects and quadratics terms considered, JMP creates 51 design points. 2 out of the 51 design points are the baseline designs (with one of them a duplicate created by default) making a total of 49 design points. The design point along with the performance outputs is given in Table 4.6.

Table 4.6. DOE – Design Details and Results

Design #	Factors								Responses		
	L1	L2	K1	K2	H1	e1	e2	e3	PR	DC	RCS [dBm <sup>2</sup> ]
1	-1	1	1	1	-1	1	1	-1	0.9268	0.6931	-6.4
2	1	-1	1	1	1	-1	1	-1	0.9356	0.7686	-9.3
3	1	0	-1	-1	0	-1	1	0	0.9399	0.5577	-9.9
4	1	0	1	-1	-1	1	0	0	0.9402	0.5137	-9.9
5	1	1	-1	1	-1	1	1	1	0.9128	0.2179	-7.0
6	1	0	1	1	-1	0	-1	-1	0.9518	0.8021	-9.4
7	1	-1	-1	0	1	1	1	1	0.9245	0.3812	-10.0
8	1	-1	-1	-1	-1	0	0	1	0.9368	0.3419	-10.6
9	0	0	-1	-1	1	1	-1	1	0.8654	0.7697	-10.6
10	-1	0	-1	0	-1	1	0	0	0.8553	0.8113	-7.4
11	1	1	1	1	0	-1	0	0	0.9424	0.8579	-7.1
12	-1	-1	0	-1	-1	0	-1	-1	0.9482	0.9200	-7.4
13	1	0	-1	1	1	-1	-1	1	0.9500	0.7689	-11.7
14	-1	0	1	-1	0	-1	0	-1	0.8796	1.1646	-9.7
15	1	0	0	1	1	1	1	-1	0.9338	0.5023	-9.8
16	-1	-1	0	-1	1	-1	0	1	0.8850	0.9388	-8.7
17	1	-1	0	1	-1	0	1	0	0.9445	0.4385	-9.0
18	-1	1	-1	1	1	1	-1	-1	0.8185	0.8645	-8.2
19	1	1	0	0	-1	-1	1	-1	0.9331	0.6805	-7.2
20	0	-1	0	1	0	1	0	-1	0.9345	0.6840	-8.6
21	0	0	1	0	1	0	-1	0	0.9222	0.9544	-7.1

Table 4.6. DOE – Design Details and Results (continued)

<b>22</b>	1	1	-1	-1	-1	-1	-1	0	0.9391	0.7856	-8.0
<b>23</b>	0	-1	-1	0	0	-1	-1	0	0.9009	0.9485	-11.2
<b>24</b>	1	-1	-1	0	-1	1	-1	-1	0.9408	0.3424	-8.6
<b>25</b>	-1	-1	1	-1	1	1	1	-1	0.9432	0.8129	-14.9
<b>26</b>	-1	-1	1	-1	-1	1	1	1	0.9352	0.6870	-9.3
<b>27</b>	1	1	1	-1	1	0	1	1	0.9359	0.6808	-7.1
<b>28</b>	-1	1	1	-1	-1	-1	1	0	0.9117	0.9265	-7.7
<b>29</b>	0	1	-1	1	-1	0	-1	0	0.9185	0.7071	-8.4
<b>30</b>	-1	-1	-1	1	-1	1	-1	1	0.8435	0.8617	-6.6
<b>31</b>	-1	1	0	1	1	1	0	1	0.8575	0.7595	-7.8
<b>32</b>	-1	1	0	-1	0	1	1	0	0.8355	0.7298	-7.7
<b>33</b>	-1	1	1	-1	-1	1	-1	1	0.9302	0.7340	-7.1
<b>34</b>	0	1	-1	-1	1	-1	0	-1	0.8731	0.8628	-11.5
<b>35</b>	1	1	-1	0	0	0	0	-1	0.9237	0.5418	-7.3
<b>36</b>	-1	1	-1	0	0	-1	-1	1	0.8421	0.9368	-7.4
<b>37</b>	-1	-1	1	1	-1	-1	-1	0	0.8996	1.1433	-10.6
<b>38</b>	1	-1	1	1	1	1	-1	1	0.9538	0.6255	-10.0
<b>39</b>	0	-1	-1	-1	-1	1	1	-1	0.8618	0.7183	-7.8
<b>40</b>	-1	1	0	1	1	-1	-1	-1	0.8602	1.0542	-9.3
<b>41</b>	0	0	0	0	-1	-1	0	1	0.9454	0.8256	-7.1
<b>42</b>	-1	0	-1	1	-1	-1	0	-1	0.8600	0.9660	-10.2
<b>43</b>	0	1	-1	1	1	-1	1	0	0.8573	0.6226	-9.9
<b>44</b>	1	-1	1	-1	0	-1	-1	1	0.9192	0.9307	-7.8
<b>45</b>	1	-1	0	-1	1	0	-1	-1	0.9552	0.7578	-13.0
<b>46</b>	0	0	1	1	0	0	1	1	0.9436	0.7789	-9.1
<b>47</b>	1	1	1	-1	1	1	-1	-1	0.9353	0.7107	-10.3
<b>48</b>	1	1	0	0	0	1	-1	1	0.9285	0.4025	-10.7
<b>49</b>	-1	-1	-1	1	1	0	1	-1	0.8010	0.8197	-8.9

The PR values range from 0.8010 to 0.9552, the DC from 0.2179 to 1.1646 and the RCS from -6.4 to -14.8 dBm<sup>2</sup>. The obtained DOE results are to be used for the RSM model generation but these results can still be used for the identification of factors. The identification is done by comparing these to the DSD results as the DOE design point set is larger. The overview and the comments on the results are given in the next sections.

### 4.3.1 DOE - Investigation

The investigation is done by comparing the most effective factors found by the DOE and the DSD studies. The comparison for the responses are done by examining the p-values below the threshold of 0.1 and explained respectively. For the PR response, DOE study output is shown in Figure 4.8.

Screening for PR						
Contrasts						
Term	Contrast			Lenth t-Ratio	Individual p-Value	Simultaneous p-Value
L1	0.025027			7.96	<.0001*	0.0002*
K1	0.018346			5.83	<.0001*	0.0011*
L1*K1	-0.012975 *			-4.13	0.0008*	0.0293*
H1	-0.009535			-3.03	0.0083*	0.2143
K1*e1	0.008234 *			2.62	0.0174*	0.4089
K1*e2	0.006034 *			1.92	0.0612	0.8772
L1*H1	0.005598 *			1.78	0.0797	0.9416

Figure 4.8. DOE – PR Results

The results show that L1, K1, H1, e1 and e2 are the most effective factors for PR. The DSD study results estimated the L1 and K1 factors to be the most effective, so the DOE study is consistent on the effectiveness of these factors and adds H1, e1, e2. For the DC response, DOE study output is shown in Figure 4.9.

Screening for DC						
Contrasts						
Term	Contrast		Lenth	Individual	Simultaneous	
			t-Ratio	p-Value	p-Value	
L1	-0.122324		-11.75	<.0001*	<.0001*	
e1	-0.103733		-9.96	<.0001*	<.0001*	
e2	-0.057687		-5.54	0.0002*	0.0018*	
K1	0.055370		5.32	0.0003*	0.0029*	
L1*K1	0.032711 *		3.14	0.0062*	0.1791	
H1	0.029475		2.83	0.0114*	0.3039	
e3	-0.027592		-2.65	0.0152*	0.4035	
e1*K1	-0.025148 *		-2.42	0.0223*	0.5258	
L1*e1	-0.021604 *		-2.07	0.0443*	0.7780	
e1*H1	0.020634 *		1.98	0.0533	0.8399	
L1*L1	-0.019808 *		-1.90	0.0619	0.8846	
L2*L2	-0.017354 *		-1.67	0.0982	0.9705	

Figure 4.9. DOE – DC Results

The results show that L1, e1, e2, K1, H1, e3 and L2 are the most effective factors for DC respectively leaving out the K2 factor. With the factors mentioned, the DC response is the most affected response by the factors. The DSD study results estimated the L1, e1 and e2 factors to be the most effective, so the DOE study is consistent on the effectiveness of these factors and adds K1, H1, e3 and L2. For the RCS response, DOE study output is shown in Figure 4.10.

Screening for RCS						
Contrasts						
Term	Contrast		Lenth	Individual	Simultaneous	
			t-Ratio	p-Value	p-Value	
H1	-0.684382		-2.99	0.0069*	0.2369	
L2	0.596697		2.60	0.0148*	0.4238	
K1*e1	-0.433283 *		-1.89	0.0666	0.8939	
H1*K1	0.411281 *		1.79	0.0794	0.9341	
K2*e1	0.404807 *		1.77	0.0842	0.9446	

Figure 4.10. DOE – RCS Results

The results show that H1, K1, e1 and K2 are the most effective factors for the RCS. The DSD study estimated that only the H1 factor is effective and with the DOE study finding H1 the most effective, the result can be evaluated as successful.

### **4.3.2 DOE - Overview**

The results of the DOE study and the comparison of them to the DSD study is evaluated in this section. The comparison of all responses reveals that the DSD study managed to capture the most effective factors for all responses but fails to estimate the less effective ones. The studies agree on the factors especially well for factors with p-values smaller than 0.01 which way smaller than 0.1 threshold. Comparing the 17 design point count of DSD to the 50 designs of the DOE, the identification of the factors is done taking 1/3 of time the DOE requires, also with mentioned deductions in mind, the DSD study is decided to be successful. Several deductions and estimations made for the outcomes of the responses are listed below.

- For the PR, the first duct part and the middle station parameters are more important. The investigation made for the DSD study is eligible that the first duct curvature and the profile shape are effective for the PR.
- For the DC, nearly all parameters are important. This makes sense since the distortion of the flow may get affected by the shape of all of the parts of the duct surfaces driven by all of the parameters.
- For the RCS, parameters deciding the shape of the ducts (saddle points) and the middle station parameters are important. The RCS output should be result of waves bouncing off of surfaces, so the parameters that may affect the number of bounces should be important. The results confirm the estimated outcomes.

With the investigation and overview of the DOE results are carried out, the obtained DOE design points are used for the model generation with RSM in the following section.

## **4.4 Surrogate Model Generation**

For the surrogate model, the Kriging method explained in 2.2.3 is carried out. The model generation is done with the HEEDS MDO by supplying the 50 design points

to the generation tool. The surrogate model features three functions for three performance outputs and the fitting of these function are done automatically by the tool with changing shape factors. Also mentioned Gaussian surface approximation decides the smoothness and the shape of the model.

Generation of the model is done within minutes and the results contain the design point actual values, the model prediction values and the cross-validation results. As was mentioned in 2.2.2, the model actual versus predicted values are exact, showing the model has perfect fit for all three functions. The representation of the actual versus predicted values for the performance outputs is shown in Figure 4.11, Figure 4.12 and Figure 4.13. The graphs show the perfect fit at all design points.

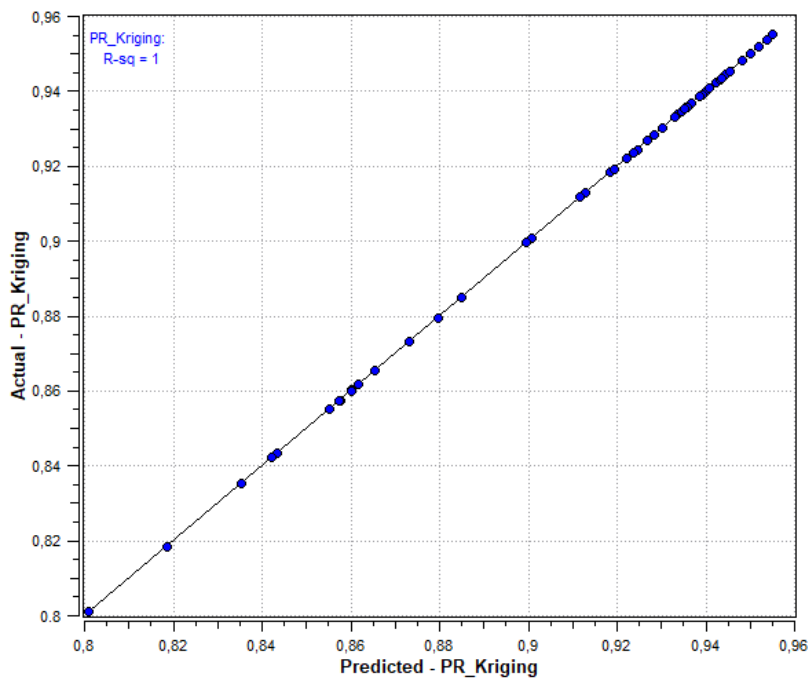


Figure 4.11. Surrogate Model PR Output

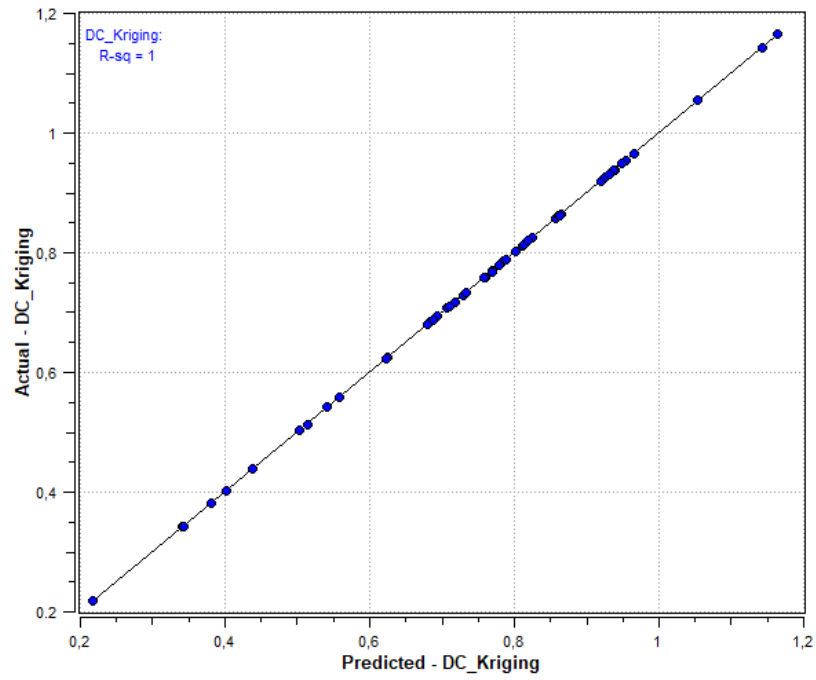


Figure 4.12. Surrogate Model DC Output

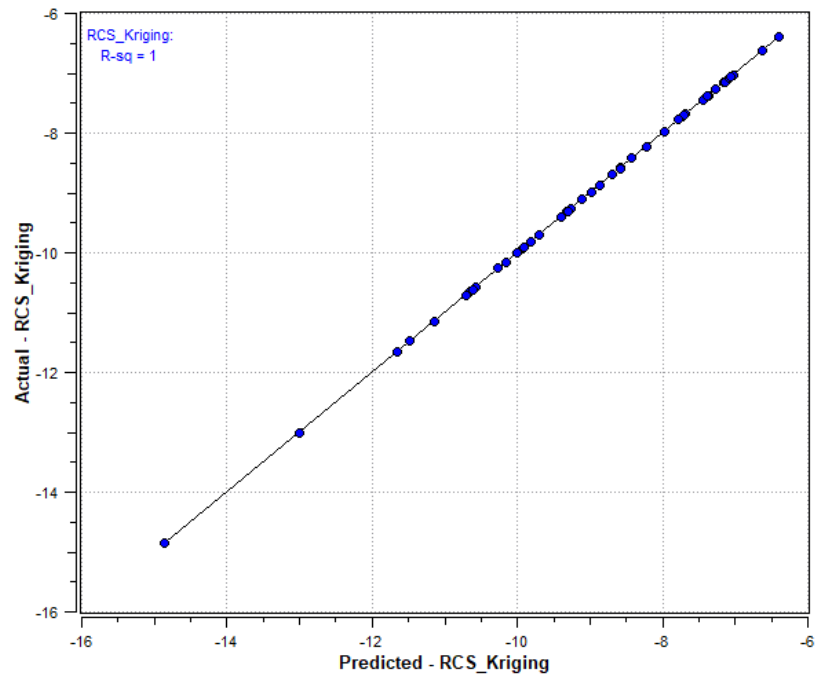


Figure 4.13. Surrogate Model RCS Output

Considering the mentioned perfect fit of values at design points, the validation of the model will be investigated only through the cross-validation results. Cross-validation

results are evaluated with the leave-one-out approach (also called PRESS), so each design point is subtracted from the design set and the performance output is recalculated revealing the residual of the difference that design point causes. The maximum residual caused by all design points show the maximum expected residual from the actual values for any design point. The results for the three performance parameters are given in Table 4.7.

Table 4.7. Surrogate Model Performance Outputs

<b>Performance Output</b>	<b>Method</b>	<b>Shape Factor</b>	<b>Cross-validation Residual</b>
PR	Kriging with Gaussian Approximation	0.623	0.0276
DC	Kriging with Gaussian Approximation	0.454	0.0844
RCS	Kriging with Gaussian Approximation	0.454	1.63

The cross-validation results are in terms of residual, so instead of evaluating the residual values solely by the numbers, the residuals are compared to the average of actual design point outputs in terms of percentile. The comparison is given in Table 4.8.

Table 4.8 Surrogate Model Cross-Validation Results

	<b>PR</b>	<b>DC</b>	<b>RCS [dBm<sup>2</sup>]</b>
<b>Average of DOE Design Points</b>	0.9088	0.7409	-8.9
<b>Cross-Validation Residual</b>	0.0276	0.0844	1.63
<b>Percentage of Residual to the Average</b>	3.0	11.4	18.2

The comparison shows that the PR prediction is below 5%, the DC prediction is around 10% and the RCS prediction is below %20. The comparison is done with respect to average actual values, so it may not be counted as an accurate comparison as the average values are used. But using the maximum or minimum values would also be misleading in terms of percentile difference. Considering that the percentages given represents the maximum expected residuals, the results are counted sufficient for use as the surrogate model. Still in the optimization process, the expected performance outputs will be evaluated with the cross-validation results in mind. Optimization process which uses the surrogate model is detailed in the following sections.

## **4.5 Optimization**

### **4.5.1 Optimization Results**

The optimization is carried out with the method explained in 2.2.3. The multi-objective optimization driven by the surrogate model containing three functions is handled with the HEEDS MDO method called SHERPA. The optimization is done with a single block of process thanks to the surrogate model, meaning that the processing unit gives out the needed performance outputs given the input values in an instant. The optimization input variables are given in the Table 4.9.

Table 4.9 Design Optimization Input Limitations

		Minimum	Baseline	Maximum	Resolution
<b>First Duct Part</b>	<b>L1 [m]</b>	0.3375	0.375	0.45	101
	<b>H1 [m]</b>	0.26	0.28	0.30	101
	<b>k1</b>	0.4	0.5	0.6	101
<b>Second Duct Part</b>	<b>L2 [m]</b>	0.675	0.75	0.9	101
	<b>H2 [m]</b>	-	0.23	-	-
	<b>k2</b>	0.4	0.5	0.6	101
<b>Middle Station</b>	<b>e1 [mm]</b>	75	85	95	101
	<b>e2 [mm]</b>	50	60	70	101
	<b>e3 [mm]</b>	65	70	75	101

The optimization objectives and constraints are given in Table 4.10 and Table 4.11 respectively.

Table 4.10 Design Optimization Objectives

Performance Output	Objective
PR	Maximize
DC	Minimize
RCS	Minimize

Table 4.11 Design Optimization Constraints

Performance Output	Constraints
DC	$DC_i < 0.6$

The optimization variable resolution is set to 101 making the design space consisting of  $10^{16}$  design points for 8 variables. The number of evaluation for this design space is set to 4000 designs with an option to increase in case the convergence is not

ensured. The optimization performance calculation is decided as is mentioned in 2.2.3.

With the optimization details set, the optimization is carried out. The convergence check is done quantitatively by comparing the 20 highest performing designs and visually by comparing the designs with highest performing 5% design variables. Performance outputs of the 20 highest performing designs are given in Table 4.12. Performance outputs' difference from the highest performing design in percentile is also given in the results.

Table 4.12 Design Optimization Performance Output Results

Design Number	Performance Outputs					
	PR	PR % Difference	DC	DC % Difference	RCS [dBm <sup>2</sup> ]	RCS % Difference
313	0.9376	-	0.3113	-	-10.4906	-
298	0.9377	-0.003	0.3123	-0.313	-10.4990	-0.080
328	0.9376	0.003	0.3101	0.396	-10.4797	0.104
342	0.9376	0.001	0.3111	0.082	-10.4881	0.024
385	0.9372	0.044	0.3098	0.497	-10.4951	-0.042
357	0.9373	0.041	0.3107	0.184	-10.5035	-0.123
455	0.9372	0.047	0.3085	0.892	-10.4840	0.063
329	0.9372	0.044	0.3095	0.579	-10.4925	-0.017
441	0.9380	-0.044	0.3129	-0.519	-10.4855	0.049
469	0.9380	-0.040	0.3117	-0.122	-10.4747	0.152
434	0.9377	-0.003	0.3126	-0.415	-10.5009	-0.098
414	0.9381	-0.046	0.3139	-0.833	-10.4939	-0.031
484	0.9380	-0.043	0.3127	-0.436	-10.4830	0.072
796	0.9377	-0.006	0.3136	-0.729	-10.5094	-0.179
746	0.9376	0.003	0.3104	0.292	-10.4815	0.087
592	0.9374	0.020	0.3120	-0.236	-10.5060	-0.146
659	0.9373	0.040	0.3111	0.083	-10.5055	-0.142
2316	0.9376	0.006	0.3092	0.688	-10.4706	0.191
2676	0.9373	0.038	0.3120	-0.230	-10.5140	-0.222
511	0.9375	0.017	0.3130	-0.550	-10.5144	-0.227

The differences of the design performance outputs from the highest performing one show that all of them under 1% difference, so the convergence of the optimization is decided to be ensured. Variables of the same 20 highest performing designs are given in Table 4.13.

Table 4.13 Design Optimization Variable Results

Evaluation Number	First Duct Part Variables			Second Duct Part Variables		Middle Station Variables		
	L1	H1	K1	L2	K2	e1	e2	e3
313	0.45	0.26	0.408	0.675	0.4	88.0	61.6	75.0
298	0.45	0.26	0.408	0.675	0.4	88.0	61.4	75.0
328	0.45	0.26	0.408	0.675	0.4	88.2	61.6	75.0
342	0.45	0.26	0.408	0.675	0.4	88.2	61.4	75.0
385	0.45	0.26	0.406	0.675	0.4	88.0	61.6	75.0
357	0.45	0.26	0.406	0.675	0.4	88.0	61.4	75.0
455	0.45	0.26	0.406	0.675	0.4	88.2	61.6	75.0
329	0.45	0.26	0.406	0.675	0.4	88.2	61.4	75.0
441	0.45	0.26	0.410	0.675	0.4	88.0	61.6	75.0
469	0.45	0.26	0.410	0.675	0.4	88.2	61.6	75.0
434	0.45	0.26	0.408	0.675	0.4	87.8	61.6	75.0
414	0.45	0.26	0.410	0.675	0.4	88.0	61.4	75.0
484	0.45	0.26	0.410	0.675	0.4	88.2	61.4	75.0
796	0.45	0.26	0.408	0.675	0.4	87.8	61.4	75.0
746	0.45	0.26	0.408	0.675	0.4	88.0	61.8	75.0
592	0.45	0.26	0.408	0.675	0.4	88.0	61.6	75.0
659	0.45	0.26	0.406	0.675	0.4	87.8	61.6	75.0
2316	0.45	0.26	0.408	0.675	0.4	88.2	61.8	75.0
2676	0.45	0.26	0.406	0.675	0.4	87.8	61.4	75.0
511	0.45	0.26	0.408	0.675	0.4	88.0	61.4	75.0

The HEEDS outputs for the highest performing 1% designs per performance outputs are given in Figure 4.14, Figure 4.15 and Figure 4.16. The results contain designs with performance similar to the Design 313 with a maximum of 1% difference. The discussion of the outputs will be discussed in the following section.

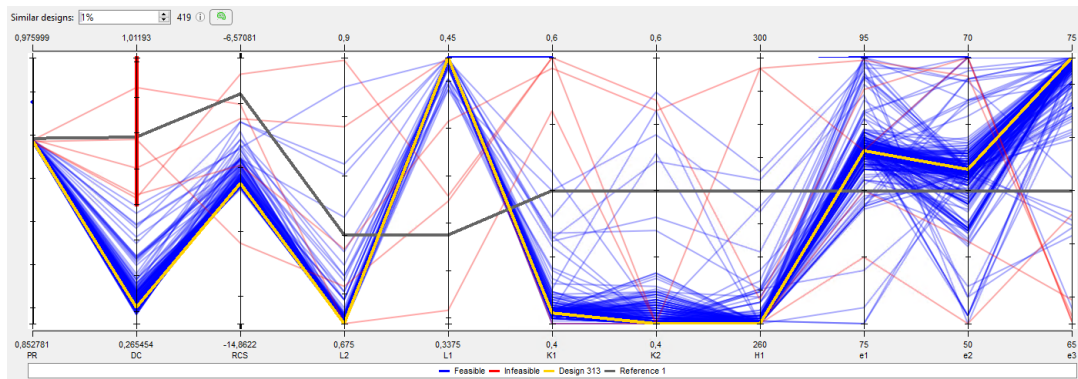


Figure 4.14. Design Optimization PR Investigation

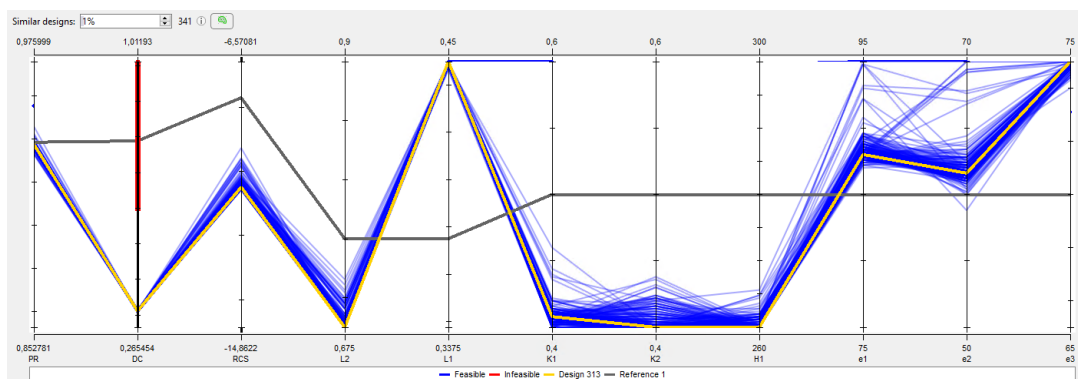


Figure 4.15. Design Optimization DC Investigation

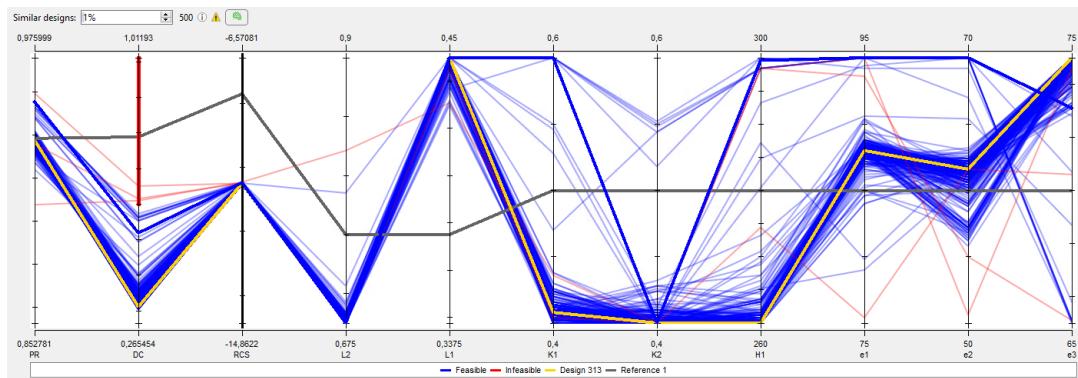


Figure 4.16. Design Optimization RCS Investigation

The highest performing design is Design 313, and its variables and performance outputs is given in Table 4.14 and Table 4.15.

Table 4.14 Design Optimization Best Performing Design Comparison

		Minimum	Baseline	Maximum	Design 313
<b>First Duct Part</b>	<b>L1 [m]</b>	0.3375	0.375	0.45	0.45
	<b>H1 [m]</b>	0.26	0.28	0.30	0.26
	<b>k1</b>	0.4	0.5	0.6	0.408
<b>Second Duct Part</b>	<b>L2 [m]</b>	0.675	0.75	0.9	0.675
	<b>H2 [m]</b>	-	0.23	-	0.23
	<b>k2</b>	0.4	0.5	0.6	0.4
<b>Middle Station</b>	<b>e1 [mm]</b>	75	85	95	88
	<b>e2 [mm]</b>	50	60	70	61.6
	<b>e3 [mm]</b>	65	70	75	75

Table 4.15 Best Design Performance Outputs

<b>Design 313 - Performance Outputs</b>		
<b>PR</b>	<b>DC</b>	<b>RCS [dBm<sup>2</sup>]</b>
0.9376	0.3113	-10.4906

The optimized intake model images is given in Figure 4.17 as isometric view, Figure 4.18 as side view with dimensions and Figure 4.19 as middle profile with dimensions.

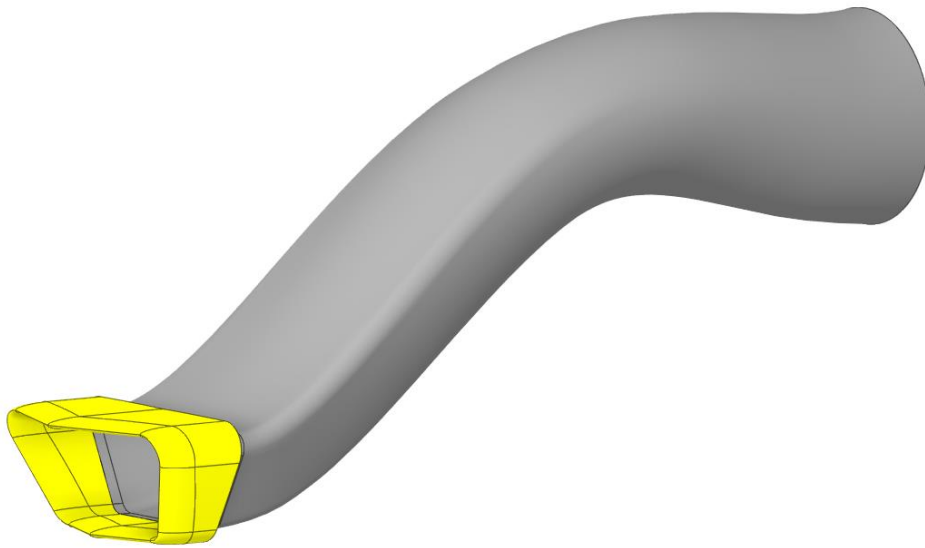


Figure 4.17. Optimized Intake Duct Isometric View

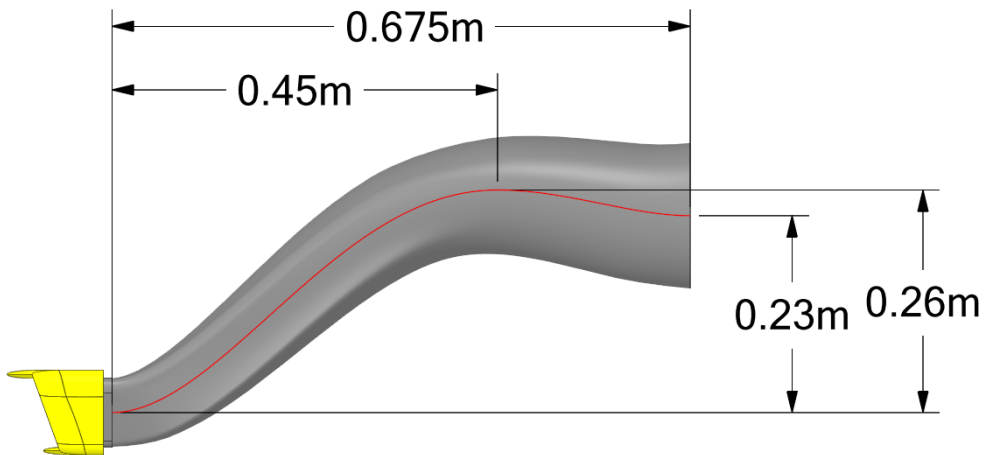


Figure 4.18. Optimized Intake Duct Dimensions

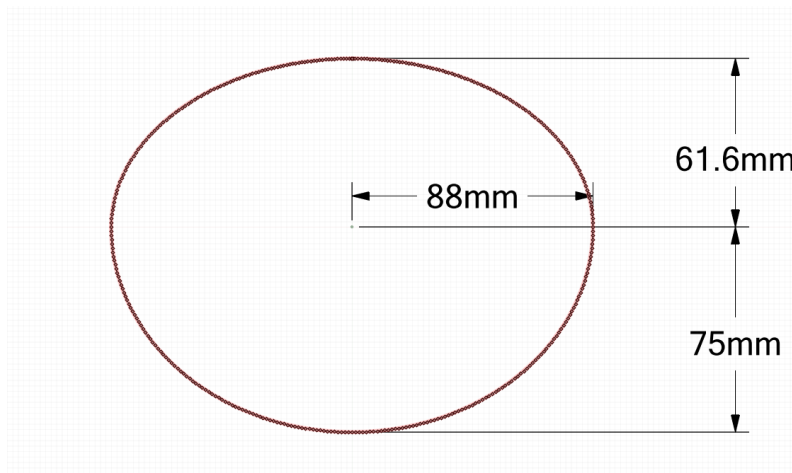


Figure 4.19. Optimized Intake Duct Middle Station Dimensions

The discussion on the obtained results is shared in the following section.

#### 4.5.2 Optimization Discussion

The results given in Table 4.12 and Table 4.13 show that the 20 highest performing designs share similar variable values. The outcomes for the variables are listed below.

- The variables of the 20 highest performing designs are in the close proximity of each other with only  $K1$ ,  $e1$  and  $e2$  parameters differentiating slightly. Considering this result with the mentioned performance outputs, the optimization is assumed converged.
- The images given in Figure 4.14, Figure 4.15 and Figure 4.16 show the designs with a maximum performance difference of 1% for each performance output. The images show the designs' variables and the performance outputs in the lower and upper bars. The feasible designs are indicated with blue lines, best design in yellow line, infeasible designs driven by the DC limit in red lines and the baseline design in grey line. According to the results, for PR, 419 designs out of 4000 designs have PR outputs with a maximum 1%

difference. Likewise for DC, 341 designs and for RCS more than 500 designs are within this limit separately. The images show that the optimization algorithm searched for designs both near the highest performing design and far from it to avoid local peaks. Also it is deduced that high PR and high RCS performance can be achieved with several different variable configurations. But the DC performance is limited to a more confined design space.

- L1, H1, L2, K2 and e3 parameters are limited by either lower or upper bounds of the optimization. L1 and e3 are limited by the upper bounds meaning the optimization opted for longer first duct length and longer downward middle station parameter. H1, L2 and K2 parameters are limited by the lower bounds, so the optimization opted for lower middle station height, lower second duct length and smaller second duct saddle point location. Also the first duct saddle point location is relatively close to the lower bound.
- The middle station profile parameters, e1 and e2, are near the baseline values, leading to a more elliptical profile than a circular one.
- The intended RCS reducing design consists of a high curvature surface in the first duct part and a smoother surface in the second part due to the placement of the middle station and duct lengths. The results show that the optimization tried to make the first duct part less curved by with longer first duct length and lower middle station height. Being naturally less curved, the second duct length is minimized. This is opposite to the expectation that the second duct could straighten the flow more with a longer duct so helping DC, but the deduced outcome is that the lower middle station height allowed the second duct be straight enough for a smoother flow. With the outcomes on the optimization results shared, obtained Design 313 is selected as the best design and used as the validation case of optimization in the following section.



## CHAPTER 5

### VALIDATION AND DISCUSSION OF THE RESULTS

In this chapter the validation and the discussion of the best design decided by the optimization is explained. Validation study and the discussion of the best design are presented in the following sections.

#### 5.1 Validation Results of the Optimized Intake

The validation of the optimized intake is carried out with the analysis methods explained in 2.3 and 2.4. The CFD and RCS analyses are carried out with the conditions given in 4.1 which is the same carried out for the DOE study. The analysis performance output results with comparison to the optimization results is given in Table 5.1.

Table 5.1 Validation Results and Comparison

	Design 313 - Performance Outputs		
	PR	DC	RCS
<b>Optimization Results</b>	0.9376	0.3113	-10.4906
<b>Validation Results</b>	0.9339	0.3325	-10.6100
<b>Difference</b>	0.0037	-0.0212	0.2084
<b>Difference [%]</b>	-0.39	6.37	1.95

Several post-process images are obtained for the CFD and RCS analyses for the discussion of optimization results. Deductions are made for all post-process outputs with the overall discussion made in the following section. For the CFD analysis, Mach, static pressure, total pressure and PR images are obtained revealing

importing insights for the optimized design. For the RCS analysis, “Visual Ray Tracing” (VRT) images on a single plane wave is investigated.

### 5.1.1 CFD Post-Process Outputs

Mach contour of the flow field at the symmetry plane is given in Figure 5.1. Given contour shows that normal shocks occur at the outer parts of the upper and lower lip sections and after the throat section where the duct surface curves outward. Given the flight speed of 0.9 Mach, the shocks occurring at the outer lip sections regarded normal and non-effective for intake duct performance, but the shock formed after the throat section is undesirable and may affect the performance. The occurring shock is deemed the result of the high curvature surface that causes first the inwards speeding flow and then the separation of the flow after the shock. Flow seem to separate on both duct parts where the flow advancing inwards. The flow separated in the first duct part reattaches due to the oppositely curved second duct part.

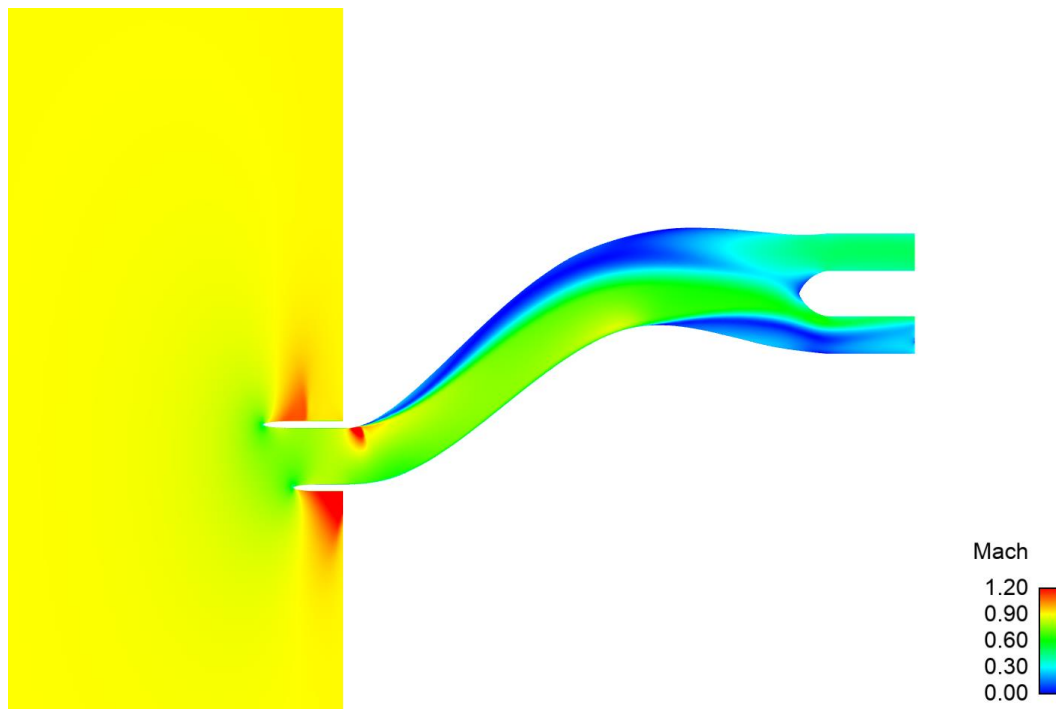


Figure 5.1. Mach Contour of the Validation Case

Mach contours at the throat station, middle station and the AIP station is given in Figure 5.2 with half of the duct surfaces. The contour supports the previous Mach contour of the flow field and reveals that the flow separation seen on the upper first and lower second duct is limited in a smaller area. Also separation starting on the lowest part of the middle station is visible.

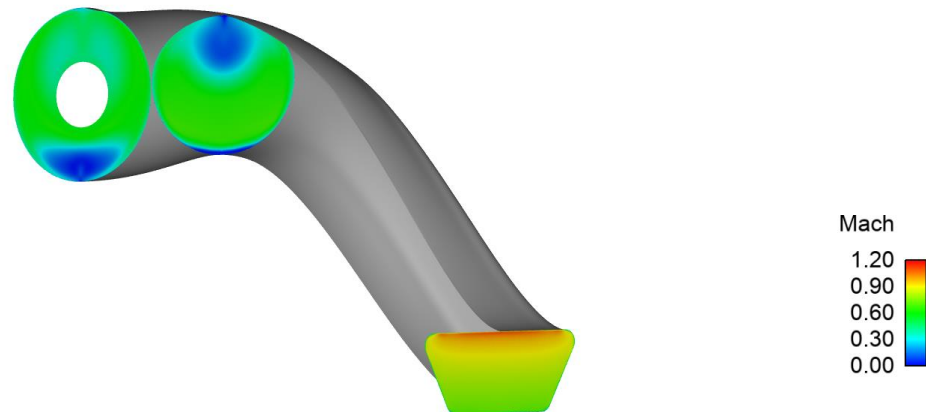


Figure 5.2. Mach Contours of the Main Stations

Further investigations on the separation zones are done by obtaining streamlines going through the duct. The streamline output is given in Figure 5.3 with the lines colored according to the Mach number. The streamlines show the formation of the separation zones with a swirling flow on the upper surface and a dead zone on the second duct part lower surface. The effect of the separations on the middle station and AIP station Mach profiles is shown with streamlines in Figure 5.4. Low speed zones caused by the swirling flow in the upper part and a relatively bigger swirl on the lower part and their effect on the stations are visible.

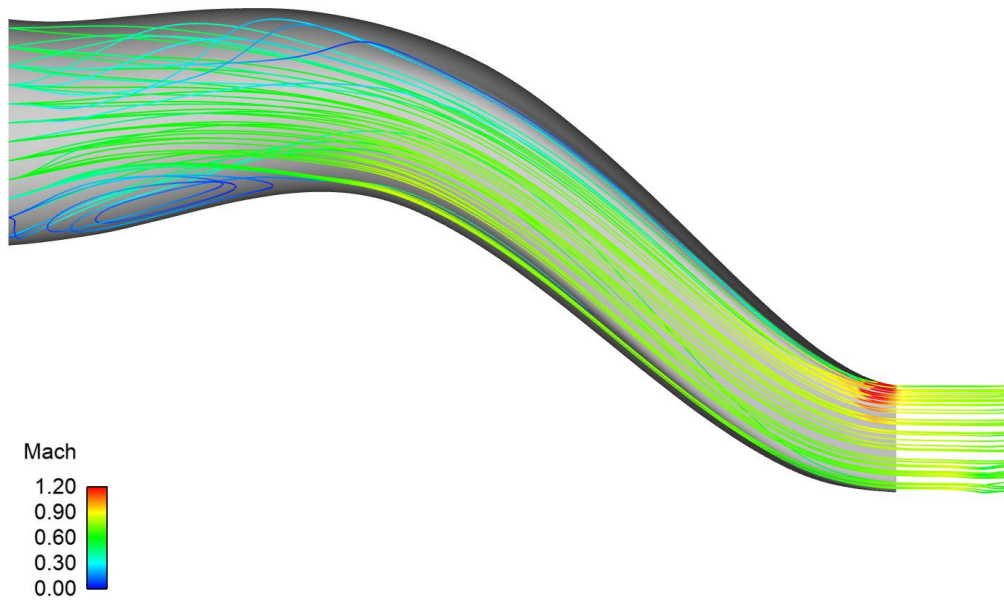


Figure 5.3. Mach Streamline Inside the Duct

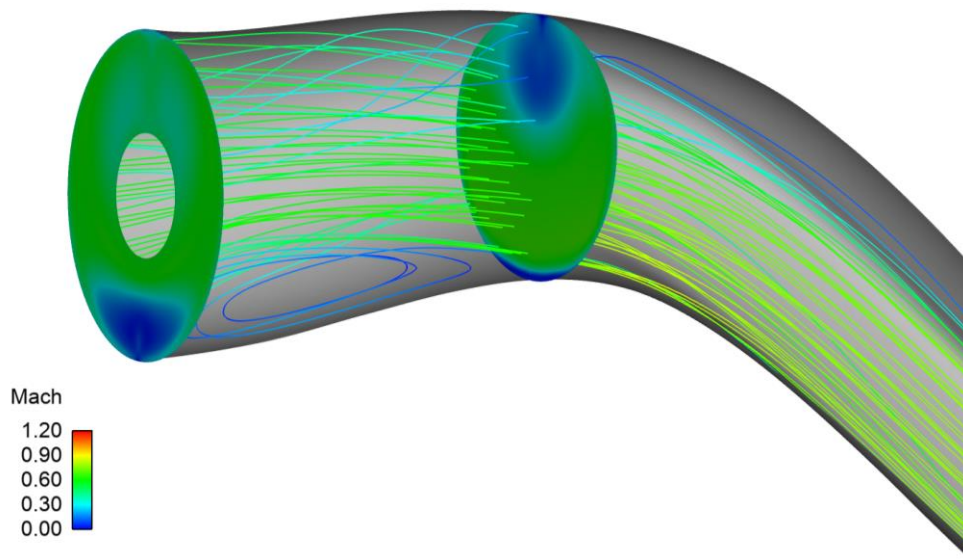


Figure 5.4. Mach Streamlines with Main Station Mach Contours

The obtained Mach contours and streamlines help understanding the behaviour of the flow inside the duct and the DC performance output. Total pressure and PR images are also obtained for the PR performance output evaluation.

The total pressure contour of the flow field at the symmetry plane is given in Figure 5.5. It can be seen that the flow field is dominated by the free stream total pressure value and how much of the quality air reaches inside the duct. The effect of the separation on the flow quality inside the duct is visible on this image and determining on the PR performance output.

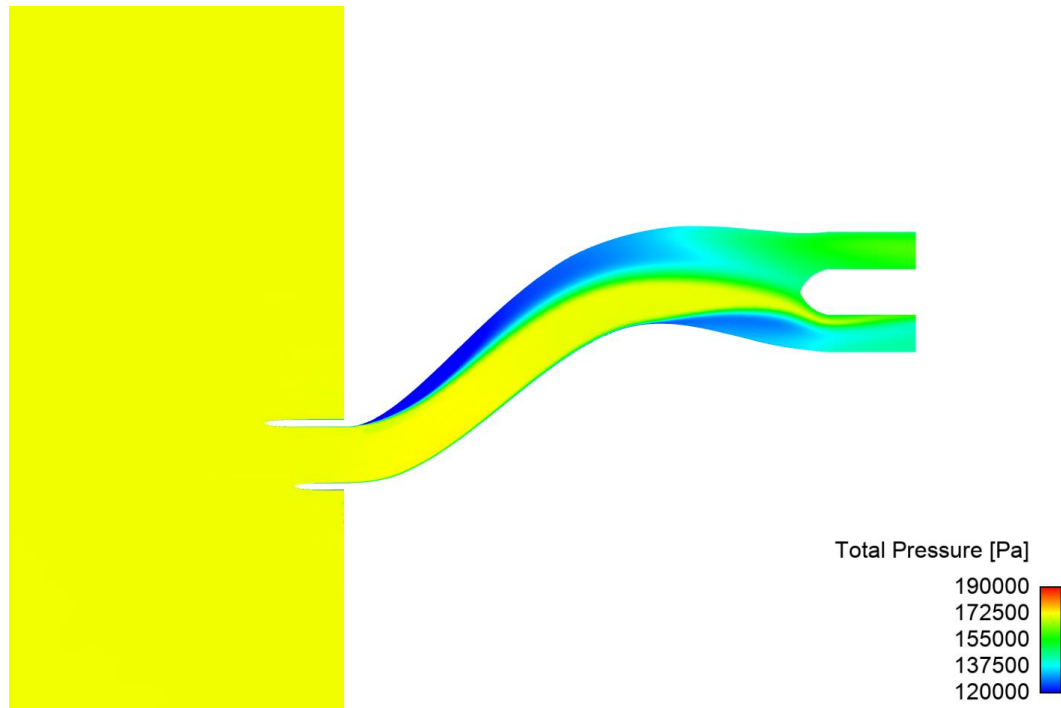


Figure 5.5. Flow Field Total Pressure Contour

A detailed investigation is carried out with PR contours on the main stations and the obtained images are given in Figure 5.6, Figure 5.7 and Figure 5.8. Figure 5.6 shows that the throat station is dominated by high quality flow as expected. Figure 5.7 shows that the middle station is affected by the separated flow off of the first duct part upper surface and the separation beginning on the lower surface is also visible. Figure 5.8 shows that the dead air zone and the vortex zone at the upper surface of the second duct part cause the PR deterioration at the AIP station.

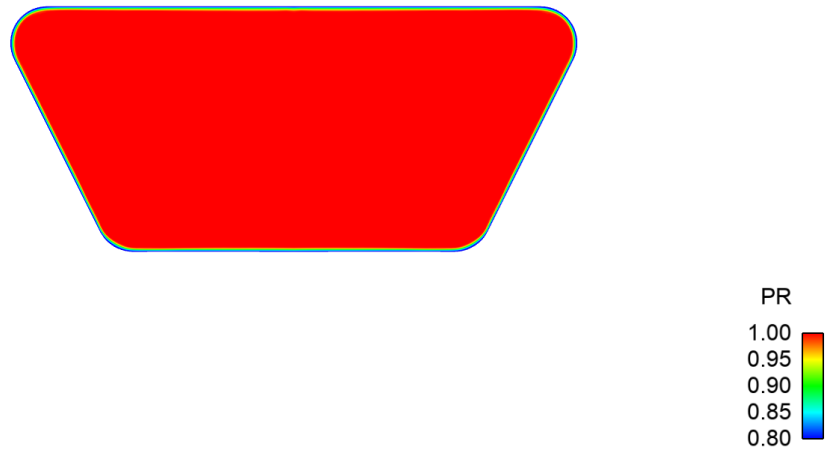


Figure 5.6. PR Contour at the Throat Station

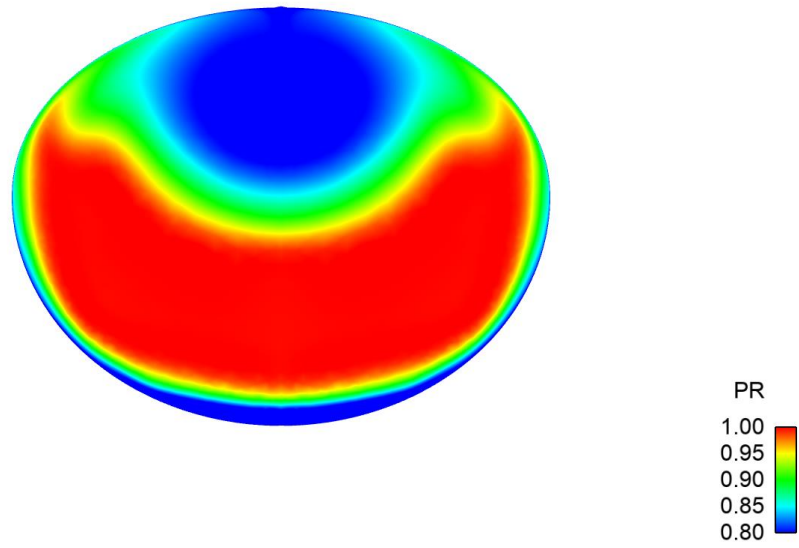


Figure 5.7. PR Contour at the Middle Station

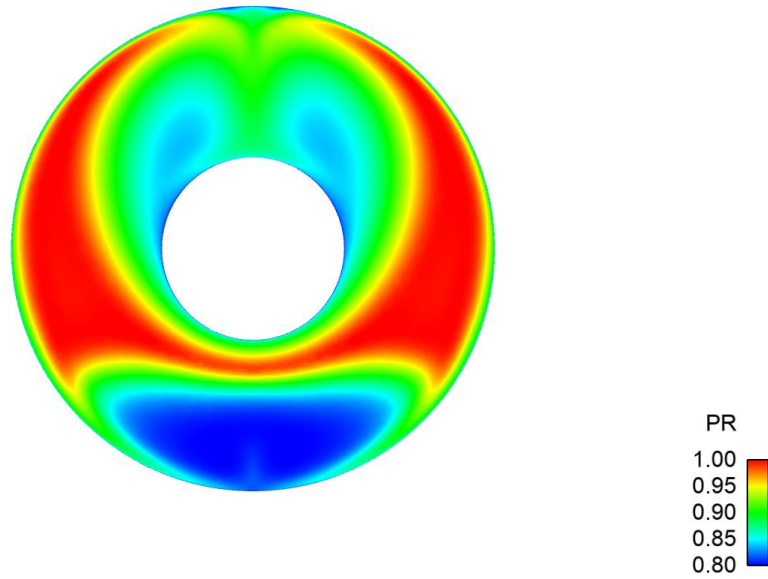


Figure 5.8. PR Contour at the AIP Station

Discussions on the RCS post-process results is given on the following sections.

### 5.1.2 RCS Post-Process Outputs

Several post-process images are obtained for the RCS analysis. As was mentioned in 2.4.3, a total of 305 RCS values is obtained at 61 azimuth angles over 5 elevation angles and the performance value is calculated with the modifying method. The non-modified RCS values is given in Figure 5.9 and it gives little information about the behaviour of the RCS data. It can be said that the majority of the data are gathered between the RCS values of -10 and -20 dBm<sup>2</sup>.

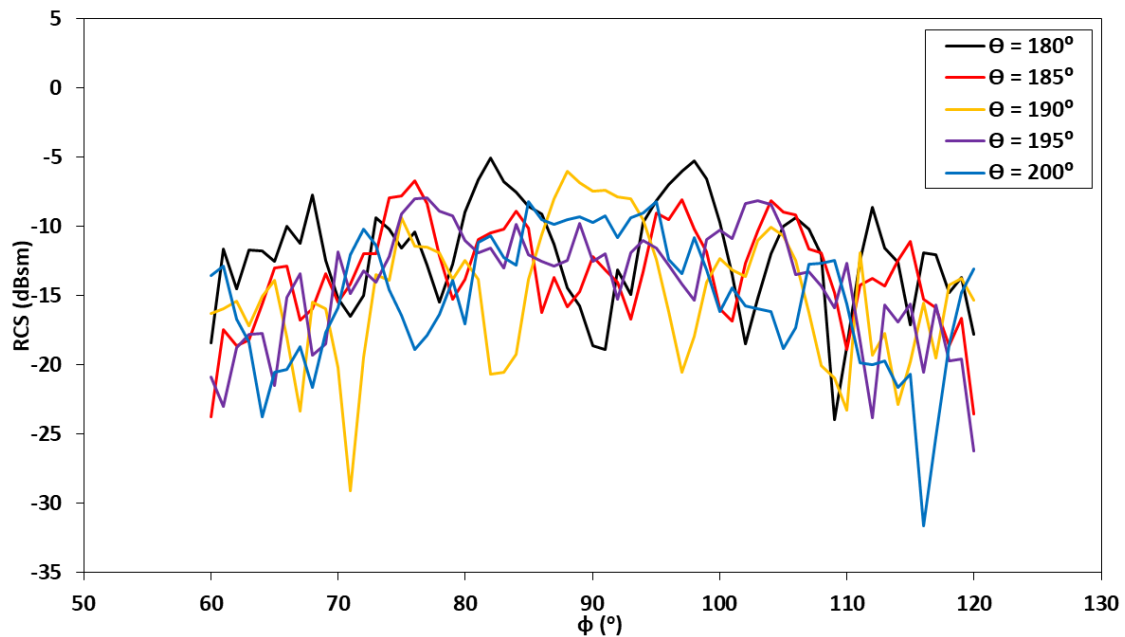


Figure 5.9. RCS Values of the Optimized Intake

Several non-modified RCS values have importance on the assessing of the data and they are listed below.

- The maximum value is  $-5.03 \text{ dBm}^2$  and it is at  $\phi=82^\circ$  and  $\theta=180^\circ$ .
- The minimum value is  $-31.61 \text{ dBm}^2$  and it is at  $\phi=116^\circ$  and  $\theta=200^\circ$ .
- At  $\phi=90^\circ$  and  $\theta=180^\circ$ , a relatively low RCS value of  $-18.62 \text{ dBm}^2$  is obtained.

Apart from the mentioned RCS values, an investigation is carried out using the VRT functionality of ANSYS HFSS which allows user to examine the waves acting on the model visually. The obtained VRT images is set up such that a single incident plane wave at  $\phi=90^\circ$  and  $\theta=180^\circ$  is launched at the model and the advancement of the waves is calculated using the ray tracing. The VRT images show the bounce locations of the waves according to the bouncing number of a wave. Obtained VRT images are given in Figure 5.10, Figure 5.11, Figure 5.12, Figure 5.13 and Figure 5.14 with green points designating waves bouncing once, blue points bouncing 2 times, yellow points bouncing 3 times, red points bouncing 4 or 5 times.

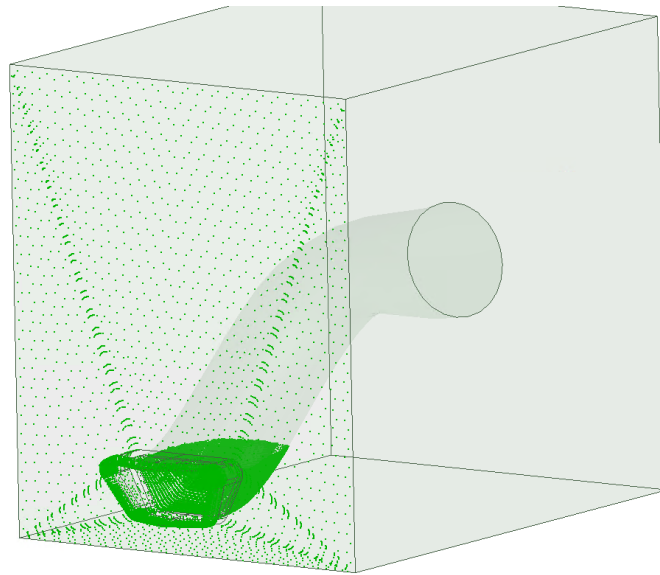


Figure 5.10. VTR Image of 1<sup>st</sup> Bounce

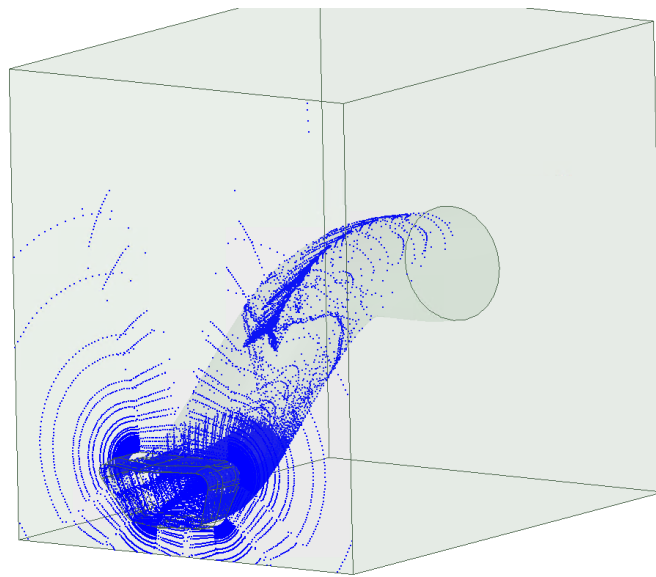


Figure 5.11. VTR Image of 2<sup>nd</sup> Bounce

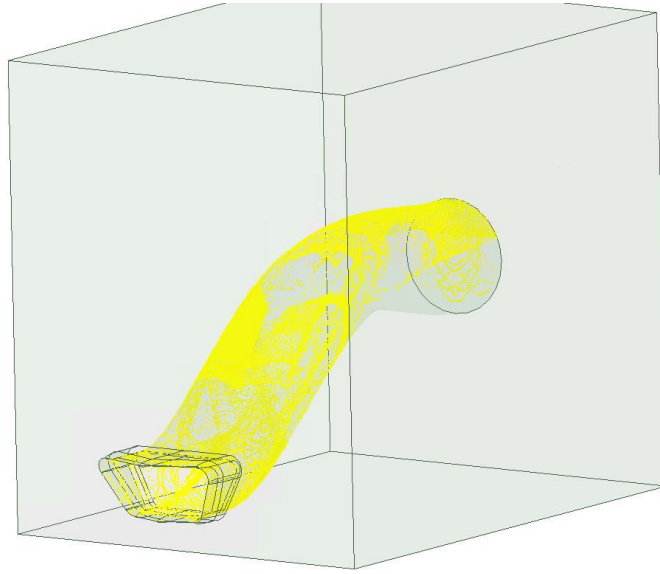


Figure 5.12. VTR Image of 3<sup>rd</sup> Bounce

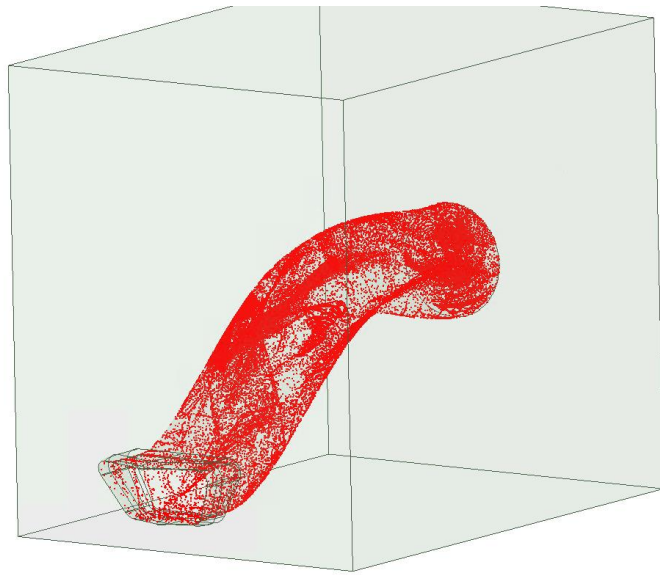


Figure 5.13. VTR Image of 4<sup>th</sup> Bounce

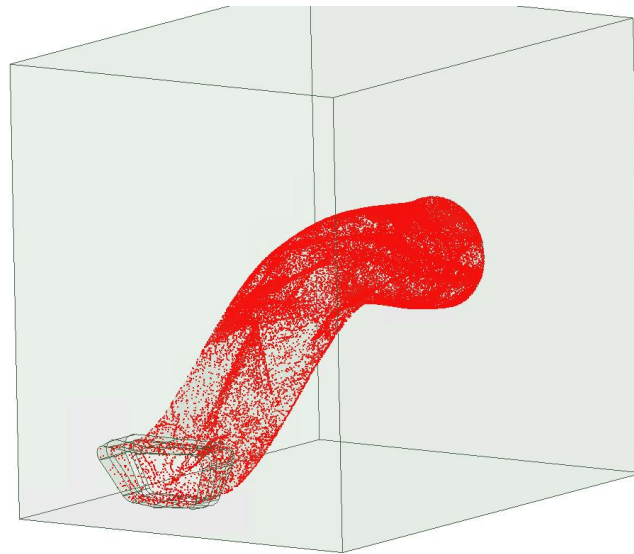


Figure 5.14. VTR Image of 5<sup>th</sup> Bounce

The VRT images show that as the bouncing count rises, the waves advance more into the duct. The lip and the entry of the duct encounter the first and second bounce and the duct surfaces encounter the rest of the bounce counts. With the waves bouncing 5 times, all of the model surfaces are illuminated, so the analysis setting of 8 maximum bounces is sufficient. The image given in Figure 5.15 shows the overall bouncing locations for all bouncing counts.

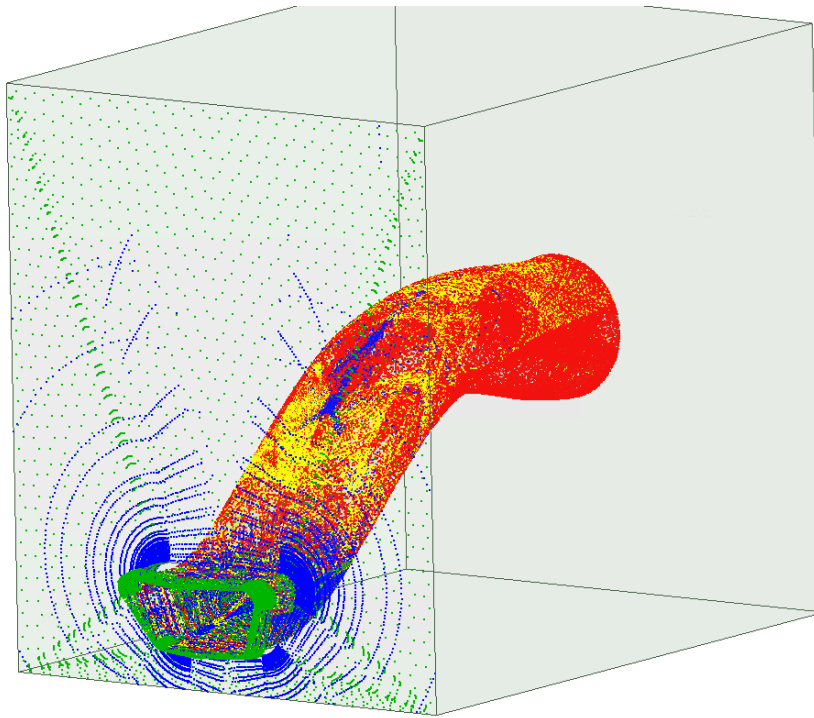


Figure 5.15. VTR Image of Bounces

## 5.2 Discussion of the Validation Results

The discussions on the best design and the optimization results are covered in this section. The performance outputs given in 5.1 show the difference of the optimization and validation results. The difference in percentile show that the difference of PR is under 1%, DC under 7% and the RCS under 2%, but the performance of the model must be evaluated with the cross-validation residual given in 4.4. The outputs of the results with the residuals is given in Table 5.2.

Table 5.2 Optimization and Validation Results Comparison

	<b>Design 313 - Performance Outputs</b>		
	<b>PR</b>	<b>DC</b>	<b>RCS</b>
<b>Optimization Results</b>	0.9376	0.3113	-10.4906
<b>Validation Results</b>	0.9339	0.3325	-10.6100
<b>Difference</b>	0.0037	-0.0212	0.2084
<b>Cross-Validation Residual</b>	0.0276	0.0844	1.63

The comparison of the difference between the optimization and validation results to the cross-validation residuals show that the difference is way below the residuals showing the model used in the optimization validated.

The aerodynamic performance coefficients PR and DC show that for a double curved duct, competitive aerodynamic coefficients can be achieved. Since the design and optimization of the concept is carried out with only the duct parameters, validation results showed that including the throat of the duct into optimization is also important. The shock forming just after the throat station is deemed caused by the throat design and the steep curve of the first duct part. The steep curve of the first duct part also cause a local separation zone affecting both the middle and the AIP stations. Since the steepness of this curve is driven by the platform limits, geometric limitations imposed by the platform and the engine is important. Although the imposed limits affect the performance, the separation of flows on the concept of double curved duct seems unavoidable.

The RCS results show that the intake system outputs values between -5 to -32 dBm<sup>2</sup> changing with the illumination angle. The plane wave with the highest importance was illumination angle  $\phi=180^\circ$  and  $\theta=90^\circ$  and its RCS value is -18.62 dBm<sup>2</sup>. The given value is equivalent to 0.014 m<sup>2</sup> which is close to the generalized bird RCS of 0.01 m<sup>2</sup> [47]. This result show that the intake system will not increase the overall

platform RCS for this illumination angle RCS value if the platform do not increase independently. Also the RCS value can be decreased up to  $0.001 \text{ m}^2$  by setting the platform orientation to the relevant illumination angle. Also the lip geometry should be included in the design and optimization process if RCS value is intended to be decreased.

## CHAPTER 6

### CONCLUSION AND FUTURE WORK

In this thesis, a design of a S-shaped subsonic intake with low radar signature is carried out with the design method proposed. Proposed double curved S-shaped intake features line of sight blockage of the engine compressor/fan face to lower the radar signature. To give background information on intakes and clarify the purpose the thesis, information on intakes, stealth applications and design methods are explained in the first part of the study.

The multi-objective and multi-disciplinary design problem is handled with surrogate-based analysis and optimization methodology to reduce the computationally expensive and time consuming simulations. The methodology utilizes a surrogate model constructed by previously selected design points to be used in the optimization. Simulations of the design points are required to be done with high fidelity CFD and EM prediction tools. The methodology behind the parameterization of the proposed intake, SBAO methodology and CFD and RCS analysis approach are explained in the second part of study.

As the mentioned CFD and RCS analyses are required to offer high accuracy solutions, validation studies for both processes are carried out in the next part of the study. For the CFD processes, two validation studies, an intake and a duct, are carried out with mesh independence and turbulence model selection studies. At the end of the studies, a sizing for intake mesh and  $k-\omega$ -SST turbulence model is selected. For the RCS processes, three validation studies are carried out with a triangular prism, a truncated cone and a simple intake duct. For the benchmark cases and the simple duct geometry, the RCS prediction method is deemed successful at capturing the electromagnetics phenomena and usable.

In the next part of the study, a design problem is constructed with several assumptions and the design studies are carried out. A DSD study is carried out with the parametric intake model to eliminate unnecessary parameters. The DSD study, containing 17 design points, showed that all parameters are effective regarding the performance outputs and no elimination is done. Then the DOE study with 49 design points is conducted. After validating the DSD results using the DOE outputs, a surrogate model is constructed using the obtained data. The surrogate model is used in the optimization study which aims to maximize the aerodynamics and signature performances. 4000 designs are evaluated in the optimization study and the 20 highest performing designs are evaluated. Evaluation revealed that the convergence is ensured and some parameters are limited by the design space. The highest performing design, Design 313 is selected as the validation design and it has a respectable PR value of 0.9376, DC value of 0.3113 and modified RCS value of -10.4906 dBm<sup>2</sup>.

In the last part of the study, the best performing design is validated using the high fidelity prediction tools. Validation results showed that the surrogate model predicted the PR value under 1% difference, DC value under 7% difference and the RCS value under 2% difference from the high fidelity results. The actual differences of performance values are all under the cross-validation residual values, so the proposed method of design is regarded as successful.

Several discussion are made on the validation results including the double curved ducts aerodynamic and signature performance. The results showed that from the aerodynamics aspect, the separation zones on both duct parts may be unavoidable for a design space like at hand, but competitive results can be achieved. From the radar signature aspects, actual results give RCS values between -5 and 32 dBm<sup>2</sup> and more importantly, from the nose-on illumination angle, the RCS value of -18.62 dBm<sup>2</sup> is obtained. Relevant nose-on RCS value (0.014 m<sup>2</sup>) is close to the generalized bird RCS value (0.01 m<sup>2</sup>) and can be reduced up to 0.001 m<sup>2</sup> by adjusting orientation of the airframe with respect to the radar system. It is deduced that even though the

results show competitive outputs, including the lip geometry in the preliminary or post design studies should be beneficial for obtaining better performance outputs.

For future studies, several improvements can be implemented in the design process and evaluations can be done as listed below.

- Intake lip geometry can be implemented into the parametric model and an extended screening study can be carried out to determine the effective lip parameters. Inclusion of lip geometry can be beneficial for better overall intake performance inspite of the increased computational effort.
- Off-design aerodynamic performance evaluation can be implemented into the design process since the thesis is focused on on-design point for performance evaluation. Although it can greatly increase the computational effort, off-design evaluation can be useful at assessing the overall intake system performance.
- Extended studies for advance flow control inside the duct (vortex generators, bleed systems, etc.) can be carried out to improve the aerodynamics performance of the intake system.
- Extended studies on RAM can be done to improve signature performance of the intake system.



## REFERENCES

- [1] P. P. Walsh and P. Fletcher, *Gas Turbine Performance*, Second Edi. Blackwell Publishing Company, 2004.
- [2] H. I. H. Saravanamuttoo, G. F. C. Rogers, H. Cohen, P. V. Straznicky, and A. C. Nix, *Gas Turbine Theory*, 7th editio. Pearson Education Limited, 2017.
- [3] A. Sóbester, “Tradeoffs in Jet Inlet Design: A Historical Perspective,” *Journal of Aircraft*, vol. 44, no. 3. American Institute of Aeronautics and Astronautics Inc., pp. 705–717, 2007, doi: 10.2514/1.26830.
- [4] N. C. Bissinger and T. Breuer, “Basic Principles - Gas Turbine Compatibility - Intake Aerodynamic Aspects,” in *Encyclopedia of Aerospace Engineering*, John Wiley & Sons, Ltd, 2010.
- [5] J. Seddon and E. L. Goldsmith, *Intake aerodynamics*, 2nd editio. Reston, VA: AIAA, 1999.
- [6] Raytheon Missiles & Defense, “Tomahawk Cruise Missile.” [https://www.raytheonmissilesanddefense.com/sites/rtx1/files/2020-01/tomahawk\\_gal\\_img5.jpg](https://www.raytheonmissilesanddefense.com/sites/rtx1/files/2020-01/tomahawk_gal_img5.jpg) (accessed Jul. 31, 2021).
- [7] ROKETSAN Missiles Inc., “ATMACA ANTI-SHIP MISSILE.” <https://www.roketsan.com.tr/wp-content/uploads/2019/06/Atmaca-3.jpg> (accessed Jul. 31, 2021).
- [8] Kongsberg, “Naval Strike Missile.” [https://www.kongsberg.com/globalassets/kda/products/defence-and-security/missile-systems/nsm-naval-strike-missile-nsm/nsm\\_fliht.jpg?w=1601&h=675&mode=max&quality=65&format=jpg](https://www.kongsberg.com/globalassets/kda/products/defence-and-security/missile-systems/nsm-naval-strike-missile-nsm/nsm_fliht.jpg?w=1601&h=675&mode=max&quality=65&format=jpg) (accessed Jul. 31, 2021).
- [9] A. Zdunek and W. Rachowicz, “Efficient Het-Engine Inlet Radar Cross-Section Prediction Using Higher-Order Finite-Element Method and Reduced-Order Modeling,” *Electromagnetics*, vol. 34, no. 3–4, pp. 345–362, 2014, doi: 10.1080/02726343.2014.877777.
- [10] E. F. Knott, “Radar observables,” *NASA STI/Recon Tech. Rep.*, vol. 92, pp. 107–194, 1992.
- [11] P. H. Pathak and R. J. Burkholder, “Modal, Ray, and Beam Techniques for Analyzing the EM Scattering by Open-Ended Waveguide Cavities,” *IEEE Trans. Antennas Propag.*, vol. 37, no. 5, pp. 635–647, 1989, doi: 10.1109/8.24192.

- [12] D. Lynch, *Introduction to RF Stealth*. SciTech Publishing Inc., 2004.
- [13] Lockheed-Martin Corporation, “F-35 Lightning II.” <https://www.lockheedmartin.com/content/dam/lockheed-martin/aero/photo/F-35/f35product/2019launch/f35-global-partnerships-splash.jpg.pc-adaptive.1920.medium.jpg> (accessed Jul. 31, 2021).
- [14] ROKETSAN Missiles Inc., “SOM-J JSF-COMPATIBLE STAND-OFF MISSILE.” <https://www.roketsan.com.tr/wp-content/uploads/2018/06/SOM-j-1-1024x370.jpg> (accessed Jul. 31, 2021).
- [15] J. M. Zhang, C. F. Wang, and K. Y. Lum, “Multidisciplinary Design of S-Shaped Intake,” *Collect. Tech. Pap. - AIAA Appl. Aerodyn. Conf.*, no. August, pp. 1–16, 2008, doi: 10.2514/6.2008-7060.
- [16] N. V. Queipo, R. T. Haftka, W. Shyy, T. Goel, R. Vaidyanathan, and P. Kevin Tucker, “Surrogate-based analysis and optimization,” *Prog. Aerosp. Sci.*, vol. 41, no. 1, pp. 1–28, 2005, doi: 10.1016/j.paerosci.2005.02.001.
- [17] J. P. C. Kleijnen, “Kriging metamodeling in simulation: A review,” *Eur. J. Oper. Res.*, vol. 192, no. 3, pp. 707–716, 2009, doi: 10.1016/j.ejor.2007.10.013.
- [18] S. R. Wellborn, B. A. Reichert, and T. H. Okiishi, “Study of the compressible flow in a diffusing S-duct,” *J. Propuls. Power*, vol. 10, no. 5, pp. 668–675, 1994, doi: 10.2514/3.23778.
- [19] T. M. Berens, A. L. Delot, M. Chevalier, J. Van Muijden, R. A. Waaijer, and P. Tattersall, “Application of CFD to high offset intake diffusers,” 2012.
- [20] S. Aslan, “Experimental and Numerical Investigation of an S-Duct Diffuser That Is Designed for a Micro Turbojet Engine Powered Aircraft,” 2017.
- [21] D. Escot-Bocanegra, D. Poyatos-Martinez, R. Fernández-Recio, A. Jurado-Lucena, and I. Montiel-Sánchez, “New Benchmark Radar Targets for Scattering Analysis and Electromagnetic Software Validation,” *Prog. Electromagn. Res.*, vol. 88, pp. 39–52, 2008, doi: 10.2528/PIER08102201.
- [22] S. K. Wong, E. Riseborough, G. Duff, and K. K. Chan, “Radar cross-section measurements of a full-scale aircraft duct/engine structure,” *IEEE Trans. Antennas Propag.*, vol. 54, no. 8, pp. 2436–2441, Aug. 2006, doi: 10.1109/TAP.2006.879223.
- [23] H. T. Anastassiou, J. L. Volakis, and D. S. Filipovic, “Integral equation modeling of cylindrically periodic scatterers in the interior of a cylindrical waveguide,” *IEEE Trans. Microw. Theory Tech.*, vol. 46, no. 11 PART 1, pp. 1713–1720, 1998, doi: 10.1109/22.734568.
- [24] D. C. Ross, J. L. Volakis, and H. T. Anastassiou, “Efficient computation of radar scattering modulation from jet engines,” *Radio Sci.*, vol. 31, no. 4, pp.

- 991–997, 1996, doi: 10.1029/96RS00780.
- [25] H. Edefur, M. Tormalm, L. Tysell, and M. J. Quas, “Design and integration of a low observable intake for the MULDICON platform,” *2018 Appl. Aerodyn. Conf.*, pp. 1–20, 2018, doi: 10.2514/6.2018-3162.
- [26] L. Shi and R. W. Guo, “Serpentine Inlet Design and Analysis,” 2012, doi: 10.2514/6.2012-839.
- [27] W. V Collie, R. Burgun, S. N. Heinzen, C. E. Hall, and N. Chokani, “ADVANCED PROPULSION SYSTEM DESIGN AND INTEGRATION FOR A TURBOJET POWERED UNMANNED AERIAL VEHICLE,” 2003.
- [28] A. Rigobello, “A Multi-objective shape optimization of an S-Duct intake through NSGA-II genetic algorithm,” *Universita’ Defli Studi Di Padova*, 2016.
- [29] F. Furlan, N. Chiereghin, T. Kipouros, E. Benini, and M. Savill, “Computational design of S-Duct intakes for distributed propulsion,” *Aircr. Eng. Aerosp. Technol.*, vol. 86, no. 6, pp. 473–477, 2014, doi: 10.1108/AEAT-04-2014-0046.
- [30] M. J. Anderson and P. J. Whitcomb, *DOE Simplified*, 2nd editio. New York: Productivity Press, 2017.
- [31] C. Lee and C. Boedicker, “Subsonic Diffuser Design and Performance for Advanced Fighter Aircraft,” Oct. 1985, doi: 10.2514/6.1985-3073.
- [32] O. Akman, “SUBSONIC-TRANSONIC SUBMERGED INTAKE DESIGN FOR A CRUISE MISSILE,” Middle East Technical University, 2014.
- [33] D. C. Montgomery, *Design and Analysis of Experiments*, 8th editio. 2017.
- [34] SAS Institute Inc., *JMP 14 Design of Experiments Guide*. Cary, NC, 2018.
- [35] J. P. C. Kleijnen and W. C. M. Van Beers, “Application-driven sequential designs for simulation experiments: Kriging metamodelling,” *J. Oper. Res. Soc.*, vol. 55, no. 8, pp. 876–883, 2004, doi: 10.1057/palgrave.jors.2601747.
- [36] Red Cedar Technology, “SHERPA, An Efficient and Robust Optimization (Search) Algorithm,” pp. 1–3, 2014.
- [37] Ansys Inc., *ANSYS Fluent Theory Guide*. 2013.
- [38] D. Anderson, J. C. Tannehill, and R. H. Pletcher, *Computational Fluid Mechanics and Heat Transfer*, 3rd editio. CRC Press, 2012.
- [39] G. J. Verhoeven, “The reflection of two fields – Electromagnetic radiation and its role in (aerial) imaging,” *AARGnews*, vol. 55, pp. 13–18, 2017.
- [40] A. A. Noor Hafizah, M. Y. Haziq Hazwan, A. R. Nur Emileen, R. A. Raja

Syamsul Azmir, O. Kama Azura, and S. Asem, "RCS analysis on different targets and bistatic angles using LTE frequency," in *Proceedings International Radar Symposium*, 2015, vol. 2015-August, doi: 10.1109/IRS.2015.7226397.

- [41] C. K. Yuzcelik, "Radar absorbing material design," Naval Postgraduate School, 2003.
- [42] S. W. Lee, "Shooting and Bouncing Rays: Calculating the RCS of an Arbitrarily Shaped Cavity," *IEEE Trans. Antennas Propag.*, vol. 37, no. 2, pp. 194–205, 1989, doi: 10.1109/8.18706.
- [43] S. R. Wellbom, T. H. Okiishi, and B. A. Reichert, "NASA Technical Memorandum 106411 A Study of the Compressible Flow Through a Diffusing S-Duct," no. December, 1993.
- [44] Technical Directions Inc., "TDI-J85." <https://tdi-engines.com/tdi-j85/> (accessed Jul. 31, 2021).
- [45] PBS Aerospace, "Jet Engine PBS TJ150." <https://www.pbs.cz/en/Aerospace/Aircraft-Engines/Jet-Engine-PBS-TJ150> (accessed Jul. 31, 2021).
- [46] TUSAS Engine Industries Inc., "TEI-TJ300." <https://www.tei.com.tr/en/products/tei-tj300-turbojet-engine> (accessed Jul. 31, 2021).
- [47] M. I. Skolnik, "Introduction to Radar Systems," *Sens. Rev.*, vol. 19, no. 2, 1999, doi: 10.1108/sr.1999.08719bae.001.